ULTRA-CLEAN WAFER-LEVEL VACUUM ENCAPSULATED INERTIAL SENSORS USING A COMMERCIAL PROCESS

Adel Merdassi

Department of Electrical and Computer Engineering

McGill University, Montreal, Canada

July, 2016

A thesis submitted to McGill University in partial fulfillment of the

Requirements of the degree of Doctor of Philosophy

ACKNOWLEDGEMENTS

First of all, I would like to express my deepest gratitude to my supervisor, Professor Dr. Vamsy Chodavarapu. Thanks to his confidence, generous effort, patience, and good guidance, I succeeded to complete this thesis. I am very thankful to the ministry of high education of Tunisia that in-part supported my graduate education. Equally, I am thankful to the Natural Sciences and Engineering Research Council (NSERC), which in-part financially supported my research studies. Also, I would like to express my acknowledgment to the Integrated Sensors Systems (ISS) program that supported my Doctoral studies.

I had a great pleasure working at the Sensors Microsystems Laboratory (SML) where I conducted all my research study under good conditions and friendly environment. Special thanks to the favors from McGill Nanotools Microfab staff: Manager Dr. Mathieu Nannimi, Dr. Lino Eugene, Mr. Don Berry, Mr. Seddik Benhammadi and Dr. John Li who supported me during all my research work and to their trainings on the microfabrication tools. Also, special thanks to the Clean room staff at Ecole Polytechnique de Montreal and especially to the manager Dr. Alireza Mesgar and Mr Cristophe Clément for their advice and help.

Special thanks are addressed to Canada Microelectronics Corporation (CMC) that supported in providing MEMS design tools and access to different commercial MEMS fabrication processes.

TABLE OF CONTENTS

LIST OF FIGURES

LIST OF TABLES

PUBLICATIONS

JOURNAL PUBLICATIONS:

[1] A. Merdassi, P. Yang, and V. P. Chodavarapu, "A Wafer Level Vacuum Encapsulated Capacitive Accelerometer Fabricated in an Unmodified Commercial MEMS Process," *Sensors (Basel, Switzerland)*, vol. 15, pp. 7349-7359, 03-25 2015.

[2] A. Merdassi, M. N. Kezzo, G. Xereas, and V. P. Chodavarapu, "Wafer level vacuum encapsulated tri-axial accelerometer with low cross-axis sensitivity in a commercial MEMS Process," *Sensors and Actuators A: Physical*, vol. 236, pp. 25-37, 12/1/ 2015.

[3] A. Merdassi, M. N. Kezzo, and V. P. Chodavarapu, "Wafer-Level Vacuum-Encapsulated Rate Gyroscope with High Quality Factor in a Commercial MEMS Process," *Sensors and Actuators: A Physical*, p. Under Review, 2016.

[4] A. Merdassi, C. Allan, E. J. Harvey, and V. P. Chodavarapu, "Capacitive MEMS absolute pressure sensor using a modified commercial microfabrication process," Accepted for Publication in *Microsystem Technologies*, 2016.

CONFERENCE PROCEEDINGS PUBLICATIONS:

[5] Y. Wang, C. Allen, S. AL-Qahtani, A. Merdassi, V. P. Chodavarapu, E. Harvey, *et al.*, "Towards Wireless Implantable Pressure Sensor to Monitor Compartment Syndrome in Trauma Victims," in *Proceedings of NanoTech Conference*, Washington DC, USA, 2013.

[6] A. Merdassi, Y. Wang, G. Xereas, and V. P. Chodavarapu, "Design and fabrication of three-axis accelerometer sensor microsystem for wide temperature range applications using semi-custom process," in *Proceedings of SPIE MOEMS-MEMS*, San Francisco, 2014, pp. 89730O-89730O-12.

[7] A. Merdassi and V. P. Chodavarapu, "Design of 3-axis capacitive low-gravity MEMS accelerometer with zero cross-axis sensitivity in a commercial process," in *Proceedings of NanoTech Conference*, Washington DC, USA, 2013.

[8] A. Merdassi and V. P. Chodavarapu, "Amorphous Silicon Carbide Based Anemometer for Harsh and Corrosive Air/gas flow Measurements," in *Proceedings of the 16th Canadian Semiconductor Science and Technology Conference*, Thunder Bay, Canada, 2013.

[9] B. Jlassi, V. Nerguizian, and A. Merdassi, "Design methodology of a high power RF MEMS switch for wireless applications," in *Fly by Wireless Workshop (FBW), 2011 4th Annual Caneus*, 2011, pp. 1-4.

ABSTRACT

Inertial sensors, such as accelerometers and gyroscopes, have become ubiquitous in our daily lives and are found in a variety of devices and applications that require measurement of motion, direction, vibration and orientation. These integrated sensors benefiting from the tremendous advancements in microfabrication technology continue to grow rapidly providing efficient control and continuous monitoring in a variety of applications including smartdevices, automotive, aerospace, and industrial robotics. Here, both the choice of the fabrication technology and the design of the sensor devices play an important role to develop high performance MicroElectroMechanical Systems (MEMS) inertial sensors to insure stability, repeatability and accuracy of the measurements during operation.

Literature review of MEMS inertial sensors reveals that many of these sensors are developed using full custom or proprietary micromachining processes. Till recently, standard pure-play MEMS processes had several limitations including choice of materials and lack of wafer-level vacuum packaging that made them incapable to support development of integrated inertial sensors with high performance specifications. Recently, the availability of standard pure-play MEMS processes that offer excellent advantages in high quality materials and advanced packaging could lead to development of new inertial sensors that can be readily mass-produced. These devices could help towards lowering the cost of devices with increased competition to existing players in the market and pursuing niche application areas that cannot be satisfied by available devices in the market. The present research aims to design, fabricate and characterize high performance novel integrated capacitive inertial sensors including both single axial and multi-axis accelerometer and a multi-axis gyroscope for angular rate measurement.

The developed devices are based on two standard pure-play processes offered by Teledyne DALSA Semiconductor Inc. (TDSI). In 2013, TDSI introduced MEMS Integrated Design for Inertial Sensors (MIDIS) process, which is currently the only commercial MEMS process that includes ultra-clean wafer-level vacuum encapsulation of the MEMS devices at 10 mTorr. MIDIS process helps towards achieving a high Quality factor and reducing noise interference on the MEMS sensor devices. The developed inertial sensors in MIDIS process include a uniaxial accelerometer with ultra-low noise performance enabling resolution of 33mg over a high-g range of ±100g, tri-axial accelerometer with very low cross-axis sensitivity of 0.8%, and rate grade gyroscope with high Quality factor (> 50,000). This research is the first demonstration of wafer-level vacuum packaging of MEMS inertial sensors in a high volume pure-play MEMS process.

RÉSUMÉ

Les capteurs inertiels, tels que les accéléromètres et les capteurs gyroscopiques, sont devenus omniprésents dans notre vie quotidienne et par conséquent ils sont employés dans divers dispositifs et applications nécessitant la mesure du mouvement, la direction, les vibrations et l'orientation. Ces capteurs intégrés ont bénéficié de l'énorme progrès perçu dans la technologie de micro-fabrication qui est en train de croître rapidement, fournissant ainsi un contrôle efficace et une surveillance continue dans les applications concernées tel que les composants intelligents (SmartDevices), l'automobile, l'aérospatiale et la robotique industrielle. Dans ce propos, le choix de la technologie de fabrication et de la conception des dispositifs de détection jouent un rôle très important pour le développement d'un tel capteur inertiel de type systèmes micro-électromécaniques (MEMS) ayant les performances désirées ce qui permet d'assurer la stabilité, la répétabilité et la précision dans les mesures durant le fonctionnement.

Dans ce contexte, la revue de littérature sur les capteurs inertiels nous révèle que plusieurs types de ces capteurs MEMS ont été fabriqués en utilisant des procédés standards de micro fabrication ou bien à l'aide d'un micro-usinage spécifique propre au développeur lui-même. Durant les dernières années, les procédés de micro fabrication standard pour les composants MEMS ont montré plusieurs limitations remarquables pour fabriquer les capteurs inertiels. Ces limitations comprennent principalement le choix du type des matériaux et l'indisponibilité accrue de l'emballage sous vide au niveau du gaufre ce qui rend les performances des capteurs inertiels médiocres. Cependant, la disponibilité récente d'un procédé de fabrication standard pour MEMS (Pure-Play) offrant des avantages efficaces en termes de matériaux de haute qualité ainsi qu'en termes d'encapsulation performante a conduit au développement des capteurs inertiels de nouvelle génération susceptibles d'être facilement produits en masse. Ces

équipements permettent d'abaisser énormément le coût global des dispositifs tout en ayant un avantage concurrentiel par rapport aux autres compétiteurs existants sur le marché. De plus, ces dispositifs permettent de répondre à plusieurs problèmes qui ne peuvent pas être résolus par les procédés de fabrication actuels. Les activités de recherche actuelles visent à concevoir, fabriquer et caractériser les nouveaux capteurs inertiels intégrés de haute performance. Ces capteurs comprennent principalement des accéléromètres uni axial ainsi que multiaxial et un capteur gyroscopique pour la mesure de la vitesse angulaire.

Ainsi, les dispositifs développés ont été fabriqués en se basant sur le procédé standard MIDIS (Pure-Play) offert par Teledyne DALSA Semiconductor Inc. (TDSI). Effectivement, en 2013, TDSI introduit un nouveau procédé de fabrication (MIDIS) conçu spécifiquement pour le développement des capteurs inertiels intégrés. MIDIS est actuellement le seul procédé commercial de fabrication MEMS qui se distingue par une encapsulation à ultra faible pression au niveau du gaufre atteignant typiquement une valeur de pression de 10 mTorr. Également, le procédé de fabrication MIDIS permet d'atteindre un grand facteur de qualité et de réduire les interférences de bruit influençant le fonctionnement nominal des capteurs inertiels. Les capteurs inertiels actuels développés par le procédé MIDIS comprennent respectivement, un accéléromètre uni-axial montrant des performances d'ultra-faible bruit ce qui permet d'atteindre une résolution de 33 mg sur une large plage de mesure de ± 100g, un accéléromètre triaxial avec une très faible sensibilité transversale de 0,8%, et un capteur gyroscopique uni-axial avec un facteur de qualité très élevé (>50000). Cette recherche est la première démonstration d'une encapsulation au niveau gaufre sous vide des capteurs inertiels de type MEMS dans un procédé Pure-Play MEMS à volume très élevé.

CONTRIBUTIONS OF AUTHORS

This dissertation is based on three published and under review manuscripts. The candidate, Adel Merdassi, is presented as the primary author in all these manuscripts. The candidate played a major role in the idea conception and device design. The co-authors assisted in the post-fabrication processing of the devices and testing of the devices.

Chapter 3 is based on published paper entitled:

- A. Merdassi, P. Yang, and V. P. Chodavarapu, "A Wafer Level Vacuum Encapsulated Capacitive Accelerometer Fabricated in an Unmodified Commercial MEMS Process," MDPI *Sensors (Basel, Switzerland)*, vol. 15, pp. 7349-7359, 03-25 2015.

Chapter 4 is based on published paper entitled:

- A. Merdassi, M. N. Kezzo, G. Xereas, and V. P. Chodavarapu, "Wafer level vacuum encapsulated tri-axial accelerometer with low cross-axis sensitivity in a commercial MEMS Process," Elsevier *Sensors and Actuators A: Physical*, vol. 236, pp. 25-37, 12/1/ 2015.

Chapter 5 is based on the paper submitted to Sensors and Actuators Journal and entitled:

- A. Merdassi, M. N. Kezzo, and V. P. Chodavarapu, "Wafer-Level Vacuum-Encapsulated Rate Gyroscope with High Quality Factor in a Commercial MEMS Process," Elsevier *Sensors and Actuators: A Physical*, Under Review, 2016.

CHAPTER -1

1. Introduction

1.1. Brief History

MEMS is the acronym for **M**icro-**E**lectro-**M**echanical **S**ystems that refers to miniature devices characterized by small sizes ranging from few hundred nanometers to several millimeters in length and have the ability to move in 3-dimensions. These devices combine both electrical and mechanical components that allow the actuation and the sensing mechanisms, and can be integrated with microelectronic interface circuits forming, compact integrated microsystems.

Historically, MEMS devices have originated from the idea of creating miniaturized devices that can accomplish multiple functions with significant performance improvement over macroscale systems owing to smaller size, lower power consumption, lower cost, and improved reliability. One of the first introduction of MEMS technology was with the development of piezo-resistive silicon strain gauges in the late of 1950s by Kulite Semiconductor (Bell Lab's first licensee of patents on semiconductor piezo-resistance) in 1954. Another demonstration of MEMS devices was reported in 1967 with the fabrication of the cantilever-based resonant gate transistor using anisotropic etching process of silicon material [1]. This initial work was followed the ground-breaking research article by Dr. Petersen with the title, - "Silicon as mechanical material" [2] which opened the doors for the widespread acknowledgement and potential of MEMS technologies. During 1980s had witnessed remarkable advancements in the fabrication of MEMS actuators with tremendous progress in the microfabrication processes. By

the early 1990s, the MEMS technology became more mature and several MEMS sensors such as pressure sensors, accelerometers, and gyroscopes have entered commercial market. In parallel, MEMS development was diversified with the development of microfluidic systems for chemical sensing and lab-on-chip systems for biological and chemical monitoring.

In 1993, saw the development of the first commercial Multiuser MEMS Process based on surface micromachining, called PolyMUMPS, which is a three-layer polycrystalline silicon (poly-silicon) process that allowed cost effective solution to fabricate a variety of MEMS devices [3]. Alongside, Sandia National Laboratories introduced another surface micro-machining process in 1996, termed SUMMiT V, with five layers of poly-silicon layers [4]. The fabrication of MEMS technology had evolved rapidly with the advent of Bosch process in 1994 that allowed the creation of deep features using anisotropic etching process called **D**eep **R**eactive **E**tching (DRIE) process [5]. From 1990 to present, MEMS technology had emphasized the development of new alternatives of fabrication processes specifically devoted to physical sensors and actuators (e.g., inertial sensors, pressure sensors, RF switches, and optical micro mirrors) [6-10]. In particular, over the last two decades, MEMS technology has continued to evolve in many fields, including biomedical applications through the development of microprobes, neural stimulators, and lab-on-chip systems. Today, MEMS devices have become essential components in all life sciences and technology applications covering telecommunications, biomedical, automotive, aerospace, and industrial and home automation sectors.

1.2. MEMS Market

MEMS devices are increasingly employed in a variety of applications due to their cost-effectiveness, multi-function integration and improved performance. According to Yole Development reports [11, 12], the market of MEMS technology will grow from $22 billion in 2015 to $90 billion by 2020, which represents a combined annual growth rate (CAGR) of 12.3 percent for the period 2014-2019. Likewise, the packaging technology is added as a key component for MEMS products due to its cost that ranges between 60 to 80% from the overall MEMS product cost. STMicroelectronics, Bosch, Texas Instruments and Hewlett Packard are among the major suppliers for MEMS products. Other prominent vendors include Knowles-Electronics, Canon, Denso Corporation, Panasonic Corporation, Avago Technologies, Freescale Semiconductor, InvenSense, Analog Devices, Sensata Technologies, Qorvo, and Seiko-Epson Corporation.

It should be noted that diverse MEMS devices are behind the rapid growth of MEMS market. Figure 1.1 illustrates several MEMS devices such as inkjet-heads, pressure sensors, microphones, accelerometers, gyroscopes, digital-compass, inertial-combos, micro-bolometers, thermopiles, micro-displays, projection micro-systems, optical MEMS, micro-dispensers, RF MEMS, and oscillators among others. These MEMS devices find potential in many applications including automotive, aeronautics, health care, electronic games, telecommunications appliances, defense, energy sector, life-science, industrial applications. The increased demand in automotive segment represents an important key market driver in part with regulations requiring monitoring of tire pressure and largely consumer interest in energy efficient, safe and smart-connected automobiles. The pressure and inertial sensors are the major devices driving MEMS market expansion. MEMS pressure sensor can be used to monitor the air pressure in the engines and in Tire Pressure Monitoring System (TPMS) and to monitor the

transmission system pressure [13]. It can be noticed that the total units of MEMS pressure sensors is expected to reach $2.21billion by 2018 [14].

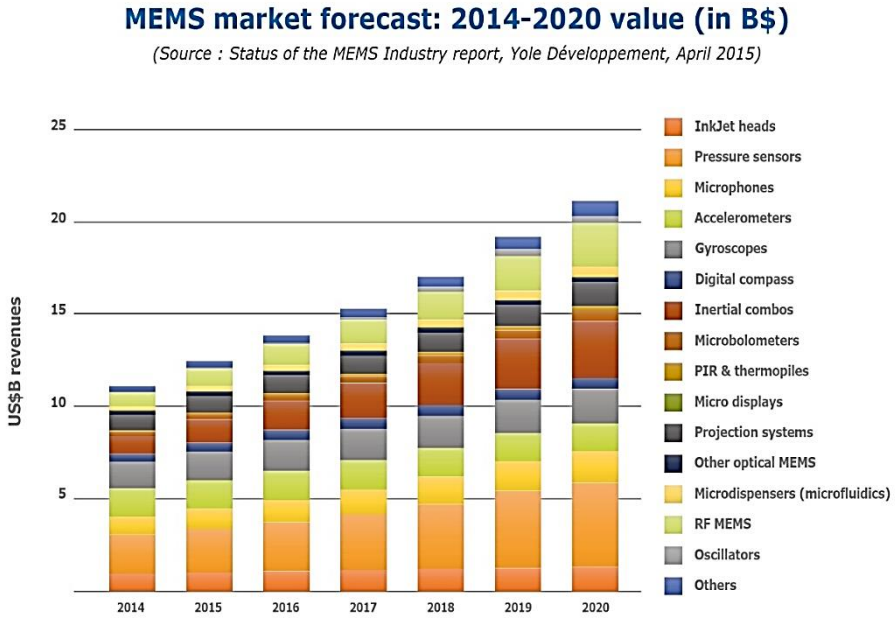

Figure 1.1 MEMS market forecast over the period 2014-2020 [15].

MEMS inertial market has witnessed considerable growth during the last few years that include **I**nertial **M**easurement **U**nits (IMUs) and **I**nertial **N**avigation **S**ystems (INUs) with expected global market growth of 10.5% in 2020. This rapid growth for inertial devices allows the accelerometers and gyroscopes markets to experience continuous increase over the next 5 years. The accelerometers sensors are employed in many automotive applications include safety systems such airbag release systems, **A**nti-lock **Br**aking **S**ystem (ABS), seat belt control, and **E**lectronic **S**ystem **C**ontrol (ESC).

The Global MEMS Gyroscope market is predicted to grow at a CAGR of 9.1 percent over the period 2014-2019 according to TechNavio's analysis [16]. These devices are used to control the dynamic stability of automobiles by detecting the tilting deviation and the yaw rate. Figure

1.2 shows the global inertial sensor market for 2017. As can be seen, the automotive sector controls 34% of the total inertial sensor MEMS market, which represents the largest market share of gyroscopes sensors.

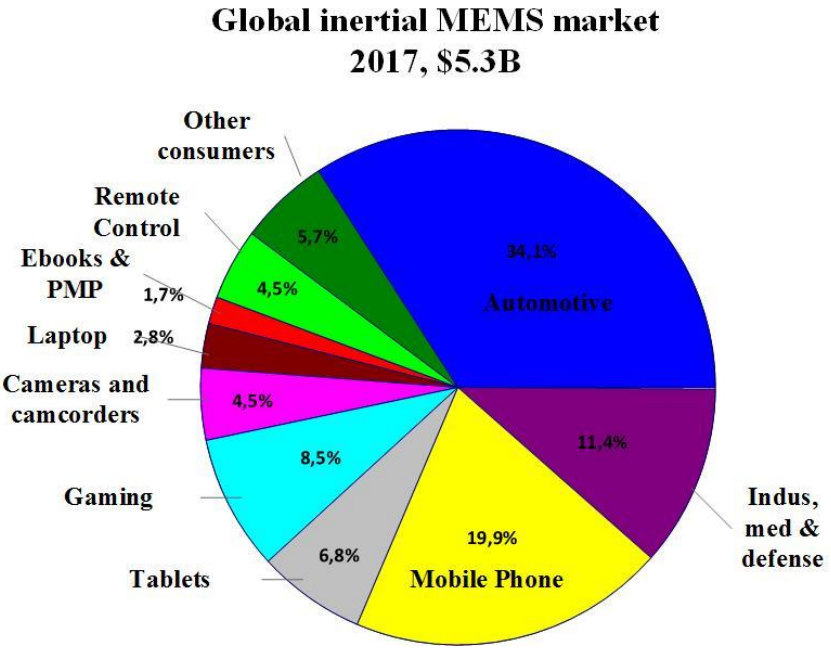

Figure 1.2 Global Inertial Sensors market. Redrawn from Reference [17].

Other major devices found in MEMS market include Digital Mirror Device (DMD) chips that are used in display projectors that contain thousands of MEMS micro-mirrors, MOEMS devices such as optical switches used for data communication, BioMEMS chips employed in health-care monitoring with **L**ab-**O**n-**C**hip (LOC) technology, **M**icro **T**otal **A**nalysis **S**ystem (µTAS), RF MEMS (e.g., shunt capacitive switches and switchable capacitors).

1.3. Design Methodology

The design flow applied for MEMS products is generally constrained by the fabrication processing features. Any change in the process Design Rule Check (DRC) rules impacts the

design characteristics and subsequently the device specifications. Thus, the MEMS structure depends intimately on the materials properties and the capability of each process step that forms the complete fabrication process. Figure 1.3 depicts the design methodology used to fabricate MEMS devices with the involvement of the manufacturing aspects.

The design methodology begins with the input specifications that can help to select the appropriate layout of the designs, and then it continues by using approximate analytical analysis followed by modeling and simulation study for optimization purpose. This is achieved through two modeling levels:

- The FEM method that takes into account the real shape of the structure with the use of Finite Element Method (FEM) solvers including Coventorware, Comsol and Ansys.
- Lumped modeling using macro-models applied on a perfect structures (e.g., beams or plates) with the aid of Architect module available from Coventorware software. The ultimate MEMS model is then implemented with the subsequent electronic circuits and a complete simulation result can be achieved.

Once the layouts are prepared and the design meets the required specifications, a verification step is launched by checking the DRC rules, which in turn validates the fabrication of the masks. If the verification fails then the design will be reviewed again and the process is repeated anew.

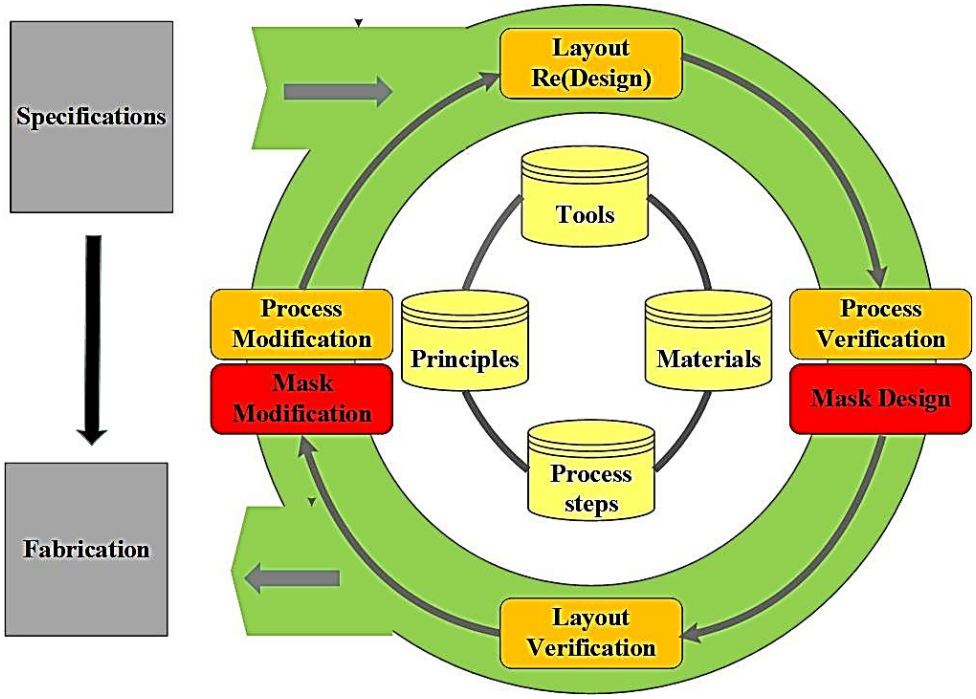

Figure 1.3 MEMS design methodology. Redrawn from Reference [18].

In some cases, the desired structure cannot be achieved with the actual process provided by a MEMS foundry, thus a post-processing step is adopted as another alternative approach to realize the required MEMS structure to meet the desired specifications, which is called a semi-custom fabrication process.

1.4. Sensing Mechanisms in inertial Sensors

Inertial sensors can be classified according to their sensing transduction. The most commonly employed sensing mechanisms include piezo-resistivity, piezoelectricity, capacitive and resonant mechanisms. Typically, these transducers translate motion and orientation into a measurable electrical signal with using appropriate readout electronics. In particular, where the fabrication permits high Quality factor (Q) devices, these sensors can use a complementary resonant element as intermediate transducer to deduce the measurand. In the following Sections,

an overview of the different transduction mechanisms will be presented, explaining the main features and limitations for each sensing mechanism.

1.4.1. Piezo-resistivity

The piezo-resistivity sensing uses strain gauges made from doped semiconductors or metals that undergo a change in their geometrical parameters or their resistivity under the application of mechanical strain or stress [19]. In this case, the resistance variation could be detected by an appropriate readout circuit (e.g., Wheatstone bridge) enabling an electrical output signal variation versus the input strain. The use of such kind of transducers has been widely exploited in many applications that require easier system integration of the transducer with its interface circuitry [20]. Figure 1.4 shows an example of an accelerometer exploiting this transduction technique.

In MEMS technology, doped silicon material is the dominant piezo-resistive element due to its higher Gauge Factor (*GF)* (on order of 100). These elements are formed in bulk silicon substrate or grown from poly-silicon thin-films. One drawback with the silicon piezo-resistivity is related to its strong dependency on temperature, which causes systematic errors in the measurement, and makes it inadequate under harsh environment conditions.

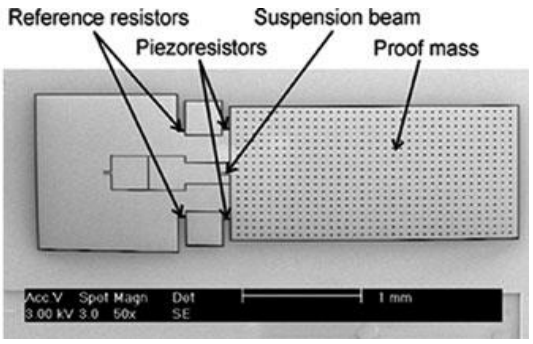

Figure 1.4 MEMS piezo-resistive accelerometer [21]

1.4.2. Piezo-electricity

Some crystal materials like quartz have the ability to generate electric charge when an external mechanical stress or force is applied to it, and inversely, a strain can be generated when applying external voltage. Thus, piezo-electric property is a reversible phenomenon through which both sensing and actuation applications can be implemented. Piezoelectric sensors are considered as active sensors because of their ability to generate electrical energy under application of mechanical force.

In principal, there are three types of piezoelectric materials, namely, crystals (e.g., quartz, lithium niobate, and gallium phosphate), thin-film piezo-electrics (e.g., zinc oxide, aluminum nitride, lead zirconate titanate (PZT)) and polymers (e.g., polyvinylidene fluoride (PVDF)) are widely used in vibratory measurements with using accelerometers and gyroscopes [22, 23]. The crystal substrate is still the dominant material in bulk micromachining. Deposited thin films of ZnT, ZnO PVDF are used in surface micromachining. Recently, *MEMSCAP* foundry has developed PiezoMUMPS standard process that uses 0.5µm of aluminum nitride AlN thin film. An example of PZT thin film is depicted in Figure 1.5.

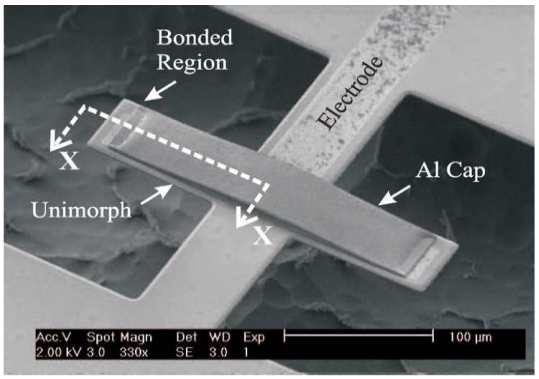

Figure 1.5 Fixed-Fixed beam actuated by PZT thin film from beneath [24]

1.4.3. Capacitive sensing

Capacitive sensing is one of the predominant principles for the development of MEMS sensors as it offers many advantages including low power consumption, long term stability, high sensitivity, high resolution, low temperature dependence (compared to piezo-resistive sensing counterparts), and easy integration with Complementary Metal-Oxide Semiconductor (CMOS) signal processing circuitry [25]. However, capacitive MEMS sensors also have a low immunity against parasitic signals that requires a suitable readout circuit in close proximity to provide shielding against the undesirable noises.

Oftentimes, the mechanical measurand detection of pressure, acceleration, Coriolis force, and shear stress exploits the small displacement of one moving electrode with respect to the anchored part. By acting either on the gap or the overlap length change, one can get a linear relationship between the capacitance variation and the input measurand, which yields an output signal proportional to the desired measurement variable. The typical value for the output of MEMS capacitive sensors ranges between few femtoFarads to several nanoFarads. Currently, there are many commercially available capacitance readout circuits that can detect capacitance changes on the order of sub femtoFarad. Another important advantage of MEMS capacitive sensors is related to their fabrication in several commercial standard processes from pure-play MEMS foundries. Examples of standard processes include SOIMUMPS and PolyMUMPs from MEMSCAP [26-28], ThELMA process from ST-Microelectronics [29], SUMMiT-V from Sandia National Laboratories [30], MIDIS process from TeledyneDalsa, MicraGEM-Si from Micralyne Inc. [31], and many others [9, 10]. Figure 1.6 illustrates an example of capacitive inertial sensor.

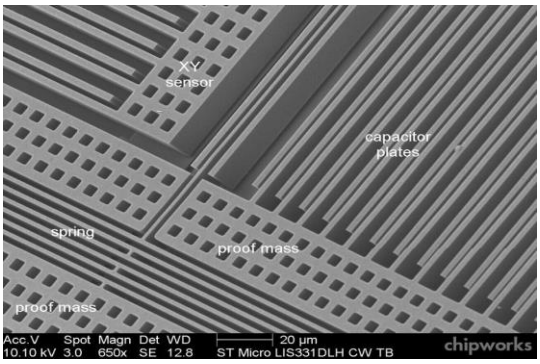

Figure 1.6 SEM Photo of capacitive sensor offered by ST microelectronics [32]

1.4.4. Resonant mode sensing

Resonant sensors use the principle of either frequency/phase or amplitude change [33], such that frequency modulation can be exploited to enhance the sensor immunity against the parasitic signals that can directly affect the measurement. This method leads to a digital modulation or **F**requency **S**hift **K**eying (FSK) that can be transmitted with digital pulses, which, in turn, eliminates the use of analog to digital converter implemented by the readout circuit. Therefore, the resonant sensor microsystem can be interfaced directly to microprocessor for data processing towards a compact sensor system. Figure 1.7 shows an example of two gyroscopes sensors using symmetrical resonator elements.

Many examples of resonant sensors include the fabrication of mechanical resonators, such as resonant beams (e.g., cantilever beam, fixed-fixed beam), **D**ouble **E**nded **T**uning **F**ork (DEFT), and thin clamped plate, among others.

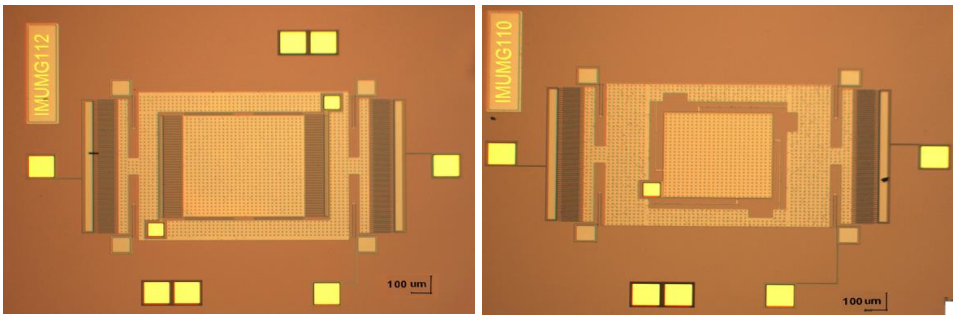

(a) (b)

Figure 1.7 Photomicrograph of PolyMUMPs standard process-based gyroscope using mechanical resonator, (a) In plane measurement and (b) Out of plane measurement

The variation of the resonant frequency can be generated mainly using two parameters, namely, the mass and the spring stiffness. Under an induced mechanical force or stress, the stiffness that is sensitive to the geometrical dimensions is susceptible to a small variation that leads to a linear relationship between the measurement variable and the frequency output. An attractive characteristic of the resonant sensors is related to the higher sensitivity over a wide measurement range, which is desired by many sensors. Further, these devices have long-term stability and offer low power consumption.

The design of the resonant sensor can be carried out through two modes, namely, one port mode that combines simultaneously the excitation and the sensing mechanisms, and two-port mode where the actuation and the sensing are separated. In some cases, the actuation is performed by employing electrostatic excitation through the application of an AC voltage superimposed on a DC voltage. The sensing mechanism can be realized by implementing piezo-resistors or capacitive transducers.

The readout circuits employed in resonant sensors are based, mainly, on oscillators where a resonant element is placed in the feedback loop and acts as a filter that enables Barkhausen condition, or in a **P**hase **L**ocked **L**oop (PLL) demodulator circuit [34]. Additionally, two crucial parameters should be considered in designing resonant sensor, namely, the *Q* and the sensitivity to the temperature gradient that represents the major issue when operating under extreme conditions. Figure 1.8 shows an example of biaxial resonant accelerometer using fixed-guided beam.

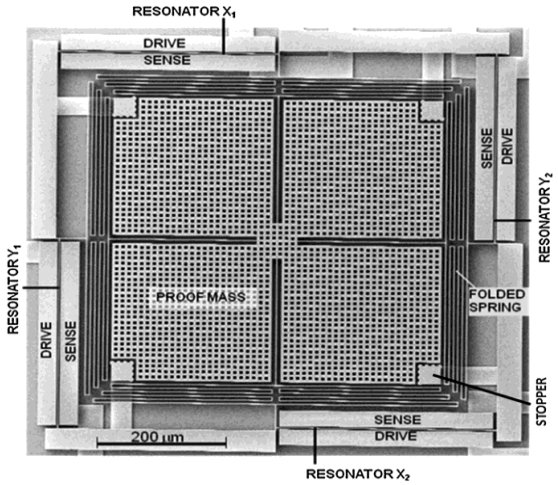

Figure 1.8 MEMS resonant accelerometer [33]

1.5. Inertial Sensors: State of the Art

MEMS inertial sensors such as accelerometers and gyroscopes have become ubiquitous in our daily lives, and are used in a variety of applications including smart devices, automotive, aerospace, and industrial robotics [35-37]. Indeed, inertial sensors are considered valuable elements in many consumer and industrial applications where there is need to monitor motion, direction, vibration, shock and angular velocity. These devices are commercially available with different metrological measurement ranges that meet various application requirements. MEMS inertial sensors are very attractive due to their low cost, low power and high reliability. The present available inertial sensors can be integrated with their readout circuits and other CMOS

signal processing circuits. Automotive sector is a major market area for inertial sensors and many applications in this segment include active stability control, air-bag release systems, and emerging driverless automotive technology [38, 39]. Other applications are related to **S**tructural **H**ealth **M**onitoring (SHM) where motion sensors are specifically implemented in-situ in civil structures such as dams, bridges, buildings [38]. Here, the inertial sensors are employed in vibration analysis such as in rotary machines for predictive maintenance purposes. Further, MEMS inertial sensors can be used in some critical applications with extreme operational conditions such as in down-hole drilling for oil and gas exploration where high vibration environment, high temperature, high pressure and corrosive media may considerably affect sensor performance [40].

1.5.1. Accelerometer Sensors: Applications and Trends

The use of integrated accelerometers has considerably grown in variety of applications that need monitoring and precise control of motion and vibration. The demand for MEMS accelerometers devices is due to the need for low cost, high reliability and improved performance in many applications. In industrial applications, accelerometers are involved in vibrational measurements, active control such as acoustic systems, robotics, machine control, crash detection **E**lectronic **S**tability **C**ontrol (ESC) and safety-critical sensing systems. Emerging applications for accelerometers include wearable devices for human physical activities monitoring and gaming entertainment systems. Figure 1.7 illustrates several accelerometers applications with their classifications according to the sensitivity and cost.

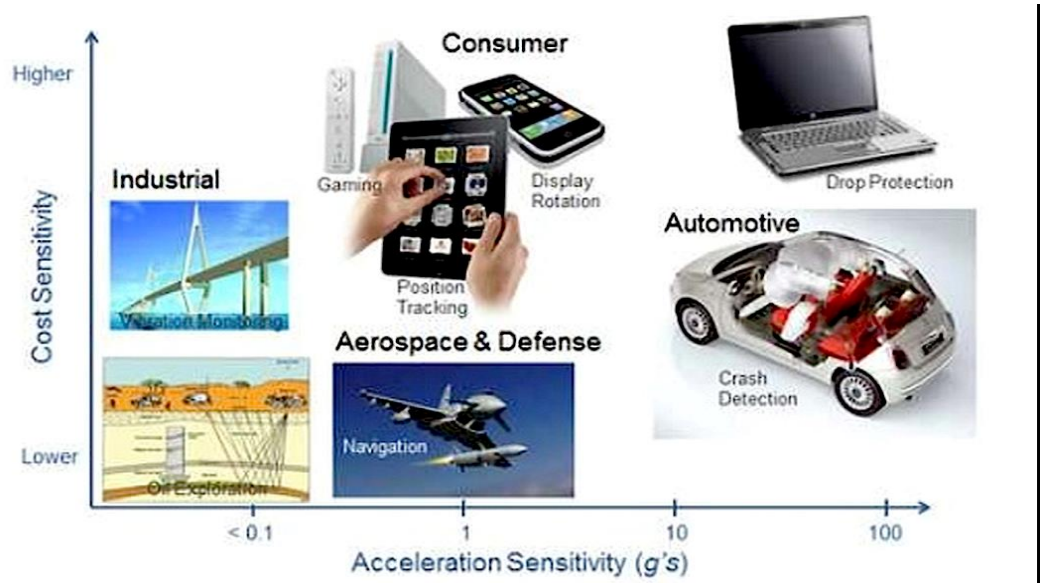

Figure 1.9 Classification of the different applications according to the sensor sensitivity [41]

As explained previously, capacitive accelerometers offer several advantages due to their high sensitivity, low noise, temperature variation cancellation, low fabrication cost, small size, and easy integration with interface circuits and forms the basis of operation for the accelerometers developed in this work. In principle, there are three types of MEMS capacitive accelerometers, namely, thin-film accelerometers based on surface micromachining, bulk-mode accelerometers using bulk micromachining and/or wafer bonding technology and other accelerometers based on high aspect ratio bulk micromachining that can be seen as a combination of surface and bulk micromachining processes.

The first category of surface micro-machined accelerometers is considered as the more prevailing class in the commercial market as exhibited many examples of commercialized MEMS accelerometers sensors offered by Analog Devices, Bosch, Motorola, Freescale, and ST Microelectronics [10, 42-44]. Alternatively, thin films-based accelerometers typically employ aluminum/silicon dioxide as composite material used to fabricate the structural layer. For example, Luo *et al.* [45] and Zhang *et al.*, [46] demonstrated that such composite materials can

be used to fabricate accelerometers for both in-plane and/or out-of-plane detection. The technology of surface micro-machined accelerometers allows noise floors ranging from 0.1 to $1mg/\sqrt{Hz}$ [47, 48]. Likewise, Franke et al. [49] demonstrated capacitive accelerometers using poly-SiGe (poly-silicon germanium) with low temperature deposition process.

The second category concerns the bulk micro machining-based accelerometers that enable the measurement detection in the range of very low-g (± 100mg) or even ultra-low acceleration ($\pm 100\mu g$) as noticed from the research works of Kulah, *et al.* [50] and Chae, *et al.* [51]. A variety of bulk MEMS accelerometers were developed using wet etching processes followed by bonding process for high performance encapsulation [52].

The combination of the above fabrication methods led to the development of new third generation of devices based on high aspect ratio bulk micromachining with using Silicon-on-Insulator (SOI) wafers, which allows the use of a thick single silicon material as structural layer, enabling better repeatability and mechanical performance. This new technology takes advantage from both surface and bulk micromachining and it further allows multi axes detections with a higher resolution performance. Previously, Li. *et al.* [53] demonstrated three-axis capacitive accelerometer using separate chips implemented in one single package.

Over the past several years, many commercial processes are used to fabricate accelerometers MEMS sensors including MUMPS [53, 54], SUMMiT V [30], IMEC's SiGe [55] and ThELMA [56]. The use of commercial processes allows the development highly reliable and reproducible devices with high manufacturing yield and low cost. The packaging of inertial sensors is a vital factor that can directly influence the final characteristics of the product in terms of mechanical

stress, shock transmission, metrology specifications, reliability and the overall product cost. Over the past decades, many packaging techniques were investigated revealing special important characteristics such as hermetic sealing under vacuum or under specific gas inside the package [57, 58]. These technologies include, mainly, ceramic/metal packages and lead-based connections with external interface circuits, which in turn, considerably increases the overall cost, and affects the sensor microsystem efficiency.

The current trend in the packaging approaches is centered on **W**afer **L**evel **P**ackaging (WLP) that allows overall low cost, improved reliability and high yield processes through a single batch process [59-61]. Further, WLP can help to reduce the total system size by integrating different MEMS devices through the stacking of many layers using interconnection vias that provide the necessary interconnects for signal transmission. In this context, the current technology advances reveal the capability to achieve vertical interconnects using Through Silicon Vias (TSVs), which enhances the efficiency, design simplicity, lowers design space, and lowers parasitic capacitance and electrical impedance [62]. The devices developed in the current work are based on MEMS Integrated Design for Inertial Sensors (MIDIS) process developed by Teledyne DALSA Semiconductor Inc. (TDSI) that offers many of the promising features discussed above for the development of inertial sensors including WLP, TSVs, and thick structural layer.

1.5.2. Accelerometer Operation Description

Generally, an accelerometer is based on the concept of a mass-spring system with the application of an external inertial force. The main component in this analysis concerns the inclusion of reference frame, through which the motion equation can be formulated. Figure 1.10 illustrates the overall concept for the design of MEMS accelerometer, including the spring,

which connects the proof mass or seismic mass to the reference frame, the electrical transducer and the signal conditioning electronic circuit. The resultant inertial force generated by the acceleration acts on the proof mass and induces a displacement change that is proportional to the input acceleration over a specified operating frequency range. The spring can be contracted or extended giving indication of the acceleration direction (positive or negative).

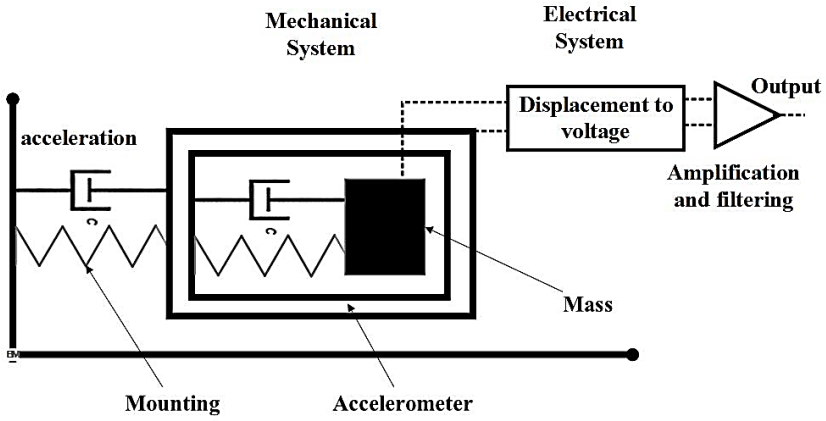

Figure 1.10 Concept of MEMS accelerometer [63]

In most accelerometers, the spring–mass systems is usually under damping mechanism due to the viscosity of fluid medium (air in most cases) so that a drag force is added and is responsible for the dynamic performance. These damping forces can generate nonlinear displacements with frequency dependency. Thus, we give important consideration to the frequency domain as well as time domain analysis. Additionally, a detailed study for the damping mechanisms is necessary in order to evaluate the damping coefficient that, ultimately, determines the *Q* which is an important parameter that dictates high performance in terms of low noise and dynamic measurement. In case of harmonic acceleration, the maximum displacement is reached at resonant frequency. Figure 1.11 shows a simplified model including the reference frame and the mass-spring system.

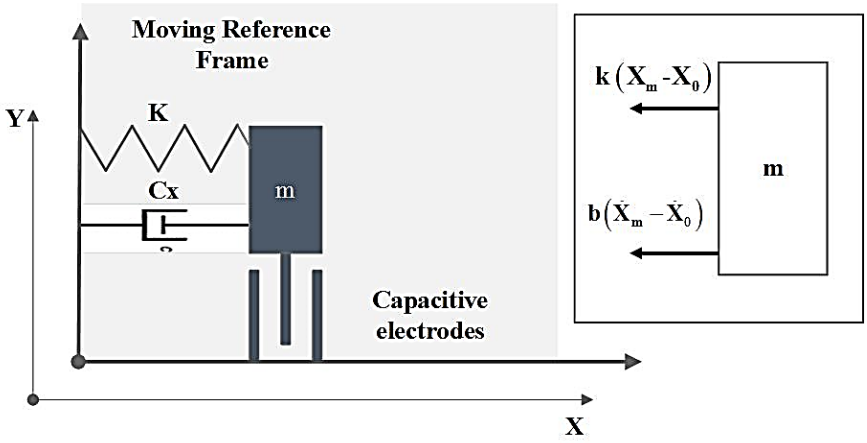

Figure 1.11. Schematic of spring-mass system with capacitive electrodes attached to moving frame. Redrawn from Reference [64]

The governing equation for the spring–mass system is given by Equation (1.1) [65] as,

$$-K\left(X_m - X_0\right) - b\left(\dot{X}_m - \dot{X}_0\right) = m\ddot{X} \tag{1.1}$$

By changing the displacement variable by $x = X_m - X_0$, the motion equation can be simplified by Equation (3.2) as,

$$F_{ext} = ma = m\frac{d^2x}{dt^2} + b\frac{dx}{dt} + kx \tag{1.2}$$

The F_{ext} accounts the inertial force applied to the moving frame, and thus, it is directly proportional to the acceleration measurand. Here, *m* represents the proof mass, *k* is the equivalent spring stiffness and *b* is the damping coefficient.

1.5.2.1. Transmissibility and accelerometer Sensitivity

The sensor sensitivity can be deduced from the product of the electrical sensitivity and the transmissibility (the mechanical sensitivity) and is given by Equation (1.3) as,

$$S_{sensor} = S_{ele}S_{mech} = \left(\frac{\Delta x}{\Delta a}\right)\left(\frac{\Delta C}{\Delta x}\right) \tag{1.3}$$

The transmissibility or mechanical sensitivity represents the transfer function between the displacement and the input acceleration and is defined by Equation (3.4) as,

$$T(\omega) = \frac{X(\omega)}{A(\omega)} = \frac{e^{j\psi}}{\sqrt{\omega_0^2 - \omega^2}} \tag{1.4}$$

where $\psi = -arctg\left(\frac{2\xi\omega_0\omega}{\omega_0^2 - \omega^2}\right)$, ξ is the damping ratio, w_0 is the natural pulsation and is equal to $\sqrt{\frac{k}{m}}$.

A lumped modeling of the overall accelerometer comprising operational amplifier and the mass-spring system with capacitive electromechanical conversion is illustrated by Figure 1.12.

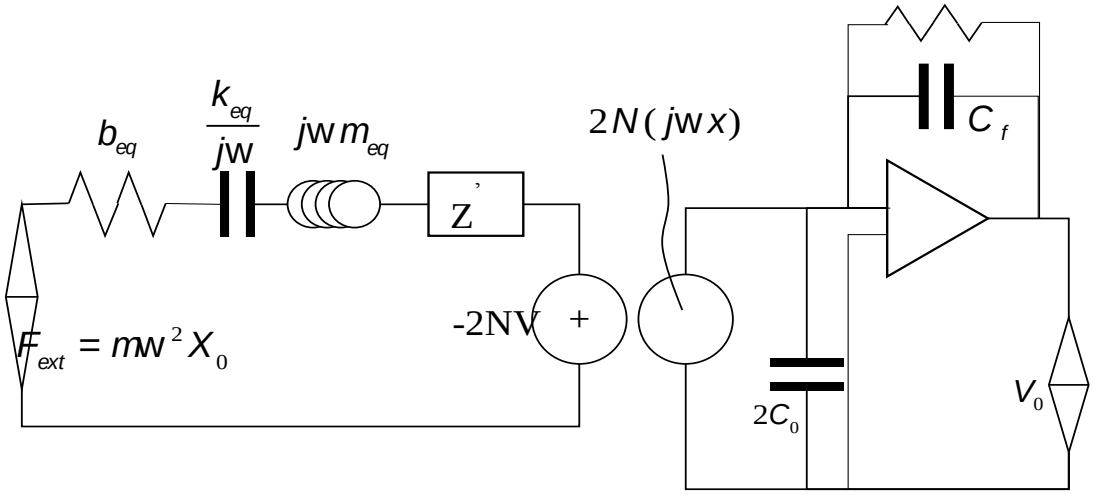

Figure 1.12 Lumped modeling including equivalent mass-spring system, differential capacitive transduction and simple op-amp model. Redrawn from Reference [64].

The overall sensitivity that relates the output voltage with the input acceleration measurand involves the transmissibility *T(ω)* and is deduced by Equation (3.5) [64] as,

$$H(\omega) = T(\omega) \times 2\omega N \times \left(\frac{V}{I}\right) \tag{1.5}$$

where $N = V_B \frac{\partial C}{\partial x}$ is the transducer coupling coefficient and $\frac{V}{I} = \frac{R}{\sqrt{1+\left(\omega R_f C_f\right)^2}}$ is the

electrical impedance with R_f, and C_f the resistance and the capacitance in the sensing element.

The mechanical impedance expression is given by $Z_m^{'} = \frac{\partial f}{\partial \dot{x}} = \frac{1}{j\omega}\frac{\partial^2 W_e^{'}}{\partial x^2} = \frac{1}{2j\omega}\frac{\partial^2 C}{\partial x^2}V^2$ [64].

Likewise, one important parameter that can affect the performance of the accelerometer concerns the frequency bandwidth that is given by Equation (1.6) [38] as,

$$f_B = f_0\sqrt{\sqrt{\left(2\xi^2-1\right)^2+1}-\left(2\xi^2-1\right)} \tag{1.6}$$

The resonance frequency is given by Equation (1.7) as,

$$f_{res} = f_0\sqrt{1-\xi^2} \tag{1.7}$$

where $\xi = \frac{b}{2\sqrt{km}}$.

The sensor sensitivity must be constant over the operating frequency range. At low frequency ($f<<f_{res}$), the mechanical sensitivity can be obtained by setting $\omega = 0$, which yields to Equation (1.8) as,

$$S_{mech} = \frac{1}{\left(2\pi f_0\right)^2} \tag{1.8}$$

Here, one can note a trade-off between the sensitivity and the 3-dB bandwidth. Hence, an optimum value should be established to keep an acceptable performance for the accelerometer. Ultimately, a simple expression for the overall sensitivity can be deduced from Equation (1.9) as,

$$H = 2\frac{1}{(2\pi f_0)^2}\frac{\partial C}{\partial x}\frac{V_0}{C_f} \tag{1.9}$$

1.5.2.2. Damping Performance

One important parameter that directly affects the accelerometer performances concerns the damping mechanism. The viscous damping amount depends on the fluid flow regime around the structure. Thus, many damping mechanisms exist in MEMS sensors such as Couette, Stoke and squeezed film damping mechanisms. The exerted shear stress on a plate moving with velocity u_x inside a fluid is $\tau = -\mu\frac{du_x}{dy}$ where μ (Pa.s) is the dynamic viscosity.

Table 1-1 Damping coefficients according to its damping mechanisms [66-68].

Damping Mechanism	Damping Coefficient
Slide Flow	$\tau_{cb} = \mu\frac{u_0}{h} \Rightarrow F_{cb} = A\mu\frac{u_0}{h}$
Stokes damping	$b_{sb} = \mu\beta A\left(1+\frac{1}{\beta h}\right)$
Squeezed film damping	$b_{sf} = \mu_{eff}\frac{96}{\pi^4}L\left(\frac{w}{h}\right)^3 \approx \mu_{eff}L\left(\frac{w}{h}\right)^3$

Although, we give importance to the gas pressure inside the package that controls the damping, the MEMS design is still an additional critical factor that can adjust the damping coefficient and thus control the dynamic device performance. The encapsulation under low pressure considerably reduces the damping effect. Here, we notice that the over damping mode allows slow sensor response, however, under damped devices are fast but susceptible to overshooting and ringing phenomena under step input excitation.

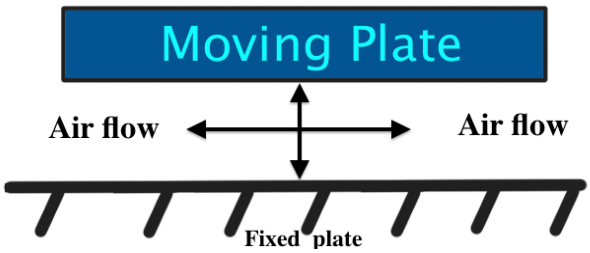

Figure 1.13 Model of simple moving plate in all directions on Airflow.

1.5.2.3. Mechanical Noise

The accelerometer resolution is limited by the noise induced both by the conditioning circuit as well as by the mechanical noise (also called thermal noise or Brownian noise) generated by the air viscosity inside the package. However, the electrical noise is the predominant component that fixes the precision of the sensor. The Brownian noise spectral density, referred to the input acceleration, is given by Equation (1.10) as,

$$\bar{\ddot{x}}_n = \frac{\bar{F}_n}{m} = \frac{\sqrt{4k_B T b}}{m} = \sqrt{\frac{4k_B T \omega_0}{Qm}} \tag{1.10}$$

where T is the temperature, k_B is the Boltzmann constant and Q is the Quality factor and is expressed by $Q = \frac{\sqrt{km}}{b}$. Given the rms vibration amplitude, the input referred rms-acceleration can be deduced through Equation (1.11) as,

$$\ddot{x}_{rms} = \sqrt{\frac{k_B T}{m} \omega_0^2} \tag{1.11}$$

The Figure 1.14 illustrates a simple model for the output signal including the additional mechanical noise component.

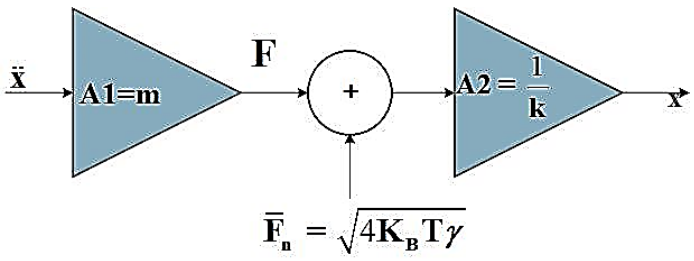

Figure 1.14 Accelerometer Noise model. Redrawn from Reference [69].

1.5.2.4. Other performance indicators

- **Cross Axis Sensitivity**

The cross sensitivity is defined as the ratio of the x-axis deflection caused by an orthogonal acceleration, a_i and the deflection caused by the acceleration applied in the x-axis direction. The relative error can be expressed by Equation (1.12) as,

$$S_x\big|_{a_x=a_j} = \left|\frac{S_{xx_j} - S_x}{S_x}\right| \times 100 \tag{1.12}$$

It should be mentioned that increasing the frequency resonance along the different modes helps to reduce the cross sensitivity effect. Likewise, this has the impact of reducing the parasitic excitation.

- **Temperature Sensitivity**

The temperature sensitivity is an important limiting factor in designing accelerometers especially for harsh environment applications. This issue is mainly due to the mismatch in Coefficient of Thermal Expansion (CTE) of composite materials. Bulk micromachining and high aspect ratio micromachining are highly preferable as single crystal silicon material has excellent thermal characteristics ($2.6\mu m.m^{-1}.K^{-1}$) [70]. Other techniques that can be used consist of employing symmetry structure-based design that enables the cancellation of this perpetual effect.

- **Multi axis measurement**

The fabrication of multi-axis accelerometers is usually based on surface micromachining, which considerably reduces the overall sensitivities regardless of the chosen direction. One option is to embed different structures into one single package with different orientations, which

increases the overall cost compared with monolithic solution. Likewise, using bulk micromachining, the accelerometers are usually sensitive to z-axis, which make it difficult to orient the chip along the other complementary axes and thus make it difficult to obtain highly sensitive accelerometers in all directions. One key to address this issue is to use thick structural layer-based micromachining approach and achieve a trade-off between the sensitivities and the multi-axes sensing.

- **Accelerometer Integration**

The integration of MEMS and readout Integrated Circuit (IC) electronics is a limiting factor in the development of compact MEMS accelerometers. In this case, one possible technique is to address this requirement concerns the monolithic integration, which requires a sophisticated fabrication process. The advances in TSV technology allows the hybrid approach of flip-chip binding of MEMS and Integrated Circuit (IC) components that provides flexibility for mechanical structures with thick structural layer and enables high sensitivity and low noise performance.

1.5.3. Gyroscope Sensors: Applications and Features

Gyroscopes devices are classified as an inertial sensor that allows the measurement of angular velocity as well as the rotation angle. These devices are found in many application areas including automotive sector for **E**lectronic **S**tability **C**ontrol (ESC) and **R**oller-over **S**tability **C**ontrol (RSC) systems [71, 72], aeronautics industry for use in navigation systems [73], and assisted **G**lobal **P**ositioning **S**ystem (GPS) [74, 75]. [76-78]. Gyroscopes are combined with accelerometer devices to form **I**nertial **M**easurement **U**nit (IMU) systems that enable measurement of inertial navigation [77, 79, 80]. In addition, gyroscopes are used in biomedical

applications for monitoring of human body movement and orientation [81] and in medical 3D gesture and motion recognition via Human Machine Interfaces (HMIs) [38, 82]. Additionally, gyroscopes are widely used in many gaming and smart devices [83]. Other applications of gyroscopes include the oil and gas industry to monitor and control the drilling direction in offshore rigs [80, 84]. The global MEMS gyroscope market is expected to reach an estimated growth rate of 9.1 percent over the period 2015-2019 according to the TechNavio's analysts [85].

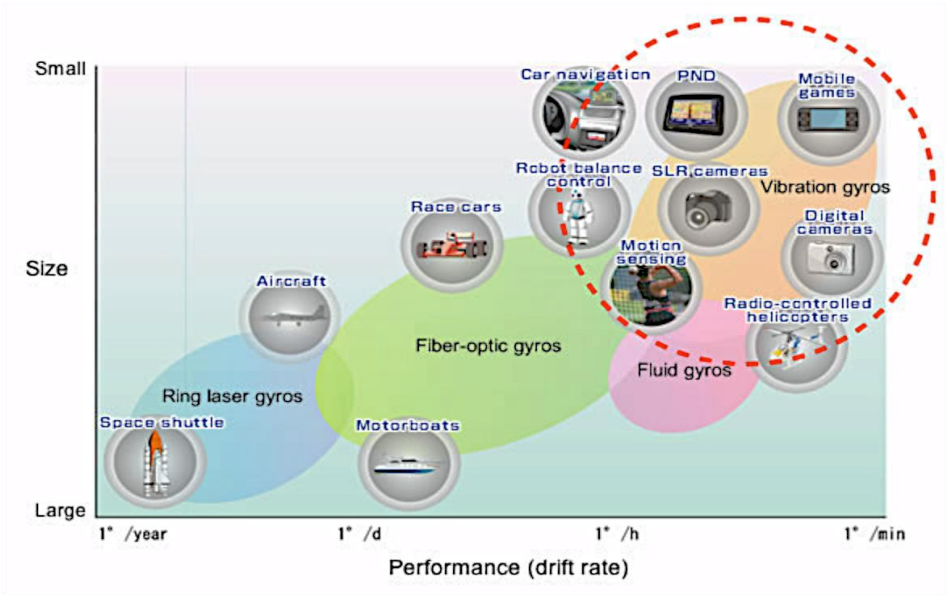

Figure 1.15 Different types of gyroscopes according to their performances and sizes [86]

Traditionally, gyroscopes are designed either based on the angular momentum conservation or using the Sagnac effect experienced by the detection of light beam in a ring interferometer such as in a ring cavity or optical fiber coil. The main gyroscope designs are categorized herein,

- **Momentum Wheel-based Gyroscope:** A gimbal support comprising rotating wheels around different axes insures the stable fixation of the spin axis during the body movement by conserving the angular momentum so that the gimbal angles will enable

angular measurement with respect to the reference frame. The friction issue in this design is reduced through the use of **D**ynamically **T**uned **G**yroscope (DTG) system [87].

- **Ring Laser Gyroscope (RLG):** Two laser beams travel in opposite directions in a closed cavity that is filled with a gas, and meet in return point where an interference phenomenon is produced. Based on the principle of Sagnac interference, the induced displacement between two adjacent fringes is proportional to the rotation rate, hence, the laser beams experience a difference in the travel path once a rotation is produced. Thus, angular velocity measurement can be obtained through the displacement shift measurement between two adjacent fringes or by measuring the phase shift between the two light beams [88].
- **Fiber Optic Gyroscope (FOG):** This method uses the RLG principle by replacing the gas cavity with an optical fiber that can simplify the sensor structure and reduce the gyroscope cost. The optic fiber can be arranged as a coil including many turns. A drawback point found in this method concerns the sensitivity of the fiber to sustain the strain induced by the temperature effect, hence, a reduction in this issue should be addressed when designing the sensor for high performance applications.

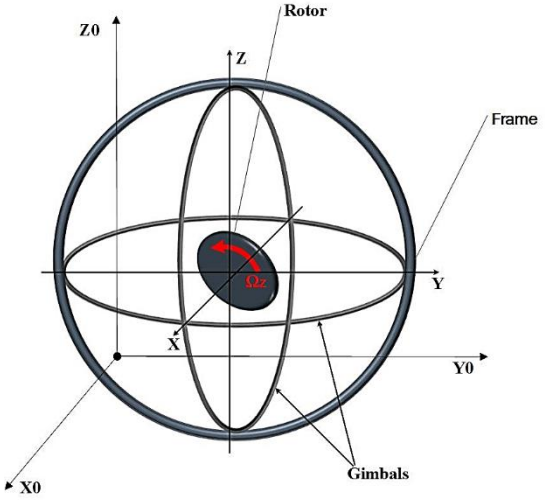

Figure 1.16 Description of the Gimbal system. Redrawn from Reference [64].

In principle, gyroscope sensor can be categorized according to their performance parameters such as consumer grade, rate grade, tactical grade, and inertial navigation grade. In the inertial navigation grade, FOGs and RLGs systems dominate the available devices. However, considerable research in MEMS based devices is being pursued [89, 90]. Many MEMS based devices have been developed and commercially available in the rate and tactical grade [91, 92] category, that have wide range of applications in automotive, industrial and advanced gaming devices. Several high performance gyroscopes with rate and tactical grade performance are available from Systron Donner, Honeywell, Sensonor, Silicon Sensing, and Tronics Microsystems [93-95]. Some devices in these two categories require wide temperature operation range from -55ºC to 125ºC with bandwidth exceeding 70 Hz [39]. Most gyroscopes are characterized by long term bias stability (0.1-10º/h) [96, 97]. The bias stability of the gyroscope measures the drift of the output offset over time. One could use the Root Allan Variance method to quantify the stability in time domain [98].

Many demonstrations of micro-machined gyroscopes began in the early 1990's [99]. In 1993, the silicon-on-glass tuning fork gyroscope [100] was developed by Charles Stark Draper Laboratory that recorded a low noise equivalent rate of 0.1º/s for a given bandwidth of 60 Hz. The implementation of polysilicon-based capacitive gyroscope using surface micro-machining process was introduced in 1996 through the research works of Juneau et.al. [101]. In 1996, Clark et al. [102] from University of California, Berkeley has released a single and dual axis gyroscope devices with the integrated trans-impedance amplifier on a single die using BiMEMS process which enabled a resolution of 1º/s. Other polysilicon-based gyroscopes are commercialized using iMEMS process from Analog Devices (e.g., ADXRS family of gyroscopes [103]) with a sensitivity of 12.5 mVº/s and an estimated bias drift of 50º/h. In 1999, decoupled mode based gyroscope sensor was developed using Deep Reactive Ion etching

(DRIE) process to etch thick single silicon layer enabling a resolution of 0.07º/s over a bandwidth of 10 Hz [104]. In 2002, He et al. [105] from University of Michigan, introduced a high-resolution vibrating ring gyroscope using bulk silicon micromachining. That sensor demonstrated a sensitivity of 130 mV/º/s with estimated noise floor of 10º/h/Hz over low bandwidth of 2 Hz. In 2002, gyroscopes based on the **H**igh aspect-**R**atio combined **P**oly and **S**ingle-crystal **S**ilicon (HRPSS) process was introduced by Ayazi and Najafi who demonstrated a low noise floor of 0.1º/s/$\sqrt{Hz}$ for a given angular velocity range of ±250º/s [106]. In 2007, M^2-TFG-based gyroscope was developed by Sharma et al. [107] that included nulling quadrature and automatic-matching systems using 0.6 µm CMOS process.

It should be noticed that with the evolving advances of the packaging technology and, especially, the advances occurring with TSVs and Wafer Level Packaging (WLP) technologies, capacitive gyroscopes have become attractive alternative to the traditional sensors such as optical and piezoelectric gyroscopes, due to the low noise, low power consumption, low long term drift, excellent stability and high sensitivity. Further, many commercial processes have been developed that are specifically used to fabricate MEMS gyroscopes including MUMPS [108, 109], iMEMS (e.g., ADXRS150, ADXRS300 from Analog Devices Inc.) [110, 111], and ThELMA (e.g., LPR530AL, L3GD20 from STMicroelectronics Inc.) [112].

1.5.4. Gyroscope Operation Description

The gyroscope operating principle is based on the inertial force induced by the vibrating element in rotating reference frame. The resultant force or Coriolis force is fictive and perpendicular to the direction of the produced vibration. The Coriolis force magnitude is

proportional to the angular velocity of the reference frame in which the proof mass is in permanent vibration movement, as given by Equation (1.13) [113],

$$F_c = ma_c = m\left(2\Omega v\right) \tag{1.13}$$

where a_c is the Coriolis acceleration, m the mass of the proof mass, Ω the angular velocity of the reference frame and v the velocity of the vibrating resonator. Figure 1.17 shows the working principle of the gyroscope sensor.

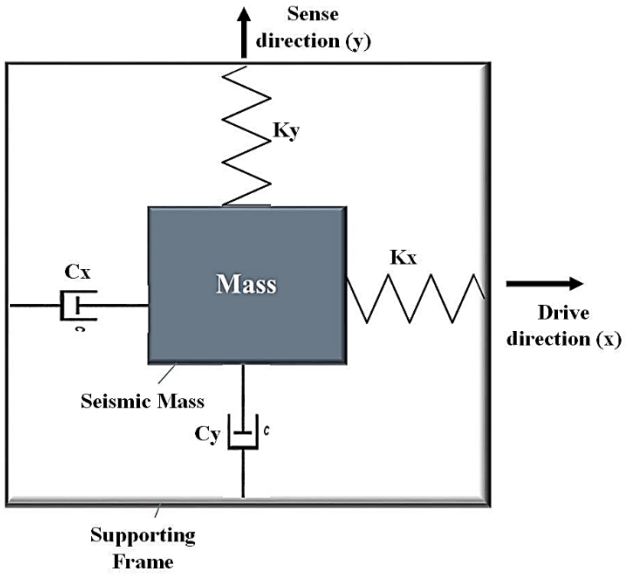

Figure 1.17 Gyroscope operating principle. Redrawn from Reference [114].

Based on the above concept, one can find the dynamic equations that govern the gyroscope motion according to the Equation (1.14) [114] as,

$$\begin{cases} m\ddot{x} + c_x\dot{x} + k_x x = F_x \\ m\ddot{y} + c_y\dot{y} + k_y y = F_y - 2m\Omega_z\dot{x} \end{cases} \tag{1.14}$$

where c is the damping coefficient, k the spring stiffness constant, Ω_z the angular velocity along Z-axis and F is the inertial force.

Typically, the oscillating motion that is fixed at the resonance frequency drives the vibrating element. Thus, the analysis of resonator element proves to be a crucial parameter in the

performance of vibratory gyroscopes. Indeed, under harmonic excitation, the frequency response of the displacement is given by the Equation (1.15) as,

$$x = \frac{\frac{F_{ex}}{k}}{\sqrt{\left(1-\left(\frac{\omega}{\omega_n}\right)^2\right)^2 + \left(2\xi\frac{\omega}{\omega_n}\right)^2}} \tag{1.15}$$

Under ultra-low damping (ξ<<1), the maximum of the oscillation amplitude can be obtained by intervening the *Q* in the displacement expression, as shown by Equation (1.16) as,

$$x_{\max} = \frac{F_{ex}}{k}Q \tag{1.16}$$

Through Equation (1.15), we can deduce the Coriolis force exciting the sense mode by Equation (1.17) as,

$$F_{c\max} = 2m\Omega_z x_{\max}\omega_d = 2m\Omega_z Q\frac{F_{ex}}{k}\omega_d \tag{1.17}$$

and ultimately the static displacement that can be converted into an electrical signal as deduced by Equation (1.18) as,

$$y_{stat} = \frac{F_c}{k_y} = \left(\frac{2mQ\omega_d}{k_x k_y}F_{ex}\right)\Omega_z \tag{1.18}$$

By investigating Equation (1.16), one can improve the sensor sensitivity by increasing the *Q* factor through the decrease of damping mechanisms and the use of thick structural layer for the proof mass that allows the mass, *m*, to increase. Further, one can operate the sense mode at its resonance frequency, which amplifies *Q* times the sensitivity. Hence, the oscillation amplitude can be modulated and then detected by synchronous amplitude demodulator giving an output signal that is linearly proportional to the angular rate velocity. Equation (1.19) gives the expression of the maximum amplitude as,

$$y_{stat} = \frac{F_c}{k_y} = \left(\frac{2mQ_sQ_d\omega_d}{k_xk_y} F_{ex} \right) \Omega_z \tag{1.19}$$

The operation of the gyroscope under the above conditions needs sophisticated electronics to synchronize the two modes (sense and drive) and risks to high error if any frequency mismatch occurs. Thus, operating at resonance frequency with mode match conditions makes the system very sensitive to any variation that causes shift in their dynamic parameters. As can be seen from Equation (1.17), the term $2m\Omega_z\dot{x}$ is induced by the frame rotation and responsible for dynamic coupling between the vibratory axis and the detection axis. Consequently, it could be very useful to decouple both mechanisms (drive and sense) so that we avoid any spurious effect from the vibrating element on the signal to be measured. Therefore, a resonator can be used as the driving element that includes the oscillating proof mass, and another separate mass-spring system acts as a Coriolis force sensor. Furthermore, it is desirable to implement the sensing element inside the drive resonator in order to allow unidirectional and super alignment motion of the oscillation movement along the driving direction, which improves the oscillation stability and avoid any undesirable displacement caused by the Coriolis force.

1.6. Conclusions

The present work in this thesis is focused on developing high performance inertial sensors benefiting from the new advances in WLP technologies. All devices presented in this thesis are based on capacitive transduction. This type of transduction offers significant advantages over the other mechanism counterparts in terms of high reliability, low temperature sensitivity, low drift, low power consumption and low noise.

Our devices are implemented using commercial pure-play MEMS processes where a higher consideration to the fabrication capability which will be useful towards mass-production of inertial sensors. We have adopted the MIDIS process developed by Teledyne DALSA Semiconductor Inc. (TDSI) that offers ultra-high vacuum encapsulation at wafer level with TSV technology that enables a high integration performance for MEMS-IC microsystem. The designs, development and experimentation results of our novel accelerometers and gyroscope will be introduced in the next chapters.

The organization of the thesis is as follows. Chapter 2 is dealing with the specifications, advantages and limitations of MIDIS process in comparison with other foundry alternative process. Equally, the TSV technology and the impact of high vacuum packaging on the performance of the inertial sensors will be discussed.

Chapter 3 describes the uniaxial accelerometer showing the direct advantages of the commercial process on the low noise performance. Design, simulation and experimental results are provided to study the feasibility of high performance inertial sensor under MIDIS platform.

Chapter 4 introduces a novel design of 3-axis accelerometer with 0% cross axis sensitivity that enables simultaneous detection of the acceleration measurement with high accuracy along the three principle directions.

Chapter 5 describes a vibratory gyroscope with high Q factor benefiting from the high vacuum encapsulation to allow high resolution, higher precision and good repeatability in the angular velocity measurement.

The articles described in Chapters 3, 4, and 5 are peer-reviewed journal publications in which I was listed as the first Author and contributed to majority of the research work. Finally, conclusion and summary of the main research activities are presented describing the research perspectives and potential future research activity.

References

[1] N. Harvey, W. E. Newell, R. A. Wickstrom, and J. R. Davis, "The resonant gate transistor," *IEEE Trans. Electron Devices,* pp. 117–133, 1967.

[2] K. E. Petersen, "Silicon as a mechanical material," *Proc. IEEE,* vol. 70, pp. 420-457, 1982.

[3] K. W. Markus, D. A. Koester, A. Cowen, R. Mahadevan, V. R. Dhuler, D. Roberson, *et al.*, "MEMS Infrastructure: The Multi-User MEMS Processes (MUMPs)," in *SPIE 2639, Micromachining and Microfabrication Process Technology*, 1995, p. 10.

[4] J. J. Sniegowski and E. J. Garcia, "Surface micromachined gear trains driven by an on-chip electrostatic microengine," *IEEE Electron Device Letter,* vol. 17, pp. 366–8, 1996.

[5] J. K. Bhardwaj and H. Ashraf, "Advanced silicon etching using high-density plasmas," 1995, pp. 224-233.

[6] G. A. MacDonald, "Proceedings of the 5th International Conference on Solid-State Sensors and Actuators and Eurosensors III A review of low cost accelerometers for vehicle dynamics," *Sensors and Actuators A: Physical,* vol. 21, pp. 303-307, 1990/02/01 1990.

[7] M. Esashi, Y. Matsumoto, and S. Shoji, "Proceedings of the 5th International Conference on Solid-State Sensors and Actuators and Eurosensors III Absolute pressure sensors by air-tight electrical feedthrough structure," *Sensors and Actuators A: Physical,* vol. 23, pp. 1048-1052, 1990/04/01 1990.

[8] J. Jahns and S. J. Walker, "Two-dimensional array of diffractive microlenses fabricated by thin film deposition," *Applied Optics,* vol. 29, pp. 931-936, 1990/03/01 1990.

[9] M. Tang, A. Agarwal, P. Win, Q. X. Zhang, J. Li, and A. Q. Liu, "A New Lateral RF Switch Using SOI-Deep-Etching Fabrication Process," *International Journal of Computational Engineering Science,* vol. 04, pp. 369-372, 2003.

[10] J. Söderkvist, "Proceedings of the 5th International Conference on Solid-State Sensors and Actuators and Eurosensors III Design of a solid-state gyroscopic sensor made of quartz," *Sensors and Actuators A: Physical,* vol. 21, pp. 293-296, 1990/02/01 1990.

[11] Solid-State-Technology. *Three markets will drive the wearable industry*. Available: http://electroiq.com/blog/2015/08/three-markets-will-drive-the-wearable-industry/

[12] Research&Markets. *Global MEMS Market 2015-2019*. Available: http://www.researchandmarkets.com/reports/2252914/global_mems_market_20152019

[13] M. B. Nagaraju, A. R. Lingley, S. Sridharan, J. R. Gu, R. Ruby, B. P. Otis, *et al.*, "A 0.8mm(3) +/- 0.68psi Single-Chip Wireless Pressure Sensor for TPMS Applications," *2015 Ieee International Solid-State Circuits Conference Digest of Technical Papers (Isscc)*, vol. 58, pp. 480-U681, 2015.

[14] P. Newswire. *North America Pressure Sensors Market 2015-2020*. Available: http://www.prnewswire.com/news-releases/united-states-pressure-sensors-market-report-2015---growth-trends-and-forecasts-to-2020-for-the-187-billion-industry-300099066.html

[15] SolidState-Technology. *Growing in maturity, the MEMS industry is getting its second wind*. Available: http://electroiq.com/blog/2015/05/growing-in-maturity-the-mems-industry-is-getting-its-second-wind/

[16] Global-Information. *Global MEMS Gyroscope Market 2014-2019*. Available: https://www.giiresearch.com/report/infi237265-global-mems-gyroscope-market-2011-2015.html

[17] D. Z. Xia, C. Yu, and L. Kong, "The Development of Micromachined Gyroscope Structure and Circuitry Technology," *Sensors*, vol. 14, pp. 1394-1473, Jan 2014.

[18] D. Ortloff, T. Schmidt, K. Hahn, T. Bieniek, G. Janczyk, and R. Brück, *MEMS Product Engineering*: Springs, 2014.

[19] C. S. Smith, "Piezoresistance effect in germanium and silicon," *Phys. Rev*, vol. 94, pp. 42-49, 1954.

[20] S. Stassi, V. Cauda, G. Canavese, and C. Pirri, "Flexible Tactile Sensing Based on Piezoresistive Composites: A Review," *Sensors*, vol. 14, p. 5296, 2014.

[21] T. K. Bhattacharyya and A. L. Roy, "MEMS piezoresistive accelerometers," in *Micro and Smart Devices and Systems*, ed: Springer, 2014, pp. 19-34.

[22] R. Voss, K. Bauer, W. Ficker, T. Gleissner, W. Kupke, M. Rose, *et al.*, "Silicon angular rate sensor for automotive applications with piezoelectric drive and piezoresistive read-out," in *Solid State Sensors and Actuators, 1997. TRANSDUCERS '97 Chicago., 1997 International Conference on*, 1997, pp. 879-882 vol.2.

[23] D. L. DeVoe and A. P. Pisano, "Surface micromachined piezoelectric accelerometers (PiXLs)," *Journal of Microelectromechanical Systems*, vol. 10, pp. 180-186, 2001.

[24] H. K. R. Kommepalli, H. G. Yu, C. L. Muhlstein, and e. al, "Design, fabrication and performance of a piezoelectric uniflex microactuator," *Journal of Microelectromechanical Systems*, vol. 18, pp. 616-625, 2009.

[25] M. Narducci, L. Yu-Chia, W. Fang, and J. Tsai, "CMOS MEMS capacitive absolute pressure sensor," *Journal of Micromechanics and Microengineering*, vol. 23, May 2013.

[26] M. Shuja Khan, S. A. Bazaz, and M. Abid, "Comparative Study on System Model and Finite Element Analysis of a Monolithic 3DOF MEMS Capacitive Accelerometer," p. 528, 2009.

[27] R. A. Dias, L. Mol, R. F. Wolffenbuttel, E. Cretu, and L. A. Rocha, "Design of a Time-Based Micro-g Accelerometer," vol. 11, p. 1683, 2011.

[28] A. Alfaifi, F. Nabki, and M. N. El-Gamal, "A dual-axis bulk micromachined accelerometer with low cross-sensitivity," p. 736, 2012.

[29] A. Briffa, E. Gatt, J. Micallef, I. Grech, O. Casha, and J. M. Darmanin, "Area minimization of a three-axis separate mass capacitive accelerometer using the ThELMA process," p. 2099, 2013.

[30] F. Serrano-Vazquez, A. Herrera-May, and M. Bandala-Sanchez, "Design and modeling of a single-mass biaxial capacitive accelerometer based on the SUMMiT V process," *Microsystem Technologies-Micro-and Nanosystems-Information Storage and Processing Systems*, vol. 19, pp. 1997-2009, Dec 2013.

[31] H. K. Chu, J. K. Mills, and W. L. Cleghorn, "Design of a high sensitivity capacitive force sensor," p. 33, 2007.

[32] S. J. Dixon-Warren. (2010). *Motion Sensing In The Iphone 4: Mems Accelerometer*. Available: http://www.memsjournal.com/2010/12/motion-sensing-in-the-iphone-4-mems-accelerometer.html

[33] A. Caspani, C. Comi, A. Corigliano, G. Langfelder, and A. Tocchio, "Compact biaxial micromachined resonant accelerometer," *J. Micromech. Microeng*, vol. 23, p. 10, September 2013.

[34] G. C. Wei and M. S. C. Lu, "A CMOS MEMS capacitive resonant sensor array utilizing a PLL-based oscillator loop," in *2013 Transducers & Eurosensors XXVII: The 17th International Conference on Solid-State Sensors, Actuators and Microsystems (TRANSDUCERS & EUROSENSORS XXVII)*, 2013, pp. 82-85.

[35] M. Perlmutter and L. Robin, "High-performance, low cost inertial MEMS: A market in motion!," in *Position Location and Navigation Symposium (PLANS), 2012 IEEE/ION*, 2012, pp. 225-229.

[36] A. M. Madni, "Keynote speech:Smart configurable wireless sensors and actuators for industrial monitoring and control," in *Sensors, 2009 IEEE*, 2009, pp. 1658-1659.

[37] I. Popova, A. Lestev, A. Semenov, V. Ivanov, O. Rakityanski, and V. Burtsev, "Micromechanical gyros & accelerometers for digital navigation & control systems," *IEEE Aerospace and Electronic Systems Magazine*, vol. 24, pp. 33-39, 2009.

[38] V. Kempe, *Inertial MEMS Principles and Practice*. New York: Cambridge University Press 2011.

[39] M. Kraft and N. M. White, *MEMS for automotive and aerospace applications*. USA, Philadelphia: Woodhead Publishing Limited, 2013.

[40] W. Muthu and A. Robert, *Silicon Carbide Microsystems for Harsh Environments* vol. 22: Springer Science+Business Media, 2011.

[41] P. Singh. (2014). *Mems accelerometer designing and fabrication*. Available: http://www.slideshare.net/prashantsingh94651/mems-accelerometer-designing-and-fabrication

[42] ST-Microelectronics. *Accelerometers*. Available: http://www.st.com/web/en/catalog/sense_power/FM89/SC444?icmp=sc444_pron_accelerometers_aug2013&sc=accelerometers-nb-aug13

[43] Freescale-Semiconductor. *Low g Accelerometers*. Available: http://www.freescale.com/webapp/sps/site/overview.jsp?code=ACCLOWG

[44] BOSCH-Sensortec. *Acceleration sensors*. Available: https://www.bosch-sensortec.com/en/homepage/products_3/3_axis_sensors/3-axissensors

[45] H. Luo, G. K. Fedder, and L. R. Carley, "A 1 mG lateral CMOS- MEMS accelerometer," in *Proc. 13th IEEE Int. Conf. Micro Electro Mechanical Systems (MEMS 2000)*, Japan, 2000.

[46] Z. Gang, X. Huikai, L. E. d. Rosset, and G. K. Fedder, "A lateral capacitive CMOS accelerometer with structural curl compensation," in *Micro Electro Mechanical Systems, 1999. MEMS '99. Twelfth IEEE International Conference on*, 1999, pp. 606-611.

[47] H. Luo, G. K. Fedder, and L. R. Carley, "A 1 mG lateral CMOS- MEMS accelerometer," in *Proc. 13th IEEE Int. Conf. Micro Electro Mechanical Systems (MEMS 2000)*, Japan, 2000, pp. 502-507.

[48] H. Xie and G. K. Fedder, "Vertical comb-finger capacitive actuation and sensing for CMOS-MEMS," *Sens. Actuators A Phys* vol. 95, pp. 212-221, 2002.

[49] A. E. Franke, J. M. Heck, K. Tsu-Jae, and R. T. Howe, "Polycrystalline silicon–germanium films for integrated microsystems," *J. Microelectromech. Syst*, vol. 12, pp. 160-171, 2003.

[50] H. Kulah, N. Yazdi, and K. Najafi, "A CMOS switched-capacitor interface circuit for an integrated accelerometer," in *Proc. 43rd IEEE Midwest Symp. Circuits and Systems*, Lansing, MI, 2000, pp. 244–247.

[51] J. Chae, H. K. H, and K. Najafi, "An in-plane high-sensitivity, low-noise micro-g silicon accelerometer with CMOS readout circuitry," *J. Microelectromech. Syst*, vol. 13, pp. 628-635, 2004.

[52] J. Wang and X. Li, "Monolithic-integrated silicon bulk-micromachined accelerometer and pressure-sensor for tire-pressure-monitoring-system (TPMS) application," in *2011 16th International Solid-State Sensors, Actuators and Microsystems Conference*, 2011, pp. 703-706.

[53] G. Li, Z. Li, C. Wang, Y. Hao, T. Li, D. Zhang, *et al.*, "Designand fabrication of a highly symmetrical capacitive triaxial accelerometer," *J. Micromech. Microeng*, vol. 11, pp. 48-54, 2001.

[54] H. Farahani, J. K. Mills, and W. L. Cleghorn, "Design, fabrication and analysis of micromachined high sensitivity and 0% cross-axis sensitivity capacitive accelerometers," *Microsystem Technologies*, vol. 15, pp. 1815-1826, Dec 2009.

[55] A. Witvrouw, R. Van Hoof, G. Bryce, B. Du Bois, A. Verbist, S. Severi, *et al.*, "SiGe MEMS Technology: a Platform Technology Enabling Different Demonstrators," *Sige, Ge, and Related Compounds 4: Materials, Processing, and Devices*, vol. 33, pp. 799-812, 2010.

[56] C. Comi, A. Corigliano, A. Ghisi, and S. Zerbini, "A resonant micro accelerometer based on electrostatic stiffness variation," *Meccanica*, vol. 48, pp. 1893-1900, Oct 2013.

[57] L. Lin, "MEMS post-packaging by localized heating and bonding," *IEEE Transactions on Advanced Packaging*, vol. 23, pp. 608-616, 2000.

[58] L. E. Felton, N. Hablutzel, W. A. Webster, and K. P. Harney, "Chip scale packaging of a MEMS accelerometer," in *Electronic Components and Technology Conference, 2004. Proceedings. 54th*, 2004, pp. 869-873 Vol.1.

[59] R. Zoberbier, M. Hennemeyer, D. Toennies, A. Kraft, M. Eisner, V. R, *et al.*, "Technology trends in the manufacturing and packaging of Wafer Level Cameras," in *Electronic System-Integration Technology Conference (ESTC), 2010 3rd*, 2010, pp. 1-5.

[60] N. Fujimori, T. Igarashi, T. Shimohata, T. Suyama, K. Yoshida, Y. Nakagawa, *et al.*, "Wafer level package by using post dicing process," in *Electronics Packaging (ICEP), 2014 International Conference on*, 2014, pp. 34-38.

[61] T. Braun, K. F. Becker, E. Jung, S. Voges, T. Thomas, R. Kahle, *et al.*, "Fan-out Wafer Level Packaging for MEMS and Sensor Applications," in *Sensors and Measuring Systems 2014; 17. ITG/GMA Symposium; Proceedings of*, 2014, pp. 1-5.

[62] J. H. Lau, C. Lee, C. S. Premachandran, and Y. Aibin, "Accelerometer Packaging," in *Advanced MEMS Packaging*, ed: McGraw-Hill 2010.

[63] H. Xie, G. K. Fedder, and R. E. Sulouff, "Accelerometers," in *Comprehensive Microsystems*, O. Tabata and H. Zappe, Eds., ed Oxford: Elsevier, 2008, pp. 135-180.

[64] T. B. Jones and N. G. Nenadic, "Practical MEMS devices," in *Electromechanics and MEMS*, ed: Cambridge University Press, 2013, p. 577.

[65] G. Krishnan, C. U. Kshirsagar, G. K. Ananthasuresh, and N. Bhat, "Micromachined High-Resolution Accelerometers," *Journal of the Indian Institute of Science,* vol. 87, pp. 333-361, September 2007.

[66] A. H. Nayfeh and M. I. Younis, "A new approach to the modeling and simulation of flexible microstructures under the effect of squeeze-film damping," *Journal of Micromechanics and Microengineering*, vol. 14, pp. 170–181, February 2004.

[67] W. Ye, W. Hemmert, D. Freeman, and J. White, "Air damping in laterally oscillating microresonators: a numerical and experimental study," *IEEE Journal of Microelectromechanical Systems,* vol. 12, pp. 557–566, October 2003.

[68] B. Bahreyni, "Damping Mechanisms," in *Fabrication and design oF resonant Microdevices*, ed: William andrew inc, 2008.

[69] V. Kaajakari, "Accelerometers," in *Practical MEMS: Analysis and design of microsystems, MEMS sensors, electronics, actuators, rf mems, optical mems, and microfluidic systems*, ed: Small Gear Publishing, 2009, p. 484.

[70] D. Choia, Y. Gea, James S. Harrisa, J. Cagnonb, and S. Stemmerb, "Low surface roughness and threading dislocation density Ge growth on Si (0 0 1)," *Journal of Crystal Growth,* vol. 310, pp. 4273–4279, August 2008.

[71] Y. Nonomura, M. Fujiyoshi, Y. Omura, N. Fujitsuka, K. Mizuno, and K. Tsukada, "SOI rate gyro sensor for automotive control," *Sensors and Actuators a-Physical,* vol. 132, pp. 42-46, Nov 2006.

[72] H. Seidel, M. Aikele, M. Rose, and S. Toelg, "Safety relevant microsystems for automotive applications," *Microsystem Technologies*, vol. 7, pp. 244-248, Jan 2002.

[73] Z. Fang, J. Zhang, and Y. Wang, "The HAL-3 airborne navigation radar," vol. 32, p. 1211, 1996.

[74] A. Buhmann, C. Peters, M. Cornils, and Y. Manoli, "A GPS aided Full Linear Accelerometer Based Gyroscope-free Navigation System," p. 629, 2006.

[75] W. Chenhao, H. Zhencheng, S. Kusuhara, and K. Uchimura, "Vehicle Localization with Global Probability Density Function for Road Navigation," p. 1038, 2007.

[76] A. M. Madni, L. E. Costlow, and S. J. Knowles, "Common design techniques for gyrochip quartz rate sensors for both automotive and aerospace/defense markets," *IEEE Sensors Journal,* vol. 3, pp. 2569–578, 2003.

[77] A. Lawrence, "Modern Inertial Technology," in *Navigation, Guidance, and Control*, ed New York: Springer-Verlag,, 1993.

[78] C. Acar, A. R. Schofield, A. A. Trusov, L. E. Costlow, and A. M. Shkel, "Environmentally Robust MEMS Vibratory Gyroscopes for Automotive Applications," *Sensors Journal, IEEE* vol. 9, pp. 1895 - 1906, Octobor 2009.

[79] C.-W. Tan, S. Park, K. Mostov, and P. Varaiya, "Design of gyroscope-free navigation systems," in *Intelligent Transportation Systems, 2001*, Oakland, CA, 2001, pp. 286 - 291.

[80] V. Kempe, "Gyroscopes," in *Inertial MEMS Principles and Practice*, ed New York: Cambridge University Press 2011, p. 492.

[81] Q. An, Y. Ishikawa, J. Nakagawa, A. Kuroda, H. Oka, H. Yamakawa, *et al.*, "Evaluation of wearable gyroscope and accelerometer sensor (PocketIMU2) during walking and sit-to-stand motions," in *2012 IEEE RO-MAN: The 21st IEEE International Symposium on Robot and Human Interactive Communication*, 2012, pp. 731-736.

[82] H. Zeng and Y. Zhao, "Sensing Movement: Microsensors for Body Motion Measurement," *sensors*, vol. 11, pp. 638-660, January 2011.

[83] S. Ayub, A. Bahraminisaab, and B. Honary, "A Sensor Fusion Method for Smart phone Orientation Estimation," in *13th Annual Post Graduate Symposium on the Convergence of Telecommunications, Networking and Broadcasting*, Liverpool, 2012.

[84] A. Noureldin, H. Tabler, D. Irvine-Halliday, and M. Mintchev, "Testing the applicability of fiber optic gyroscopes for azimuth monitoring for measurement-while-drilling processes in the oil industry," in *Position Location and Navigation Symposium, IEEE 2000*, San Diego, CA, 2000, pp. 291 - 298.

[85] Technavio. *Global Mems Gyroscope Market 2015-2019*. Available: http://www.technavio.com/report/global-mems-gyroscope-market-2015-2019

[86] EPSON. *Gyro sensors - How they work and what's ahead*. Available: http://www5.epsondevice.com/en/information/technical_info/gyro/

[87] D. Xia, C. Yu, S. Wang, H. Li, and K. Lun, "Structure design and simulation of micro dynamically tuned gyroscope with three equilibrium rings," in *Nano/Micro Engineered and Molecular Systems (NEMS), 2013 8th IEEE International Conference on*, 2013, pp. 965-968.

[88] N. Beverini, G. Carelli, E. Maccioni, J. Belfi, A. D. Virgilio, M. Pisani, *et al.*, "Ring laser gyroscope for accurate angle metrology," in *Laser Optics, 2014 International Conference*, 2014, pp. 1-1.

[89] A. A. Trusov, G. Atikyan, D. M. Rozelle, A. D. Meyer, S. A. Zotov, B. R. Simon, *et al.*, "Flat is not dead: Current and future performance of Si-MEMS Quad Mass Gyro (QMG) system," in *2014 IEEE/ION Position, Location and Navigation Symposium - PLANS 2014*, 2014, pp. 252-258.

[90] A. A. Trusov, I. P. Prikhodko, S. A. Zotov, A. R. Schofield, and A. M. Shkel, "Ultra-high Q silicon gyroscopes with interchangeable rate and whole angle modes of operation," in *Sensors, 2010 IEEE*, 2010, pp. 864-867.

[91] R. Maimon, O. Lahav, Y. Gerson, O. Zohar, H. Berko, and S. Krylov, "Tactical grade micro gyroscope with dual capcitive/optical sensing," in *Micro Electro Mechanical Systems (MEMS), 2013 IEEE 26th International Conference on*, 2013, pp. 637-640.

[92] C. Jin, C. Mei, L. Xiaoqin, H. Wei, and D. Zhantao, "Simulation Analysis of a Symmetrical Micromachined Vibratory Rate Gyroscope," in *Instrumentation, Measurement, Computer, Communication and Control (IMCCC), 2012 Second International Conference on*, 2012, pp. 482-485.

[93] TronicsMicrosystems. *High Performance MEMS Gyros*. Available: http://www.tronicsgroup.com/High-Performance-MEMS-Gyros

[94] Sensonor. *Gyro sensors*. Available: http://www.sensonor.com/gyro-products/gyro-sensors.aspx

[95] S. Donner. *Gyroscopes*. Available: http://www.systron.com/inertial-sensors/single-axis-gyroscope

[96] J. Mizuno, K. Nottmeyer, Y. Kanai, O. Berberig, and T. Kobayashi, "A silicon bulk micromachined crash detection sensor with simultaneous angular and linear sensitivity," *IEEE Transducers*, pp. 1302–1305, 1999.

[97] B. Trayner, "Introduction to the noninertial quality rate gyroscope and its applications," presented at the Optoelectronics, IEE Proceedings J 2008.

[98] F. Ayazi, M. Faisal Zaman, and A. Sharma, "Vibrating Gyroscopes," in *Comprehensive Microsystems*, O. Tabata and H. Zappe, Eds., ed Oxford: Elsevier, 2008, pp. 181-208.

[99] P. Greiff, B. Boxenhorn, T. King, and L. Niles, "Silicon monolithic micromechanical gyroscope," in *Solid-State Sensors and Actuators, 1991. Digest of Technical Papers, TRANSDUCERS '91., 1991 International Conference on*, 1991, pp. 966-968.

[100] M. Weinberg, J. Bernstein, S. Cho, A. T. Kin, A. Kourepenis, P. Maciel, *et al.*, "A Micromachined Comb-Drive Tunning Fork Gyroscope," *Institute of Navigation*

Proceedings of the 49th Annual Meeting: Future Global Navigation and Guidance, pp. 595-601, 1993.

[101] T. Juneau, A. P. Pisano, and J. H. Smith, "Dual axis operation of a micromachined rate gyroscope," in *Solid State Sensors and Actuators, 1997. TRANSDUCERS '97 Chicago., 1997 International Conference on*, 1997, pp. 883-886 vol.2.

[102] W. A. Clark, R. T. Howe, and R. Horowitz, "Surface micromachined z-axis vibratory rate gyroscope," presented at the Solid-state sensor and actuator Workshop, Hilton Head Island, SC, USA, 1996.

[103] Analog-Devices. *New iMEMS® Angular-Rate-Sensing Gyroscope*. Available: http://www.analog.com/library/analogDialogue/archives/37-03/gyro.html

[104] K. Park, C. Lee, Y. Oh, and Y. Cho, "Laterally oscillated and forcebalanced micro vibratory rate gyroscope supported by fish hook shape springs," in *IEEE Micro Electro Mechanical Systems Workshop (MEMS '97)*, Nagoya, Japan, 1997, pp. 494–513.

[105] H. Guohong and K. Najafi, "A single-crystal silicon vibrating ring gyroscope," in *Micro Electro Mechanical Systems, 2002. The Fifteenth IEEE International Conference on*, 2002, pp. 718-721.

[106] F. Ayazi and K. Najafi, "High aspect-ratio combined poly and single-crystal silicon (HARPSS) MEMS technology," *Journal of Microelectromechanical Systems*, vol. 9, pp. 288-294, Sep 2000.

[107] A. Sharma, M. F. Zaman, and F. Ayazi, "A 0.2Â°/hr Micro-Gyroscope with Automatic CMOS Mode Matching," p. 610, 2007.

[108] P. Qu and H. W. Qu, "Design and Characterization of a Fully Differential MEMS Accelerometer Fabricated Using MetalMUMPs Technology," *Sensors*, vol. 13, pp. 5720-5736, May 2013.

[109] K. Azgin, Y. Temiz, T. Akin, and Ieee, "An SOI-MEMS tuning fork gyroscope with linearly coupled drive mechanism," in *Proceedings of the Ieee Twentieth Annual International Conference on Micro Electro Mechanical Systems, Vols 1 and 2*, ed New York: Ieee, 2007, pp. 482-485.

[110] S. Lewis, S. Alie, T. Brosnihan, C. Core, T. Core, R. Howe, *et al.*, *Integrated sensor and electronic processing for > 10 boolean AND 8 "iMEMS" inertial measurement unit components*. New York: Ieee, 2003.

[111] J. Geen and D. Krakauer. (2003). *New iMEMS® Angular-Rate-Sensing Gyroscope*. Available: http://www.analog.com/library/analogDialogue/archives/37-03/gyro.html

[112] L. Prandi, C. Caminada, L. Coronato, and G. Cazzaniga, "A low-power 3-axis digital-output MEMS gyroscope with single drive and multiplexed angular rate readout," presented at the Solid-State Circuits Conference Digest of Technical Papers (ISSCC) 2011 IEEE International, San Francisco, CA, 2011.

[113] J.-P. Guan and X.-M. Liu, "Improved Design and Modeling of Micromachined Tuning Fork Gyroscope Characterized by High Quality Factor," *Journal of Electronic Science and Technology* vol. 8, pp. 280-286, September 2010.

[114] C. Acar and A. Shkel, *MEMS Vibratory Gyroscopes, Structural Approaches to Improve Robustness*: Springer Science+Business Media, 2009.

CHAPTER -2

2. MIDIS Microfabrication Platform for Inertial Sensors

Over the past two decades, various standard fabrication platforms have been developed by pure-play MEMS foundries for the purpose of large-scale mass-production of MEMS devices. A pure-play MEMS foundry is a facility that is open to manufacturing for other companies and institutions. Many of these commercial MEMS fabrication processes offer Multi-Project Wafer (MPW) service. MPW service allows low-cost access to prototype and medium volume quantities of custom MEMS designs by aggregating multiple user designs onto one mask set. The MPW processes from pure-play foundries include both surface and bulk micromachining techniques along with the inclusion of high aspect ratio processing using Deep Reactive Ion Etching (DRIE)[1].

Regardless the features and specifications that characterize any particular fabrication platform, a well-developed MPW process offers the ability to grow and pattern thin-film and bulk materials involved in the MEMS fabrication using well-studied and optimized recipes parameters [2]. This allows to define a standard set of design rules that facilitate the estimation of MEMS sensor metrology characteristics according to the specific fabrication capability. Thus, the use of standard MEMS fabrication processes require significant attention paid at the design stage where the design rules and the capability in each fabrication phase is particularly considered during the design development.

Following the approach of using a standard microfabrication process for MEMS development, offers many advantages including, a significantly short development timeline [3-

5], low cost of development by sharing the fabrication cost with other users involved in the MPW service [6], and finally, taking advantage of optimized microfabrication process with high manufacturing yield [7]. Figure 2.1 shows the world's top 20 MEMS foundries players ranking according to the sales revenues.

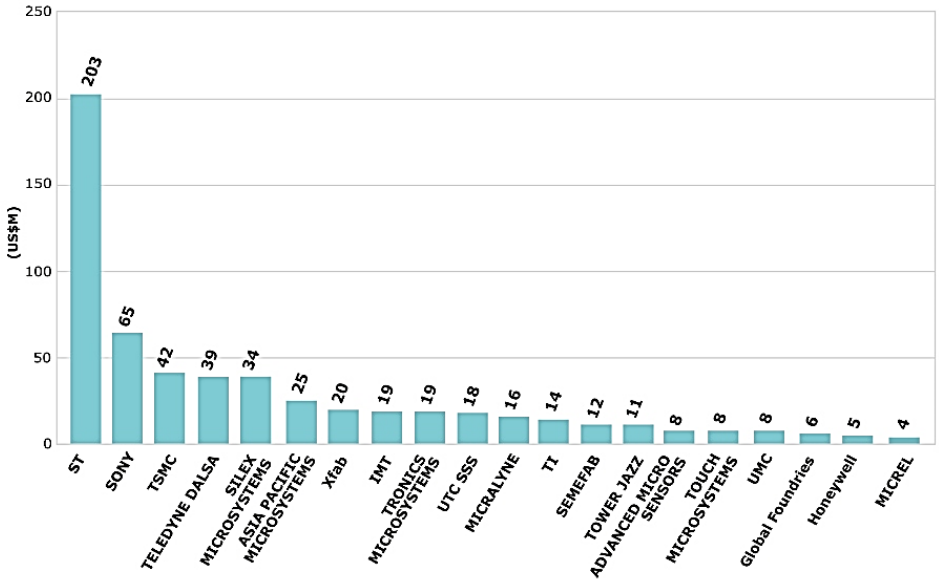

Figure 2.1 Top 20 MEMS foundry ranking [8].

It is generally agreed that the microfabrication process needed to develop a MEMS device technology is specific to the design, but a number of commercial standard microfabrication processes are now available that are made application specific, such as for inertial sensors, pressure sensors, or thermal sensor fabrication. In the following section, some well-known and widely used foundry processes will be described. In particular, the MIDIS fabrication process from TDSI will be described in detail by describing its important features and fabrication process flow. The main specifications in each fabrication step will be described.

2.1. Commercial Fabrication Processes

2.1.1. Examples of Commercial MPW Platforms

A plethora of standard fabrication processes with useful properties have emerged over the past two decades. Amongst, the MEMSCAP foundry, with locations in France and USA, provides standard and custom innovative MEMS based fabrication solutions suitable for various market segments such as aerospace, medical/biomedical and telecommunications [9]. The Multi-User MEMS Processes (MUMPs) is a MPW platform from MEMSCAP that enables MEMS prototyping and low volume production through four different processes, PolyMUMPs, SOIMUMPs, MetalMUMPs and PiezoMUMPs [9].

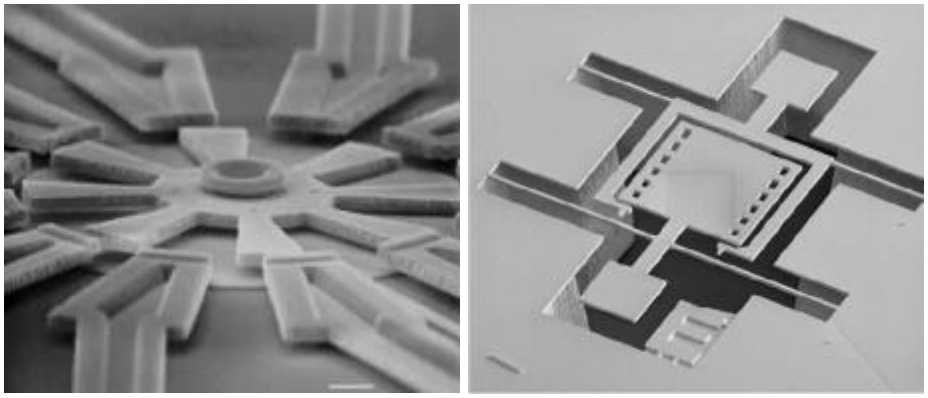

(a) (b)

Figure 2.2 Scanning Electron Microscope (SEM) images of (a) PolyMUMPs process and (b) SOIMUMPs process [10].

The PolyMUMPs is surface micromachining process that enables the creation of suspended structures of polycrystalline silicon (polysilicon) by removing the sacrificial layers (i.e., silicon dioxide). Acoustic sensors (e.g., microphone), accelerometers, microfluidic devices and display technology are the main types of devices fabricated using PolyMUMPs process [11-13]. SOIMUMPS is a high aspect ratio fabrication process where Silicon-on-Insulator (SOI) wafer is patterned up to the oxide layer through Deep Reactive Ion Etching (DRIE). A shadow mask metal process is used to provide coarse metal structures such as bonding pads, electrical

connections and optical mirror surfaces [14]. Bond pads are created through the deposition of second metal layer. The minimum feature size is equal to 2μm with structural layer thickness of either 10μm or 25μm which allows the fabrication of inertial sensors like gyroscopes and accelerometers, whereas the through-hole capability and mirror surfaces can be used to design MOEMS devices for display technology [14]. Figure 2.2 illustrates SEM views for both SOIMUMPs and PolyMUMPs fabrication processes.

In 2013, MEMSCAP introduced a new process called PiezoMUMPs process. Based on a SOIMUMPs process (10μm silicon thickness) it adds a 0.5 μm Aluminum Nitride piezoelectric layer on top of the silicon structural layer. PiezoMUMPs process can be very useful for energy harvesting applications where active piezoelectric devices (e.g., piezoelectric actuators) can be fabricated.

ST-Microelectronics introduced Thick Epitaxial Layer based fabrication process designed specifically for the fabrication of inertial sensors like gyroscopes and accelerometers. This process is termed as Thick Epitaxial Layer for Micro gyroscope and Accelerometer (THELMA) process [15, 16]. This technology is widely used to fabricate MEMS devices in consumer products such as smartphones, tablets, video cameras and gaming. One important feature in ST-Microelectronics's THELMA process is the use a cap wafer bonded to the top wafer which allows the protection of the moving mechanical structures. The encapsulation process is made with nitrogen gas which provide acceptable stability for the resonant frequency. Figure 2.3 shows the different layers involved in THELMA fabrication process.

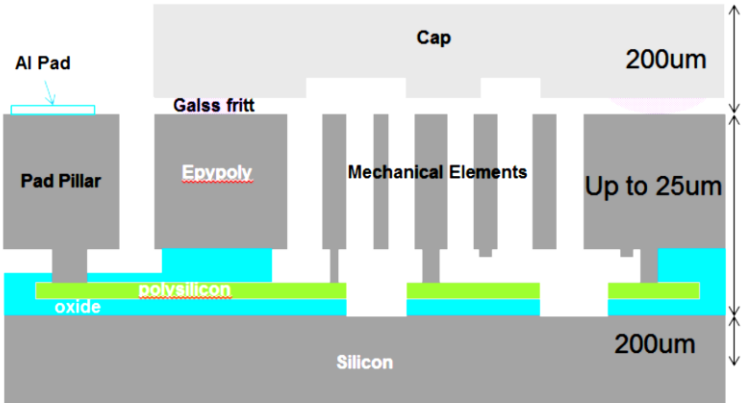

Figure 2.3 Cross section view of THELMA process [17].

The Micragem and Micragem-SI fabrication processes were developed by Micralyne Inc., Edmonton, Alberta, Canada [18]. These technologies allow the creation of suspended MEMS devices using single crystal silicon with metal electrodes for Input/Output. The process is considered flexible because it allows the designer to vary the gap sizes between layers. Micragem includes a variety of MEMS devices suitable for different applications in telecommunications, micro-assembly, and inertial navigation for aerospace and automobiles [19, 20]. Figure 2.4 depicts a cross section view of Micragem-SI fabrication process.

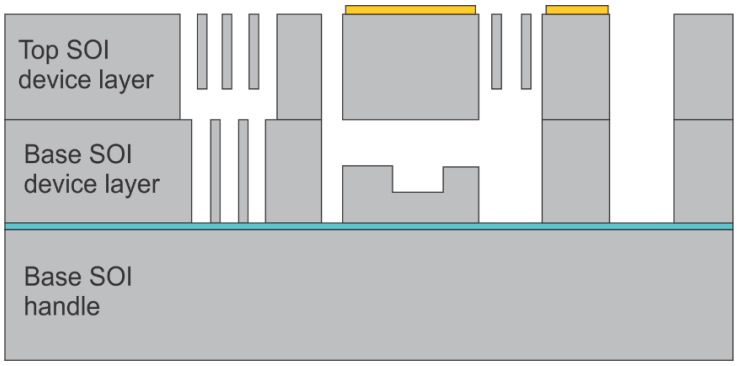

Figure 2.4 Cross section view of Micragem process [19].

NASIRI-FABRICATION is a fabrication platform built by InvenSense and designed for the development of inertial sensors. The important features that characterize the NASIRI-Fabrication process include, (1) the use of single crystal silicon as structural layer, (2) wafer

level integration with CMOS electronics, (3) and a cost effective wafer level packaging technique (WLP) [21]. The InvenSense technology addresses a wide variety of MEMS devices for use in consumer products (e.g., smart phone, tablets, gaming consoles, and smart TVs) and motion sensors for position tracking purpose in free space [21]. Figure 2.5 depicts a cross section view of Nasiri-Fabrication process.

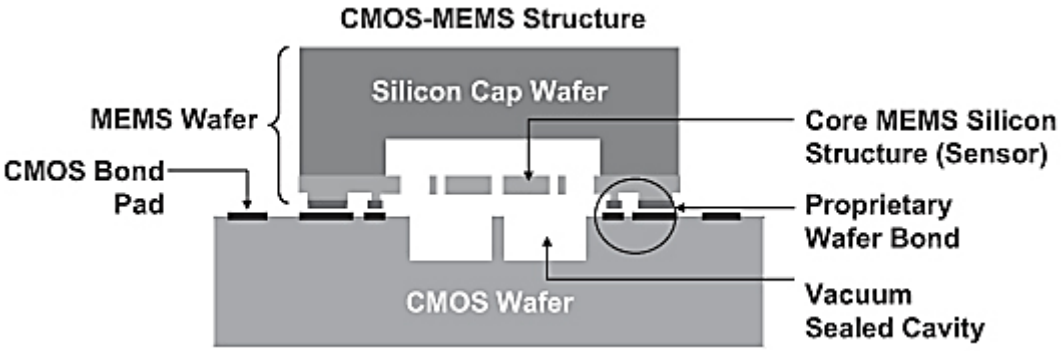

Figure 2.5 Cross section view of Nasiri-Fabrication process [22]

2.1.2. MIDIS Process

The MEMS Integrated Design for Inertial Sensors (MIDIS) platform has been developed by Teledyne DALSA Semiconductor Inc. (TDSI) in 2013. The process is specifically designed for inertial sensors fabrication such as gyroscopes and accelerometers and provides the world's leading ultra-clean wafer-level vacuum encapsulation process. The MIDIS technology platform helps to significantly reduce the overall die size with the availability of Through Silicon Vias (TSVs) [23]. The encapsulation process in MIDIS is getter-free which improves reliability and lowers cost to attain high Q for resonators and vibratory gyroscopes devices (Q > 20,000) along with optimal air damping for accelerometers [23]. Furthermore, the structural layer height control can be used for out-of-plane sensing. In summary, the MIDIS process addressed some key challenges for the design and development of inertial sensors including, low cost, high reliability, high performance and fast time-to-market [23]. Figure 2.6 shows Scanning Electron

Microscope (SEM) cross-sectional image of encapsulated micromechanical resonator under high vacuum.

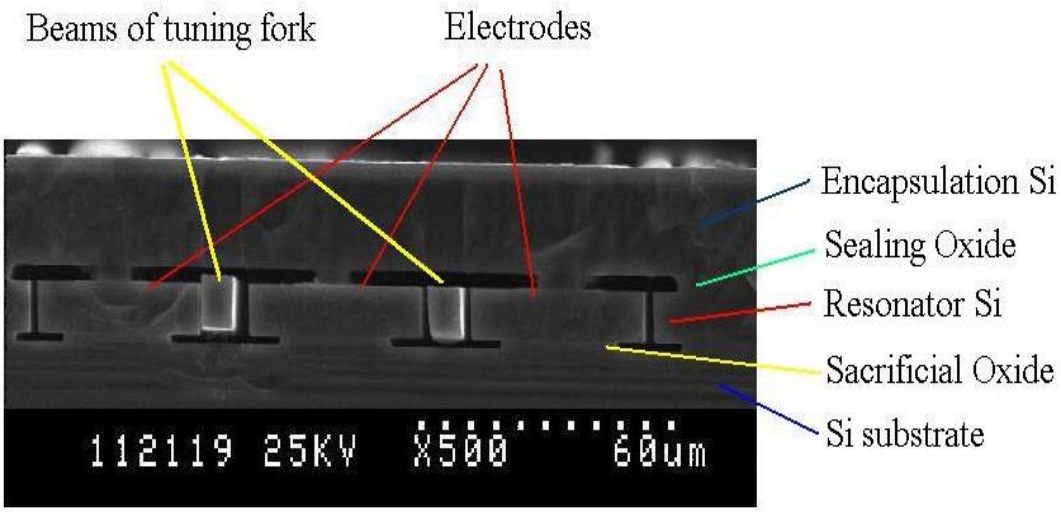

Figure 2.6 SEM cross-section image of encapsulated micromechanical resonator [24].

Unlike most other approaches where the electrical connections between MEMS devices and Integrated Circuits (ICs) are built using wire bonding, MIDIS process allows "Above IC" integration, which results in a compact microsystem with high reliability. In the following Section, a detailed description of the MIDIS flow process is presented. Figure 2.7 illustrates the different layers involved in MIDIS fabrication process.

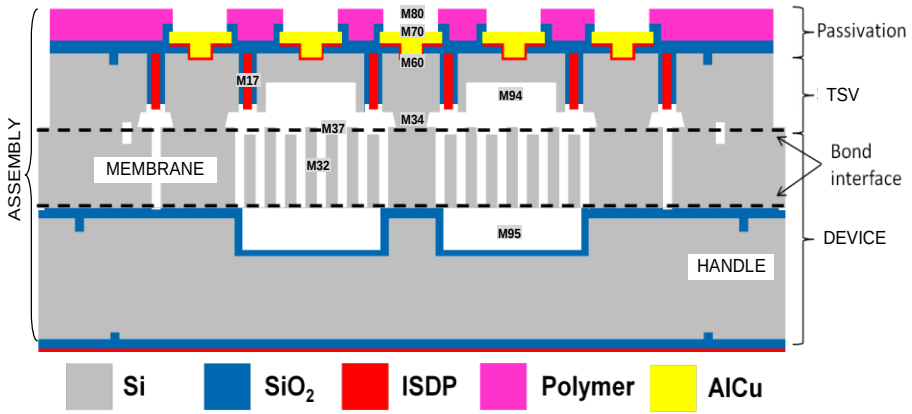

Figure 2.7 Process cross-section with substrates and masks identification [23].

2.1.3. Process flow

The MIDIS platform is a high aspect ratio bulk micromachining process of a 30 μm thick single-crystal silicon device layer that is vacuum encapsulated at 10 mTorr between two silicon wafers. The bottom wafer (or handle wafer) has a thickness of 380 μm. The top wafer (or interconnect wafer) has a thickness of 108 μm. The interconnect wafer includes Through-Silicon Vias (TSVs) to create electrically isolated connections to the device wafer. The process begins by patterning the bottom wafer using a Deep Reactive Ion Etching (DRIE) process to create 30 μm deep silicon cavities in the handle wafer. The MEMS devices will be suspended over these regions. The surface is then protected by a 1.1 μm thermally grown layer of silicon oxide. The silicon oxide is used to protect the bottom wafer during further processing, as well as, provide electrical isolation to the MEMS device. In the next step, the 30 μm thick silicon device wafer is fusion bonded onto the handle wafer. To facilitate this process, the 30 μm device wafer is placed on its own handling wafer in a Silicon on Insulator (SOI) like configuration. Heat and pressure are applied to fuse the device wafer to the handle wafer. The 30 μm thick device layer is then isolated from its wafer using Chemical Mechanical Polishing (CMP) and SiO_2 etching. The device wafer is patterned in order to prepare the wafer for a DRIE step.

The features are aligned over the bottom wafer cavities by using markings on the backside. The DRIE etch step etches through the 30 μm device wafer releasing the structures. This step is also used to electrically isolate the structures within the device wafer. This DRIE etch step is performed with a Bosch process using SF_6 as the etchant and a Teflon like polymer to protect the side walls and create vertical profiles. The 1.1 μm thermal oxide layer on the bottom handle wafer is used as an etch stop for this DRIE step. The top wafer has undergone bulk micromachining steps in order to prepare the top wafer for fusion bonding with the device wafer. The top interconnect wafer is etched on the bond side and then processed from the top

of the wafer. In MIDIS platform, the bonding plane is isolated by placing a protective layer and performing a 2 μm anisotropic wet etch of the exposed silicon wafer.

In order to provide an electrically isolated path to the encapsulated MEMS device Through Silicon Vias (TSVs) are built onto the interconnect wafer. The channels necessary for TSVs are etched using a DRIE like process are then filled with In Situ Doped Silicon (ISDP) and a layer of silicon dioxide. After this step, the bond side patterning profile is complete and the top wafer is flipped to work on the final interconnect formation steps before bonding. Figure 2.8 presents the main principle steps involved in MIDIS process.

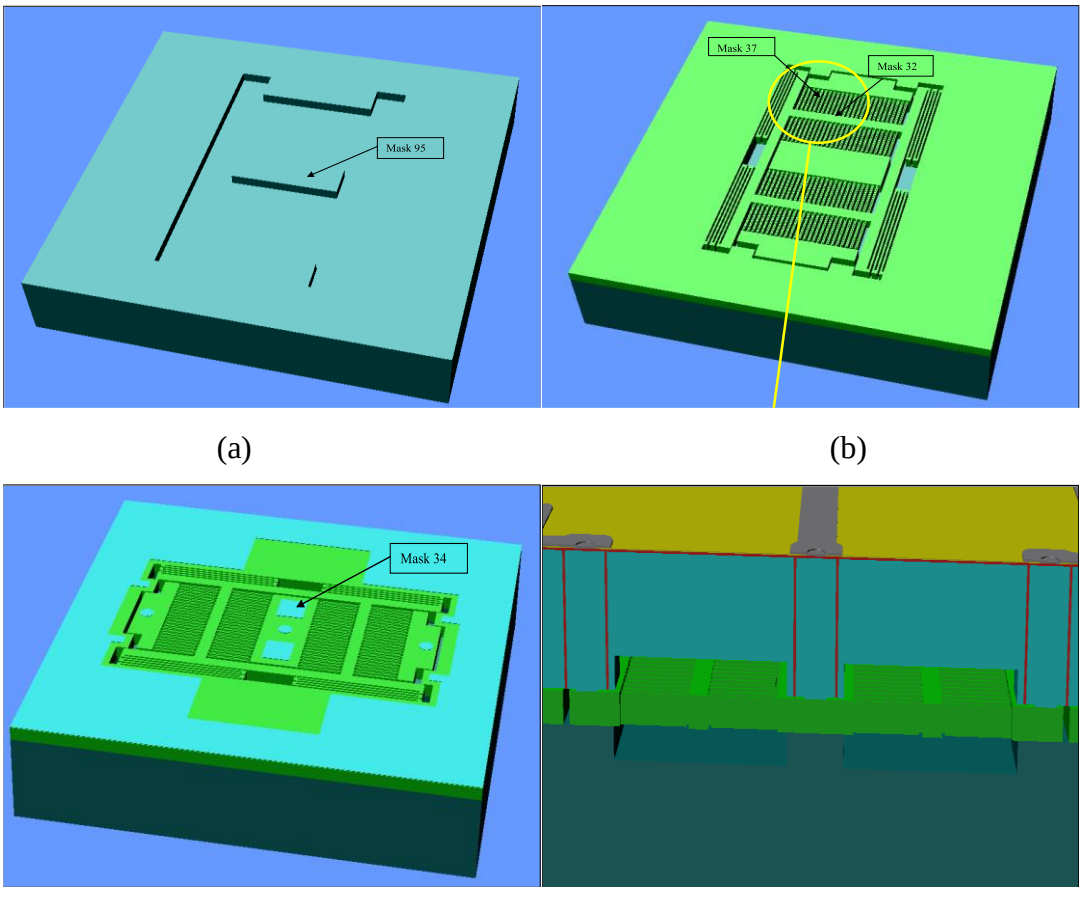

(a) (b)

(c) (d)

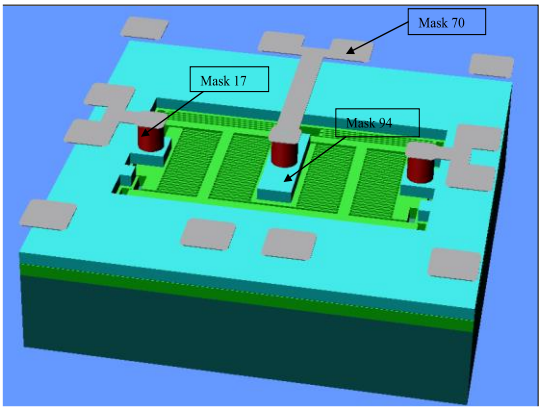

(e)

Figure 2.8 The main processing steps in MIDIS process: (a) Handle layer patterning followed by thermal oxidation, (b) Three silicon wafers stacking and patterning, (c) Bonding layer plane stacking and patterning, (d) Silicon-to-silicon fusion bonding and TSV forming [23].

2.1.4. MIDIS Features

The MIDIS process uses single-crystal silicon device layer which provide mechanical reproducible results and is less sensitive to thermal mismatch. The device layer thickness is controllable to be either 22μm to 30μm depending on the application. The thick structural device layer offers a heavy proof mass that significantly increases the sensor sensitivity and provides a better immunity from noise. Furthermore, the MIDIS process includes the ability to move the proof mass along different axes including the out-of-plane direction. In summary, the MIDIS process uses a combination of surface and bulk micromachining techniques and takes advantages from both approaches.

The MIDIS process is a unique microfabrication process as it offers ultra-clean wafer-level vacuum packaging. With MIDIS, the MEMS device is hermetically encapsulated under a high vacuum pressure of 10 mTorr. This vacuum level is attained during the bonding process. The total leak rate equivalent in the MIDIS process is as low as 45 molecules/s ($7.5x10^{-13}$ atm·cc/s)

that is several orders of magnitude better than Military-Standard 883H (10^{-9} atm·cc/s or 61,500 molecules/s), which is commonly accepted by industry [23]. The materials used during the bonding process do not outgas which eliminates the use of getter materials.

Vibratory inertial sensors require high quality vacuum packaging as different damping mechanisms including, thermoelastic dissipation (TED), surface loss, and air damping, can cause nonlinear effects in the sensor response and affect the proof-mass velocity and bias instability in gyroscopes. Both, accelerometers and vibratory gyroscopes requires high vacuum pressure in order to decrease the damping effect and consequently attain a high Quality factor (Q). Further, the use of high vacuum packaging helps to maintain a stable and constant damping factor while working under high temperature which improves significantly the bias stability as well as the dynamic response of the system.

2.2. MEMS packaging: Wafer Level Packaging (WLP)

Packaging represents an important key factor that determines the performance of MEMS devices, and ultimately, the MEMS device success in commercialization. The main functions realized by MEMS packaging include:

- Protection of MEMS device from the surrounding environment to insure high reliability and long term operation.
- The supply of electrical connections to the devices and/or interface circuits placed inside the sealed cavity, which provides the necessary electrical power and allows the data acquisition.
- Proper packaging helps to minimize damping and energy losses.

The current trend in packaging technology aims to minimize the overall product cost, enhance the yield, and insure the required reliability of the whole integrated microsystem. Here, Wafer Level Packaging (WLP) is very relevant technique that insures a low device cost thanks to batch processing with high yield and fewer assembly process steps. Further, WLP enables reduced die size through the integration of many devices into a single package by vertically stacking multiple devices with different functions. Current technology allows vertical interconnects or Through Silicon Vias (TSVs) that facilitates the design implementation and heterogeneous integration with a low parasitic capacitance and impedance. [25, 26].

There are three commonly used techniques used to create TSVs interconnects [26]:

- TSV with sacrificial wafer: This technique consists of deep trench etching followed by thin oxide layer growth by thermal oxidation. Additional layer of metal (Ti/TiN) is deposited over the oxide to make a good adhesion between the filled insulating layer (oxide) and the filled material in the TSV. The TSV wafer is bonded to the sacrificial wafer through a seed layer of gold (Au) that acts as intermediate layer. The patterned capping wafer is then aligned and bonded to the MEMS's wafer.

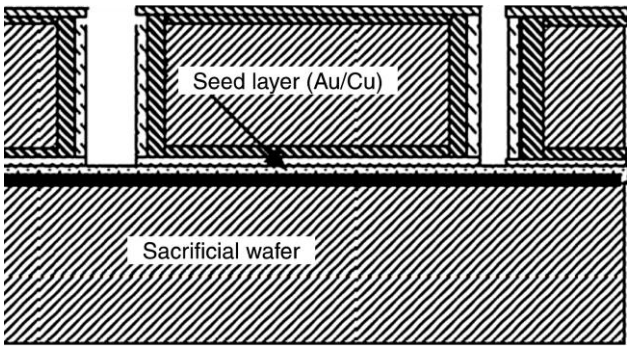

Figure 2.9 TSV formation with sacrificial wafer [26].

- TSV without sacrificial wafer: This technique does not necessitate a sacrificial wafer to create the TSVs. A seed layer is deposited on the backside of the capping wafer and

TSVs are then patterned and etched followed by oxide filling. Additionally, polishing and planarization processes can be performed on both sides of the capping wafer.

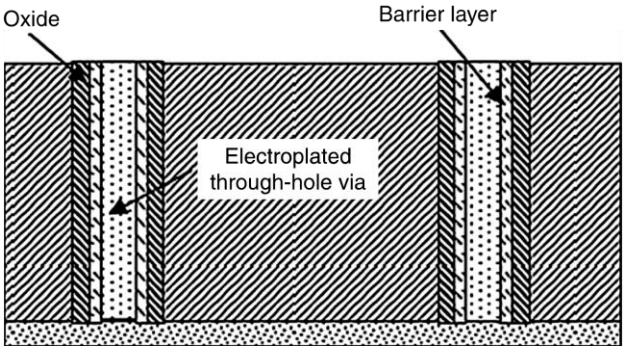

Figure 2.10 TSV creation without sacrificial wafer [26].

- TSV with MEMS wafer: The MEMS wafer and the capping wafer are bonded directly with fusion bonding process and then the TSVs are created followed by the formation of metallic pads for interconnections with external interface circuits. One important advantage of this method is that the cap wafer is more robust during the bonding process than in the preceding techniques cited above. This method is believed as an effective solution due to its simplicity, higher reliability and cost-effectiveness.

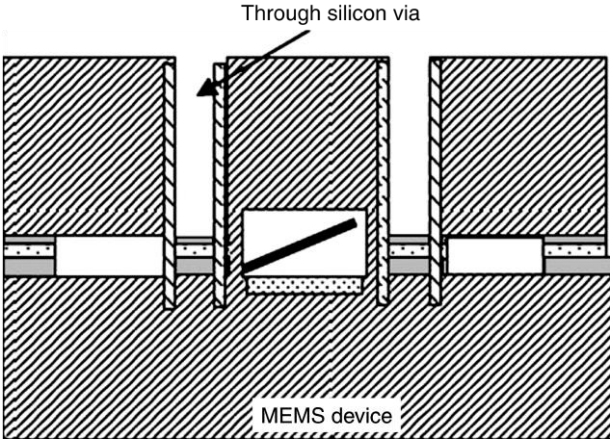

Figure 2.11 TSV creation with MEMS wafer [26]

Many vacuum packaging techniques use getter materials inside the sealed cavities, which is an important factor that enables the absorption of the outgassing gases inside the cavity to

maintain high vacuum. This method requires getters activation through either heating mechanism or by passing a current through the getter. The performance of the inertial sensors is measured mainly by its *Q* in vacuum where the damping mechanism and air-resistance are drastically minimized. With the use of WLP technology, the encapsulation pressure in MIDIS process can reach pressure of less than 10 mTorr.

Another important parameter concerns the stress issue that exists, particularly, during the bonding process at wafer level due the mismatch in the coefficient of thermal expansion (CTE). This problem can be minimized in MIDIS process thanks to the use of silicon-to-silicon bonding process. However, high stress can be generated in TSVs as in silicon surrounding the metal or the oxide material, which can cause micro-cracks that can considerably affect the reliability of the MEMS devices. Several methods can be used to minimize this stress by designing TSVs with smaller diameters, by properly choosing filling materials with comparable CTE or employing thick buffer polymer material between copper and silicon instead of using oxide thin layer to form polymer clad TSV [27-29].

Finally, the last parameter involved in the packaging assembly is related to electrical interconnects. Many techniques are used such as wire bonding, Tape Automated Bonding (TAB) and flip chip bonding. However, flip chip bonding called also Direct Chip Attach (DCA) includes many advantages, namely, reduced size, better electrical connections performance, rugged mechanical connections, low cost interconnection method and flexibility in pad placements [30]. The DCA technique involves direct attachment of the MEMS die face-down onto the integrated circuit through conductive bumps placed on the die bond pads [30].

2.3. Conclusions

In this chapter, various commercial standard MEMS microfabrication platforms are presented. An in-depth description of the MIDIS process from TDSI in presented. The main features and specifications of each process are illustrated. The importance of high vacuum packaging is emphasized for the development of inertial sensors. These features constitute the basis for the development of the inertial sensors to be described in the next Chapters 3, 4 and 5.

References

[1] A. A. Trusov, I. P. Prikhodko, S. A. Zotov, A. R. Schofield, and A. M. Shkel, "Ultra-high Q silicon gyroscopes with interchangeable rate and whole angle modes of operation," in *Sensors, 2010 IEEE*, 2010, pp. 864-867.

[2] J. A. Kubby, *A Guide to Hands-on MEMS Design and Prototyping*: Cambridge: Cambridge University Press, 2011.

[3] R. B. Lin, M. C. Wu, and S. C. Tsai, "Reticle Design for Minimizing Multiproject Wafer Production Cost," *IEEE Transactions on Automation Science and Engineering*, vol. 4, pp. 589-595, 2007.

[4] "IBM lowers cost of prototype and small-volume SiGe with Multi-Project Wafer programme," *III-Vs Review*, vol. 14, p. 16, 2001/05/01 2001.

[5] W. Meng-Chiou and L. Rung-Bin, "Multiple project wafers for medium-volume IC production," in *2005 IEEE International Symposium on Circuits and Systems*, 2005, pp. 4725-4728.

[6] A. E. J. Lim, J. Song, Q. Fang, C. Li, X. Tu, N. Duan, *et al.*, "Review of Silicon Photonics Foundry Efforts," *IEEE Journal of Selected Topics in Quantum Electronics*, vol. 20, pp. 405-416, 2014.

[7] A. Merdassi, M. N. Kezzo, G. Xereas, and V. P. Chodavarapu, "Wafer level vacuum encapsulated tri-axial accelerometer with low cross-axis sensitivity in a commercial MEMS Process," *Sensors and Actuators A: Physical*, vol. 236, pp. 25-37, 2015.

[8] EETimes. *TSMC races up MEMS foundry ranking*. Available: http://www.eetimes.com/document.asp?doc_id=1263205

[9] MEMSCAP. *MUMPs*. Available: http://www.memscap.com/products/mumps

[10] EuroPractice, "MEMSCAP MUMPs technology introduction."

[11] R. Grixti, I. Grech, O. Casha, J. M. Darmanin, E. Gatt, and J. Micallef, "Feasibility study of a MEMS microphone design using the PolyMUMPs process," in *Design, Test, Integration and Packaging of MEMS/MOEMS (DTIP), 2014 Symposium on*, 2014, pp. 1-4.

[12] R. I. Rincon, R. Ambrosio, J. Mireles, and A. Jimenez, "Differential capacitive accelerometer fabricated with PolyMUMP's technology: Design and characterization," in *Semiconductor Device Research Symposium, 2009. ISDRS '09. International*, 2009, pp. 1-2.

[13] L. Ki Bang and L. Liwei, "Surface micromachined glass and polysilicon microchannels using MUMPs," in *Micro Electro Mechanical Systems, 2003. MEMS-03 Kyoto. IEEE The Sixteenth Annual International Conference on*, 2003, pp. 578-581.

[14] A. Cowen, G. Hames, D. Monk, S. Wilcenski, and B. Hardy, *SOIMUMPs Design Handbook*, 2011.

[15] A. Briffa, E. Gatt, J. Micallef, I. Grech, O. Casha, and J. M. Darmanin, "Area minimization of a three-axis separate mass capacitive accelerometer using the ThELMA process," in *EUROCON, 2013 IEEE*, 2013, pp. 2094-2099.

[16] EE-Times. (2014). *ST extends Thelma MEMS process*. Available: http://www.electronics-eetimes.com/news/st-extends-thelma-mems-process

[17] I. Hirama, "New MEMS sensor process by TSV technology for smaller packaginge," in *Electronics Packaging and iMAPS All Asia Conference (ICEP-IACC), 2015 International Conference on*, 2015, pp. 456-459.

[18] Micralyne. (2016). *MicraGEM-Si™ – SOI MEMS Process*. Available: http://www.micralyne.com/technology-platforms/micragem-si/

[19] EuroPractice. *Micralyne MicraGEM-Si technology*. Available: http://www.europractice-ic.com/MEMS_micralyne.php

[20] H. K. Chu, J. K. Mills, and W. L. Cleghorn, "MEMS capacitive force sensor for use in microassembly," in *2008 IEEE/ASME International Conference on Advanced Intelligent Mechatronics*, 2008, pp. 797-802.

[21] A. D. Oliver, Y. L. Teo, A. Geisberger, R. F. Steimle, T. Cassagnes, K. Adhikari, *et al.*, "A new three axis low power MEMS gyroscope for consumer and industrial applications," in *2015 Transducers - 2015 18th International Conference on Solid-State Sensors, Actuators and Microsystems (TRANSDUCERS)*, 2015, pp. 31-34.

[22] W. Commons. *InvenSense NasiriFabrication*. Available: https://commons.wikimedia.org/wiki/File:InvenSense_NasiriFabrication_WithText.png

[23] TeledyneDALSA. *MIDIS Platform for Motion Sensors*. Available: http://www.teledynedalsa.com/semi/mems/applications/midis/

[24] F. Serrano-Vazquez, A. Herrera-May, and M. Bandala-Sanchez, "Design and modeling of a single-mass biaxial capacitive accelerometer based on the SUMMiT V process," *Microsystem Technologies-Micro-and Nanosystems-Information Storage and Processing Systems*, vol. 19, pp. 1997-2009, Dec 2013.

[25] L. G. Wang, A. Bos, T. van Weelden, and F. Boschman, "The Next Generation advanced MEMS & Sensor Packaging," *2010 11th International Conference on Electronic Packaging Technology & High Density Packaging (Icept-Hdp)*, pp. 55-60, 2010.

[26] J. H. Lau, C. Lee, C. S. Premachandran, and Y. Aibin, *Advanced MEMS Packaging*. United States: McGraw-Hill Companies, Inc, 2010.

[27] T. M. Bauer, S. L. Shinde, J. E. Massad, D. L. Hetherington, and Ieee, *Front End of Line Integration of High Density, Electrically Isolated, Metallized Through Silicon Vias*. New York: Ieee, 2009.

[28] D. Malta, C. Gregory, M. Lueck, D. Temple, M. Krause, F. Altmann, *et al.*, "Characterization of Thermo-Mechanical Stress and Reliability Issues for Cu-Filled TSVs," *2011 Ieee 61st Electronic Components and Technology Conference (Ectc)*, pp. 1815-1821, 2011.

[29] M. S. Parekh, P. A. Thadesar, M. S. Bakir, and Ieee, "Electrical, Optical and Fluidic Through-Silicon Vias for Silicon Interposer Applications," *2011 Ieee 61st Electronic Components and Technology Conference (Ectc)*, pp. 1992-1998, 2011.

[30] S. Beeby, G. Ensell, M. Kraft, and N. White, *MEMS Mechanical Sensors*. Boston: Artech House, Inc, 2004.

CHAPTER -3

3. A Wafer Level Vacuum Encapsulated Capacitive Accelerometer Fabricated in an Unmodified Commercial MEMS Process

We present the design and fabrication of a single axis low noise accelerometer in an unmodified commercial Micro-Electro-Mechanical Systems (MEMS) process. The new microfabrication process, MEMS Integrated Design for Inertial Sensors (MIDIS), introduced by Teledyne DALSA Inc. allows wafer level vacuum encapsulation at 10 mTorr which provides a high Quality factor and reduces noise interference on the MEMS sensor devices. The MIDIS process is based on high aspect ratio bulk micromachining of single-crystal silicon layer that is vacuum encapsulated between two other silicon handle wafers. The process includes sealed Through Silicon Vias (TSVs) for compact design and flip-chip integration with signal processing circuits. The proposed accelerometer design is sensitive to single-axis in-plane acceleration and uses a differential capacitance measurement. Over ±1 g measurement range, the measured sensitivity was 1fF/g. The accelerometer system was designed to provide a detection resolution of 33 milli-g over the operational range of ±100 g.

Keywords: MEMS accelerometer; capacitive sensor; commercial MEMS process; low noise sensor; wafer-level vacuum encapsulation; Teledyne DALSA MIDIS process; inertial sensor

3.1. Introduction

MEMS inertial sensors such as accelerometers and gyroscopes have become ubiquitous in our modern world [1,2]. Today, MEMS accelerometers have the second largest sales volume after pressure sensors and are used in a variety of applications including automotive, industrial,

consumer electronics, and medical devices [3]. Each of above applications uses accelerometer sensors with different operational range from milli-g to several hundred g. In particular, high g (20 g and above) accelerometers are used in aerospace and automotive applications, oil & gas exploration, and structural health monitoring [4]. In the market today, many types of accelerometers are commercially available that are based on different operational principles including piezoresistance, piezoelectricity, optical, capacitive, and frequency resonance [5].

In the current work, we describe a single axis in-plane accelerometer sensor using capacitance transduction. Capacitive accelerometers are well suited for high g applications and offer low noise and low power operation. We are the first academic research group to implement an accelerometer sensor fabricated in an unmodified commercial MEMS process called, MEMS Integrated Design for Inertial Sensors (MIDIS), offered by Teledyne DALSA Semiconductor Inc. (TDSI, Bromont, QC, Canada) [6].

Development of MEMS sensors using a commercial MEMS foundry process allows highly efficient and reproducible manufacturing at very large volume, low cost, and extremely high yield [7,8]. The use of commercial MEMS foundry process ultimately enables the developed sensors to be commercially viable and successful. Many research groups have previously developed accelerometers in an unmodified commercial process including MUMPS [7,9], SUMMiT V [10], IMEC's SiGe [11] and ThELMA [12].

Wafer level vacuum packaging of MEMS accelerometers has been demonstrated previously by several research groups [13,14]. We describe, for the first time, a MEMS accelerometer fabricated in a commercial MEMS process that itself includes wafer level vacuum encapsulation. Packaging technique and package-type currently plays one of the most important parameters for development of MEMS sensors such as accelerometers and can be a significant portion of the overall product cost [15]. Vacuum packaging is needed in the proper functioning and long term reliability of MEMS devices in avoiding stiction, controlling damping and

limiting humidity exposure. Currently, low cost wafer-level or zero-level vacuum packaging techniques, that allow the use of high volume low cost plastic packaging at the device level, have become an important topic of research and development in the MEMS industry for a variety of devices including resonant sensors and inertial sensors [15,16].

In wafer-level or zero-level packaging, there are three important parameters for consideration that includes the sealing or encapsulation material, sealing leakage rate and chip-to-chip interconnection method [17–19]. The MIDIS process provides the current state-of-the-art solutions for the above three parameters that are suitable at mass-production scale. The MIDIS process allows high vacuum encapsulation at 10 mTorr enabling very high Quality factor (Q factor) for the encapsulated devices.

The total leak rate equivalent in the MIDIS process is 45 molecules/s (7.5E−13 atm·cc/s) that is several orders of magnitude better than Military-Standard 883H (1E−9 atm·cc/s or 61,500 molecules/s) that is commonly accepted by industry [6]. Finally, the MIDIS process includes sealed vertical Through Silicon Vias (TSVs) that minimize wastage of valuable die area and allow compact flip-chip integration with microelectronic signal processing circuits.

The MIDIS process is based on high aspect ratio bulk micromachining of 30 μm thick single-crystal silicon wafer that is vacuum encapsulated between two handle silicon wafers. The proposed accelerometer design is sensitive to in-plane single axis acceleration and uses a differential capacitive measurement with asymmetric configuration capable of detection resolution of 33 milli-g over the operational range of ±100 g. The proposed accelerometer uses strong U-hinges that help to improve performance by reducing the mechanical noise. The high aspect ratio of the fabricated springs enables high precision detection along single axis and avoids cross sensitivity from other axis that could generate a systematic error in sensor output. Like other capacitive inertial sensors, the proposed accelerometer is based on the principle of a proof mass undergoing an electrostatic force over the operating frequency range that is

proportional to the input acceleration. The sensor readout circuit employed is a 24-bit 2-channel Σ-Δ capacitance-to-digital convertor (AD7746) available from Analog Devices Inc. (Norwood, MA, USA), that provides an I2C compatible output [20].

3.2. Accelerometer Sensor Structure

In this work, we present a comb-drive accelerometer that uses a proof mass, m, supported by two U-shaped springs or hinges with stiffness, k. The principle of working is based on static displacement proportional to the input acceleration over the operating frequency range. The displacement is then converted to an electrical output signal through differential capacitance transduction. Equation (3.1) gives the transmissibility function between the input acceleration, a, and the proof mass displacement, x [21]:

$$\begin{aligned} & ma = m\ddot{z} + b\dot{z} + kz \\ & \Rightarrow H(j\omega) = \frac{Z}{X} = \frac{\frac{\omega^2}{\omega_n^2}}{\sqrt{\left(1-\frac{\omega^2}{\omega_n^2}\right)^2 + \left(2\xi\frac{\omega}{\omega_n}\right)}} \\ & where \begin{Bmatrix} \xi = \frac{b}{2\sqrt{km}} \\ Z = Y - X \end{Bmatrix} \end{aligned} \tag{3.1}$$

where, ξ, b and ω_n are the damping ratio, damping coefficient, and natural angular frequency respectively.

3.2.1. Mechanical Spring Structure

The proposed accelerometer is designed for high acceleration range of ±100 g. The proof mass has a rectangular shape to allow appropriate translational motion along its in-plane direction and its thickness is set by the fabrication process which is 30μm. At low frequencies when $f << f_r$, the mechanical sensitivity, S_{mec}, is given by the Equation (3.2):

$$S_{mech} = \frac{\Delta x}{\Delta a} = \frac{1}{\omega_n^2} \tag{3.2}$$

where, $\omega_n = \sqrt{\frac{k}{m}}$ is the natural angular frequency of the vibrating system. The springs supporting the proof mass are selected as U-shape that allows a better translation motion of rigid bodies. Figure 3.1 shows the 3D model of the device without the top sealing layer. The sensor includes springs with high stiffness that helps to reduce deflection due to the temperature variations. The parameters involved in the selection of the springs are given by Equation (3.3), where E is Young's Modulus of Elasticity, h is spring beam thickness, w is spring beam width, L is spring beam length, I_z is Moment of Inertia along Z-axis:

$$K_{in-plane} = 2K_{unit} = 2\times\left(\frac{12EI_z}{L^3}\right) = 2\times\left(\frac{12w^3h}{L^3}\right) \tag{3.3}$$

In Equation (3.3), h and E are fixed by the MIDIS fabrication process. The values for L and w are optimized to obtain maximum deflection depending on the acceleration range, output linearity and the Design Rule Check (DRC) provided by TDSI for the MIDIS process. Further, all the corners are rounded in the two springs to avoid any fracture due to stress gradient and consequently to enhance the reliability of the device. The high aspect ratio of thickness to width for the springs helps to minimize disturbance from out of plane acceleration leading to low cross-axis sensitivity.

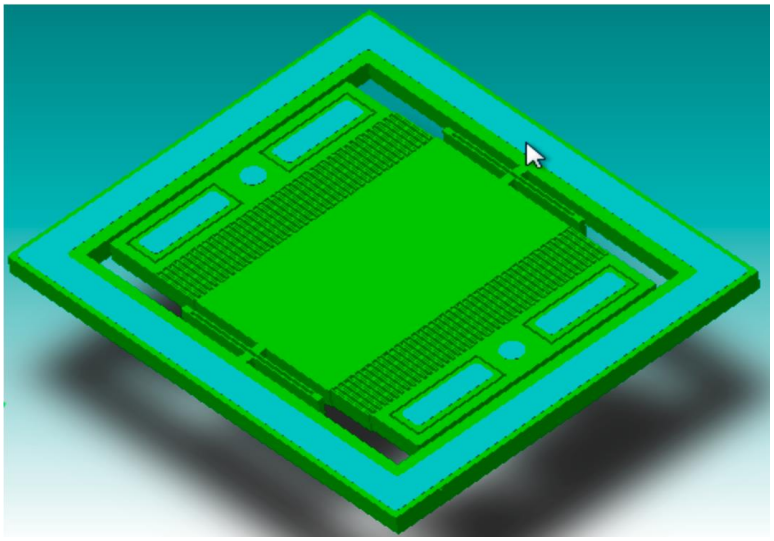

Figure 3.1 3-D Model of the single-axis capacitive accelerometer

3.2.2. Electro-Mechanical Transduction

The electrical transduction uses differential capacitance measurement through inter-digitized comb fingers with asymmetric configuration with two different gaps, g_1 and g_2. Figure 3.2 illustrates the asymmetric configuration of the transduction fingers with $g_1 > g_2$. For a small displacement, the electrical sensitivity, S_{ele} can be approximated by the Equation (3.4). In our sensor, the initial capacitance value of the sensor structure is around 1.7 pF with ΔC_{max} of 320 fF. The assumed capacitance values are affected by parasitic capacitances after physical device implementation. In our sensor, the optimal ratio between g_1 and g_2 is determined to be 6:

$$S_{ele} = \frac{\Delta C}{\Delta x} = C_0 \frac{g_2 - g_1}{g_2 g_1} \tag{3.4}$$

The overall sensitivity of the sensor is deduced from the multiplication of Equations (3) and (4) for S_{ele} and S_{mec}, respectively, and is given by Equation (3.5):

$$S_{sensor} = \frac{\Delta C}{\Delta a} = \frac{C_0 \Delta g}{\omega_n^2 g_2 g_1} \tag{3.5}$$

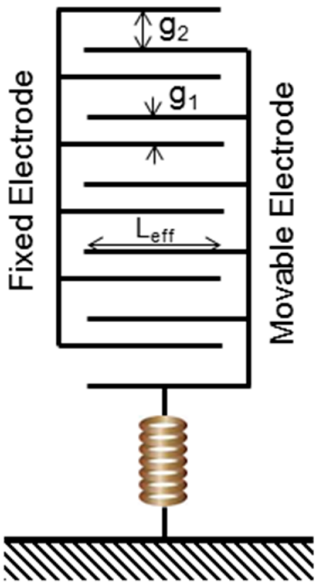

Figure 3.2 Inter-digitized comb fingers with asymmetric configuration

3.2.3. Improved Noise Performance

There are three techniques to improve the accelerometer signal to noise ratio, an, as given by Equation (3.6), where, kB, T, K_{spring} are the Boltzmann constant, operating temperature, and spring stiffness, respectively. First, the Q factor can be increased by reducing the damping factor. In the present case, this is done through the wafer level packaging under high vacuum of 10 mTorr. Second, we employed the maximum allowable gap of 30μm, between the moving structure and the capping layer in order to decrease the damping coefficient. Finally, the mechanical noise was minimized by selecting rigid springs with higher spring stiffness, K_{spring}, without drastically reducing the mechanical sensitivity [22]:

$$a_n = \sqrt{\frac{4k_B T \omega_n}{mQ}} \tag{3.6}$$

Typically, the main sources of damping effect that decrease the Q factor is due to two mechanisms, the first is related to the squeeze air film confined in the inter-digitized fingers [22] and the second concerns the slide air film between the sealing cap and the moving plate. Both these factors are negligible in the proposed sensor structure due to wafer level packaging under high vacuum of 10 mTorr.

The magnitude of electrical noise is reduced by using Σ-Δ based capacitance to digital converter (CDC) [20]. The AD7746 CDC circuit from Analog Devices offers low power consumption and low electrical noise. It uses a combination of two signal processing techniques, namely, the oversampling 24-bit Σ-Δ modulator and noise shaping filtering. Therefore, the Total Noise Equivalent Acceleration, TNEA, is given by Equation (3.7) [22]:

$$TNEA = \sqrt{a_n^2 + \left(\frac{\delta C}{S_{sensor}}\right)^2} \tag{3.7}$$

where, δC is the effective minimum capacitance detectable by the conditioning circuit per √Hz.

3.3. Simulation Results and Discussion

The simulation results are based on Finite Element Modeling (FEM) using Coventorware software for electro-mechanical, modal and damping coefficient simulations. We performed lumped modeling using Architect module where full integration of sensor and its signal conditioning circuit is implemented for time domain analysis. The modal analysis is used to show the dynamic characteristics of the accelerometer. The first mode, which illustrates the resonant frequency along the sensitive Y-axis gives the full frequency range over which the sensitivity can be considered as constant. Figure 3.3a illustrates the FEM modeling for the first mode at 12.6 kHz with an exaggerated illustration in the upper right corner. However, using lumped modeling, the frequency analysis shows the amplitude and the phase of the sensitive axis with a resonant frequency around 9.5 kHz as illustrated by Figure 3.3b. The difference in the results is mainly due to the comb fingers that add more mass to the proof plate. Also, Architect uses a model of perfect beam that gives a more accurate result than FEM method. In our sensor structure, the maximum displacement is fixed at 15% from the initial gap g1 in order to insure a good linearity.

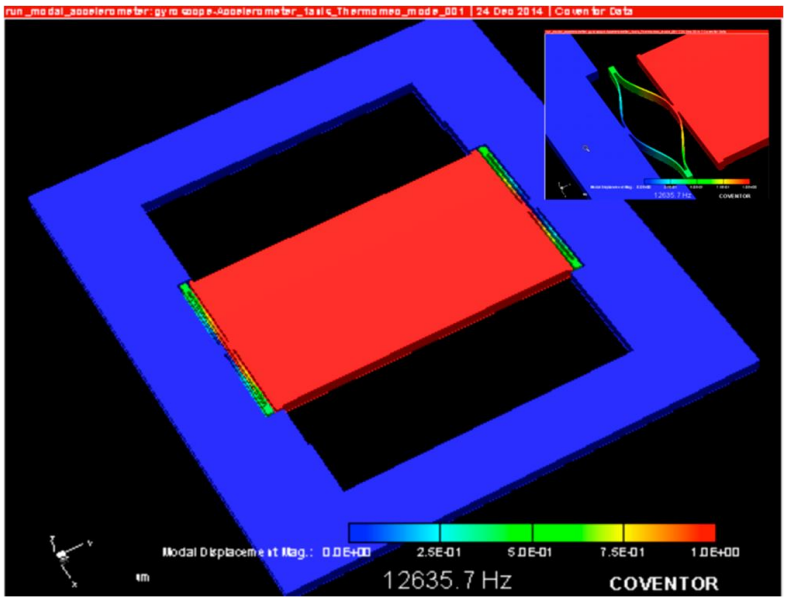

(a)

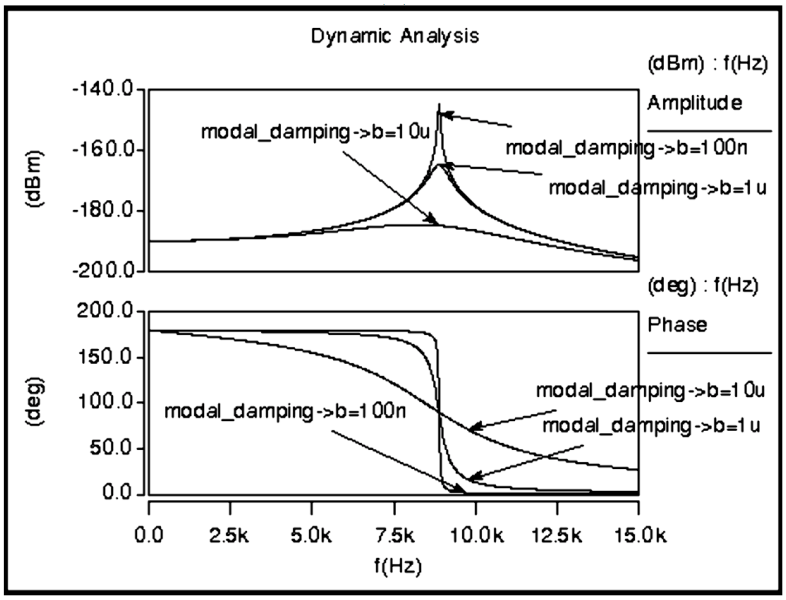

(b)

Figure 3.3 Device modeling results. (a) FEM modeling; (b) Lumped modeling

The capacitance measurement is based on differential measurement in order to double the total capacitance change and consequently improving the sensor sensitivity. The initial capacitance value for the accelerometer is selected to be 1.7 pF. Figure 3.4 shows the calibration curve of the accelerometer sensor for both polarities of the differential capacitance.

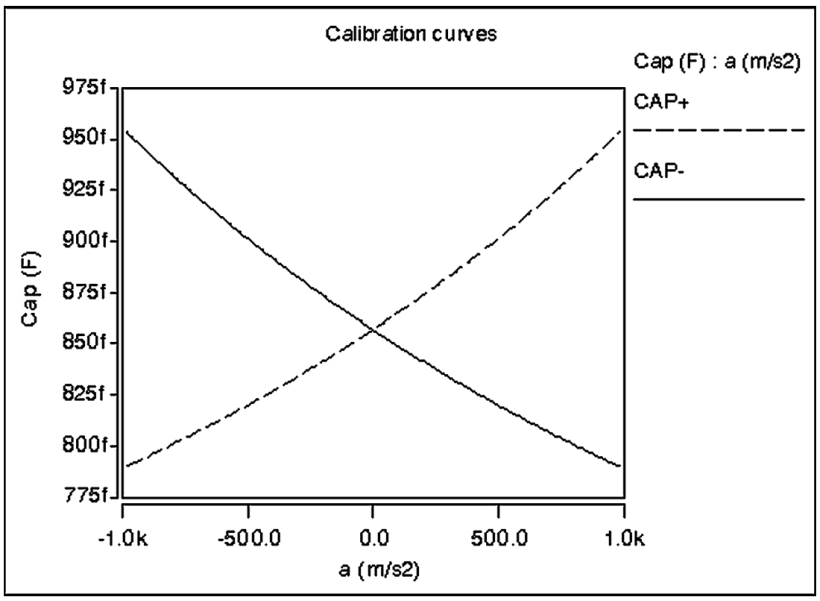

Figure 3.4 Electro-mechanical analysis showing the calibration curve response

We aim to deduce the damping force coefficient in condition of high vacuum. Here, two simulations were performed for the slide film effect and stokes fluid effect. Figure 3.5 illustrates the variation of the damping force coefficient in terms of operating frequency. At resonance frequency, the value of the damping force coefficient is around 1.17×10^{-8} (N/m/s). The damping coefficient in stokes flow reaches 3.42×10^{-7} (μN/μm/s), which means that the effect of inter-digitized fingers on damping is more significant than the slide flow mechanism.

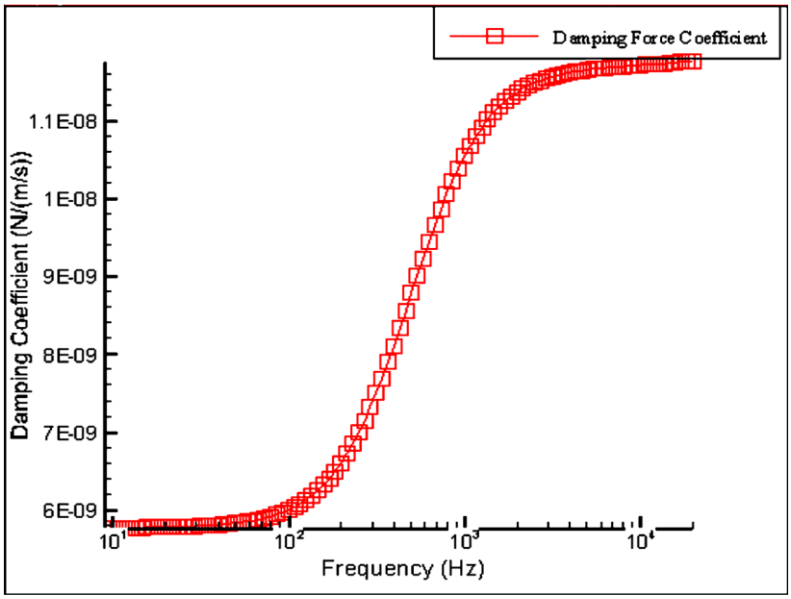

Figure 3.5 Simulation of damping force coefficient over the operational frequency range

3.4. Experimental Results and Discussion

The accelerometer device is fabricated using MIDIS process available from TDSI [5]. The Scanning Electron Microscope (SEM) image of the fabricated accelerometer is shown in Figure 3.6a that shows the proof mass suspended by U-shaped mechanical springs. Figure 3.6b shows the SEM image of spring structure with its rounded corners and Figure 3.6c shows the close-up view of the comb-drive electrodes. Table 3-1 shows the chosen specifications for the accelerometer device. The experimental measurements aim to deduce the sensor sensitivity and the associated resolution which is affected by the measured total noise. Here, the sensor data is recorded by the 24-bit 2-channel Σ-Δ capacitance-to-digital convertor (AD7746) available from

Analog Devices Inc. that is maintained at room temperature (23 °C). The Σ-Δ modulator helps to significantly minimize the noise and therefore helps to enhance the measurement accuracy.

Table 3-1 Accelerometer specifications

Parameter	In-Plane Metrics
Mechanical Sensitivity	2.83×10^{-8} (m/m/s^2)
Sensor Sensitivity	1.6 fF/g
Resolution	33 mg
Resonance frequency	9.45 (kHz)
Mechanical Acceleration Noise	2.23×10^{-2} (μg·√Hz)
Dimensions	350 × 600 × 30 (μm^3)

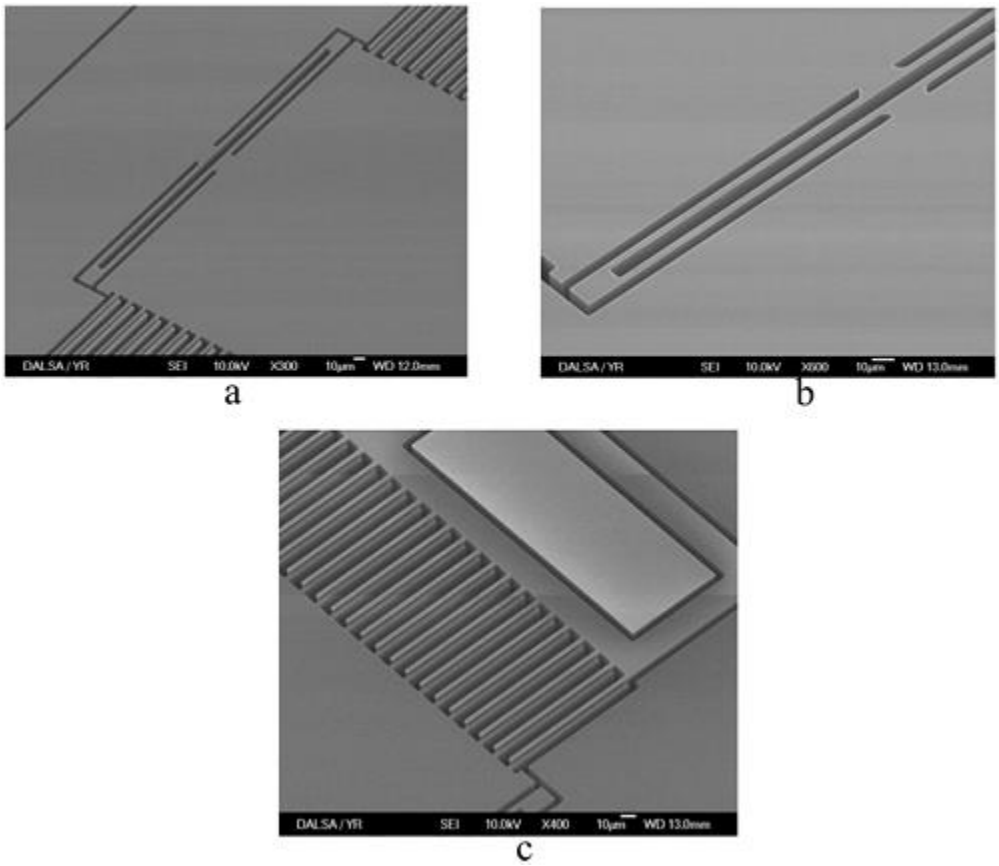

Figure 3.6 SEM images of the fabricated accelerometer device. (a) Accelerometer sensor; (b) U-shaped springs; (c) Inter-digitized sensing electrodes

The measurements consist of manually tilting the chip by 180° repeatedly over 10 times to change the acceleration due to gravity from +1 g to −1 g as shown in Figure 3.7a. Over the ±1 g measurement range, the sensitivity was measured as 1 fF/g from Figure 3.7b, which is close to 1.6 fF/g as noted from simulation results and the experiment was repeated over two cycles. The maximum noise measured corresponds to the minimum detectable signal and consequently determines the resolution of the sensor. This parameter is extracted by dividing the full range by 6σ as shown in Figure 3.7c, which leads to a resolution of 33 milli-g.

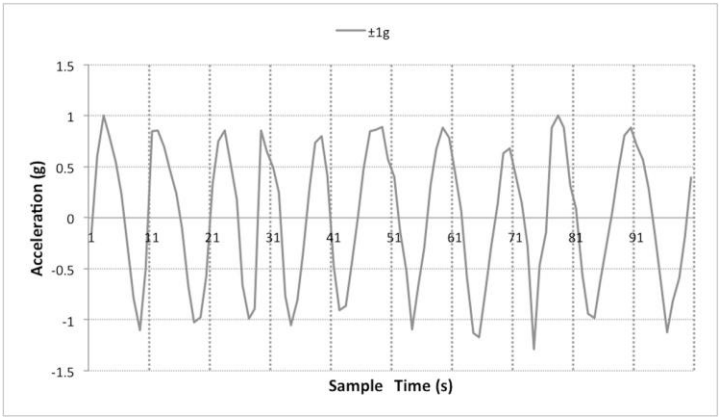

(a)

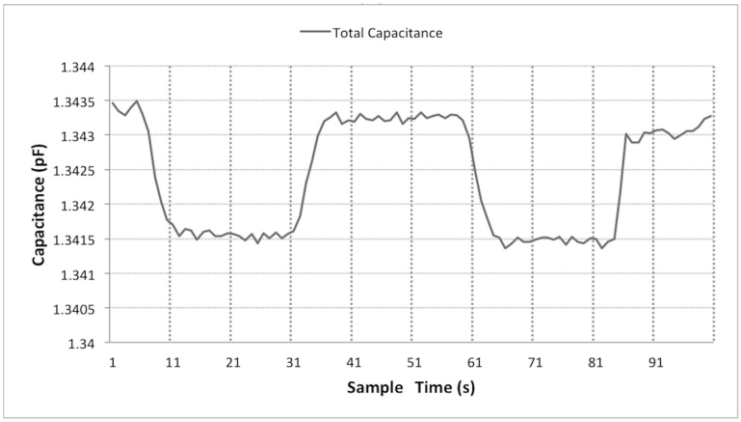

(b)

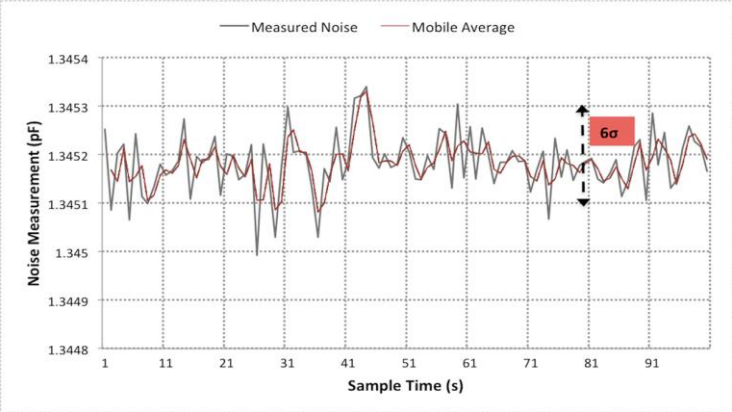

(c)

Figure 3.7 Experimental measurement results. (a) Response from ±1 g acceleration; (b) Capacitance measurement over ±1 g; (c) Generated noise from sensor system

3.5. Conclusions

We report, for the first time, the design and fabrication of a MEMS accelerometer sensor in an unmodified commercial MEMS process that includes wafer-level vacuum encapsulated. Specifically, the accelerometer sensor was fabricated in MIDIS process recently introduced by Teledyne DALSA Semiconductor Inc. The proposed accelerometer design is sensitive to in plane single axis acceleration and uses a differential capacitive measurement. Our approach allows highly efficient and reproducible manufacturing at very large volume, low cost, and extremely high yield. Over ±1 g measurement range, the measured sensitivity was 1 fF/g. The accelerometer system was designed to provide a detection resolution of 33 milli-g over the operational range of ±100 g.

Acknowledgments

We would like to acknowledge the financial support given by Natural Sciences and Engineering Research Council of Canada (NSERC). We would like to acknowledge the access to MIDIS

fabrication process of Teledyne DALSA Semiconductor Inc. provided by Canada Microelectronics Corporation (CMC). The devices were tested at CMC facility.

Author Contributions

A.M. conducted the research presented in the article. P.Y. contributed towards experimental evaluation and testing. Y.W. and V.P.C. contributed towards writing of the article.

Conflicts of Interest

The authors declare no conflict of interest.

References

1. S. D. Senturia, "Introduction," in *Microsystem Design*, ed Boston, MA: Springer US, 2001, pp. 3-14.

2. N. Yazdi, F. Ayazi, and K. Najafi, "Micromachined inertial sensors," *Proceedings of the IEEE*, vol. 86, pp. 1640-1659, 1998.

3. Choudhary, V.; Iniewski, K. *MEMS Fundamental Technology and Applications*; Iniewski, K., Ed.; CRC Press: Boca Raton, FL, USA, 2013.

4. Kraft, M.; White, N.M. *MEMS for Automotive and Aerospace Applications*; Woodhead Publishing: Sawston, Cambridge, UK, 2013.

5. R. Bogue, "Recent developments in MEMS sensors: a review of applications, markets and technologies," *Sensor Review*, vol. 33, pp. 300-304, 2013.

6. MEMS Integrated Design for Inertial Sensors (MIDIS). Available online: http://www.teledynedalsa. Com/semi/mems/applications/midis/ (accessed on 23 January 2015).

7. Farahani, H.; Mills, J.K.; Cleghorn, W.L. Design, fabrication and analysis of micromachined high sensitivity and 0% cross-axis sensitivity capacitive accelerometers. *Microsyst. Technol.* **2009**, *15*,1815–1826.

8. Bahreyni, B.; Najafi, F.; Shafai, C. Piezoresistive sensing with twin-beam structures in standard MEMS foundry processes. *Sens. Actuators A Phys.* **2006**, *127*, 325–331.

9. Qu, P.; Qu, H.W. Design and Characterization of a Fully Differential MEMS Accelerometer Fabricated Using MetalMUMPs Technology. *Sensors* **2013**, *13*, 5720–5736.

10. Serrano-Vazquez, F.; Herrera-May, A. Bandala-Sanchez M. Design and modeling of a single-mass biaxial capacitive accelerometer based on the SUMMiT V process. *Microsyst Technol.* **2013**, *19*, 1997–2009.

11. Witvrouw, A.; van Hoof, R.; Bryce, G.; Du Bois, B.; Verbist, A.; Severi, S.; Haspeslagh, L.; Osman, H.; de Coster, J.; Wen, L.; *et al.* SiGe MEMS Technology: A Platform Technology Enabling Different Demonstrators. *ECS Trans.* **2010**, *33*, 799–812.

12. Comi, C.; Corigliano, A.; Ghisi, A.; Zerbini, S. A resonant micro accelerometer based on electrostatic stiffness variation. *Meccanica* **2013**, *48*, 1893–900.

13. Jeong, Y.; Serrano, D.E.; Keesara, V.; Sung, W.K.; Ayazi, F. Wafer-Level Vacuum-Packaged Tri-Axial Accelerometer with Nano Airgaps. In Proceedings of the 26th IEEE International Conference on Micro Electro Mechanical Systems, Taipei, Taiwan, 20–24 January 2013; pp. 33–36.

14. Premachandran, C.S.; Chong, S.C.; Liw, S.; Nagarajan, R. Fabrication and Testing of a Wafer-Level Vacuum Package for MEMS Device. *IEEE Trans. Adv. Packag*. **2009**, *32*, 486–490.

15. Liu, P.S.; Wang, J.L.; Tong, L.Y.; Tao, Y.J. Advances in the Fabrication Processes and Applications of Wafer Level Packaging. *J. Electron. Packag.* **2014**, *136*, doi:10.1115/1.4027397.

16. Chae, J.; Giachino, J.M.; Najafi, K. Fabrication and characterization of a wafer-level MEMS vacuum package with vertical feedthroughs. *J. Microelectromech. Syst.* **2008**, *17*, 193–200.

17. Esashi, M. Wafer level packaging of MEMS. *J. Micromech. Microeng.* **2008**, *18*, doi:10.1088/0960-1317/18/7/073001

18. Zhang, K.; Jiang, W.; Li, X.X. Wafer-level sandwiched packaging for high-yield fabrication of high-performance MEMS inertial sensors. In Proceedings of the IEEE 21st International Conference on Micro Electro Mechanical Systems, Tucson, AZ, USA, 13–17 January 2008; pp. 814–817.

19. Zoschke, K.; Manier, C.A.; Wilke, M.; Jurgensen, N.; Oppermann, H.; Ruffieux, D.; Dekker, J.; Heikkinen, H.; Dalla Piazza, S.; Allegato, G.; *et al*. Hermetic Wafer Level Packaging of MEMS Components Using Through Silicon via and Wafer to Wafer Bonding Technologies. In Proceedings of the 2013 IEEE 63rd Electronic Components and Technology Conference (Ectc), Las Vegas, NV, USA, 28–31 May 2013; pp. 1500–1507.

20. Analog Devices Inc. Available online: http://www.analog.com/en/analog-to-digital-converters/ capacitance-to-digital converters/ad7746/products/product.html (accessed on 23 January 2015).

21. Krishnan, G.; Kshirsagar, C.U.; Ananthasuresh, G.K.; Bhat, N. Micromachined High-Resolution Accelerometers. *J. Indian Inst. Sci.* **2007**, *87*, 333–361.

22. Amini, B.V.; Ayazi, F. Micro-gravity capacitive silicon-on-insulator accelerometers. *J. Micromech. Microeng.* **2005**, *15*, 2113–2120.

CHAPTER -4

4. Wafer level vacuum encapsulated tri-axial Accelerometer with low cross-axis sensitivity in a commercial MEMS Process

We present the design, fabrication and testing of a novel integrated tri-axial capacitive accelerometer with low cross-axis sensitivity. The accelerometer is fabricated in MEMS Integrated Design for Inertial Sensors (MIDIS), a process recently introduced by Teledyne DALSA Semiconductor Inc. (TDSI). The MIDIS process is based on high aspect ratio bulk micromachining of single-crystal silicon wafer that is vacuum encapsulated between two other silicon wafers. The fabrication process includes Through Silicon Vias (TSVs) with sealed anchors for compact flip–chip integration with microelectronic signal processing circuitry. The proposed accelerometer is designed to provide simultaneous detection of the input accelerations along the 3 principle axes enabling high-g measurement up to ±50 g. The integrated structure design uses decoupled frames supported by strategically designed springs and employs capacitive compensators for the purpose of achieving low cross-axis sensitivity. The capacitive transduction is based on differential measurement along X- and Y- axis and absolute measurement along the Z-axis. The initial measured capacitances are 2.18 pF, 2.4 pF and 1.14 pF along X, Y and Z-axis, respectively. The dynamic specifications of the accelerometer are characterized by its lowest-order operating mode at 4 kHz.

4.1. Introduction

The market potential for silicon-based low cost, miniaturized and low power multi-axis Micro-Electro-Mechanical System(MEMS) accelerometers is growing rapidly and these sensors are

found in a variety of devices and applications including smartphones, gaming devices, digital cameras, automobiles, wear-able devices, structural health monitoring, energy exploration and industrial manufacturing [1–3]. Many leading and emerging semiconductor companies are currently marketing silicon based tri-axial accelerometers including Analog Devices [4], ST Microelectronics [5], Freescale Semiconductor [6], Invensense [7] and BOSCHSensortec [8]. Further, the development of silicon based tri-axial accelerometers has been extensively studied by several research groups using various custom or proprietary microfabrication processes with surface micromachining [9], bulk micromachining [10], combined surface and bulk micromachining [11], and CMOS-MEMS process [12,13].The current work describes, for the first time, the design and fabrication of a wafer level vacuum encapsulated tri-axial accelerometer with low cross-axis sensitivity using an unmodified commercial MEMS process. The capacitive accelerometer is fabricated using MEMS Integrated Design for Inertial Sensors (MIDIS) process, offered by Teledyne DALSA Semiconductor Inc. (TDSI) [14]. The proposed approach provides a promising option allowing highly efficient and reproducible manufacturing at large volumes, lower cost, and high yields. Silicon-based capacitive accelerometers are relatively simple to fabricate, low cost, small size, low power, and low noise and provide high sensitivity, good DC response, low drift, and low temperature sensitivity [15]. Tri-axial accelerometers, as proposed in the current work, require very low cross-axis sensitivity across the three directions. Here, cross-axis sensitivity is defined as the output induced on a sense axis from the application of acceleration on a perpendicular axis, expressed as a percentage of the sensitivity, and which presents a major source of systematic error in the measurement [15]. Previous implementations of accelerometers with low or nearly zero% cross-axis sensitivity include Farahaniet al. [16] who demonstrated single axis capacitive accelerometer using a commercial MEMS process, Li et al. [17] who demonstrated tri-axial capacitive accelerometer using a custom microfabrication process, and our group [18] has described the design of anon-

encapsulated tri-axial capacitive accelerometer with decoupled frames using a commercial SOIMUMPS MEMS process from MEMSCAP. To date, there have been many previous implementations of accelerometers in an unmodified commercial MEMS process including MUMPS [19, 20], SUMMiT V, [21], IMEC's SiGe [22] and ThELMA [23]. However, the MIDIS process offered by TDSI is currently the only commercial MEMS process that includes ultra-clean wafer level vacuum encapsulation of the MEMS devices. Wafer level vacuum encapsulation of MEMS devices is currently extensively studied by various research groups as it plays a key role in improving the sensor performance and long term reliability [24–26]. The availability of wafer level vacuum encapsulation in MIDIS process provides extraordinary benefit in comparison to the existing state-of-the-art microfabrication processes for the development of MEMS sensors in reducing the overall product cost, simplifying packaging constraints, and easing supply-chain logistics. The encapsulation of vibrational inertial MEMS sensors such as accelerometers with a pressure below atmospheric pressure influences quality factor, response time, stiction, damping and humidity exposure [27]. While wafer level vacuum packaging of MEMS accelerometers has been demonstrated previously by several other research groups [28,29] using custom microfabrication process, but here we employ wafer level vacuum packaging of MEMS accelerometers in a high volume commercial MEMS process. Previously, our group described a wafer level vacuum encapsulated single-axis capacitive accelerometer sensor using MIDIS process [30].The MIDIS process from TDSI is based on high aspect ratio bulk micromachining of single-crystal silicon wafer (device layer) that can either be vacuum encapsulated at 10 mTorr or at sub-atmospheric pressure of 150 mTorr between two other silicon wafers (top interconnect and bottom handle wafers). The total leak rate equivalent in the MIDIS process is 45 molecules/s ($7.5 \times 10{-}13$atm cm3/s). The top silicon wafer includes Through Silicon Vias (TSVs) with sealed anchors for compact flip–chip integration and interconnection with external microelectronic signal processing circuitry [14].

In this paper, we describe a tri-axial accelerometer sensor permitting simultaneous acceleration detection along the 3 principal axes (X, Y and Z). There are two important novelties in the current work, first, we achieve a low cross sensitivity using a strategic design of decoupled frames. Second, the MIDIS process is specifically optimized for in-plane inertial sensor development, and thus, development of tri-axial inertial sensors with out-of-plane measurement is a novel contribution in the cur-rent work. The MIDIS process allows recessed comb-fingers that are used to enable sensing along Z-direction in the current work. In summary, we propose a mechanism that employs a differential capacitive transduction using asymmetric configuration for in-plane measurement along X- and Y- axis and an absolute measurement along Z-axis. The proposed sensor uses different kinds of spring structures that are made selectively more sensitive a cross one specific axis of input acceleration. The accelerometer sensor is interfaced to a capacitance to digital converter circuit from Analog Devices Inc. (Model AD7746). The AD7746 provides good performance in terms of low noise and direct I2C interface to a microcontroller. In Section 2, we present an overview of the new accelerometer design and followed by simulation results in Section 3. Section 4 describes the fabrication and experimental results, and finally, we conclude the paper.

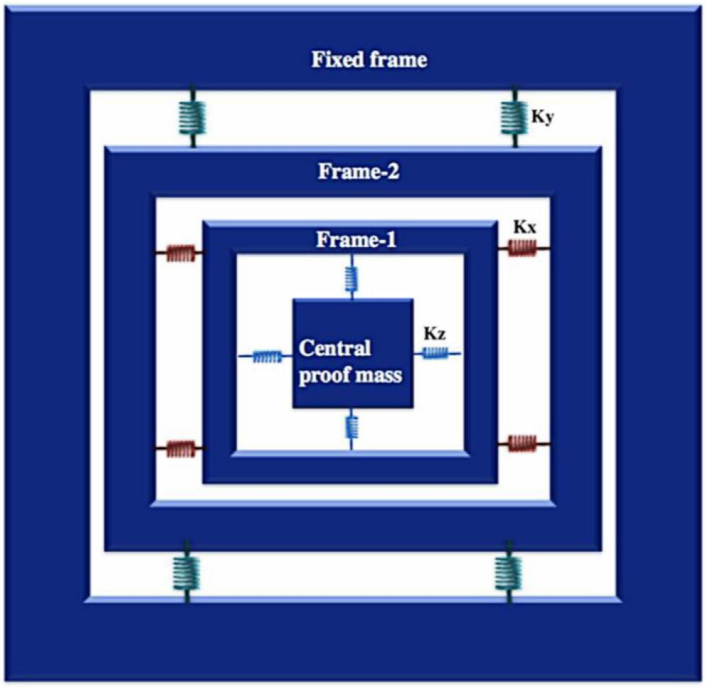

Figure 4.1Structural design of the tri-axial accelerometer sensor with decoupled frames

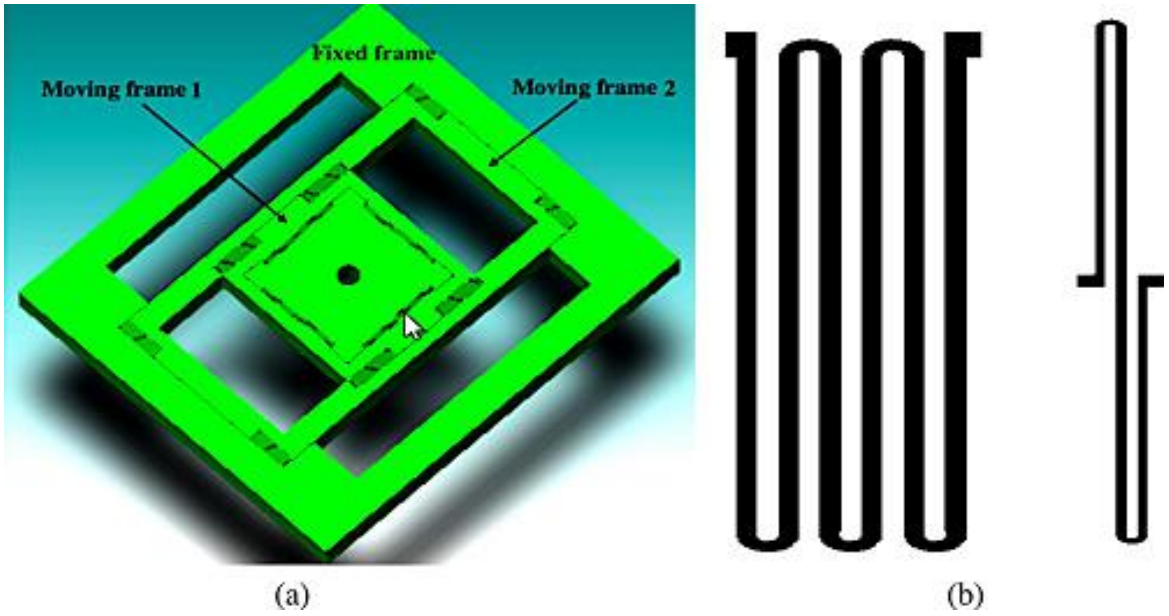

Figure 4.2 (a) 3-D model of the accelerometer sensor with showing only the fixed and decoupled frame structures. (b) Shapes of the spring structures employed in accelerometer sensor

4.2. Accelerometer sensor design

Fig.1 shows the design of the proposed tri-axial accelerometer. The design consists of a central proof mass supported by multiple frames that are connected to each other by different kinds of spring structures. The accelerometer uses one single central proof mass structure moving along the main principle axes that helps towards reducing the total dimensional area of the inertial sensor. The central proof mass, the Frame-1 and Frame-2 are sensitive to Z-, X- and Y- axis directions, respectively. Thus, each axis can be modeled by a spring-mass system with its associated damping coefficients, b_x, b_y, and b_z, along X-, Y- and Z- axis, respectively, as given by Eq. (4.1) [31, 32]. Each mass component, m_x, m_y, and m_z experiences a stimulus force due to the applied accelerations, a_x, a_y, and a_z, along X-,Y- and Z- axis, respectively, generating a small dis-placement that is converted into electrical measurement through two mechanisms, differential capacitance measurement along X-and Y-axis and absolute capacitance measurement along Z-axis. The transmissibility function, T (jω), between the acceleration and the displacement is expressed by Eq. (4.2), where, ω_0 is the natural frequency and ξ is the damping ratio.

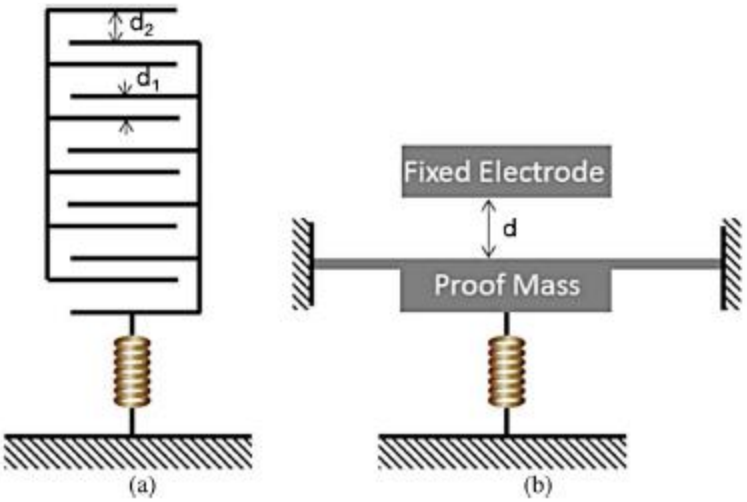

Figure 4.3 Mechanisms of signal transduction. (a) Differential capacitance measurement with asymmetric comb-finger configuration along X- and Y- axis. (b) Absolute capacitance measurement along Z-axis

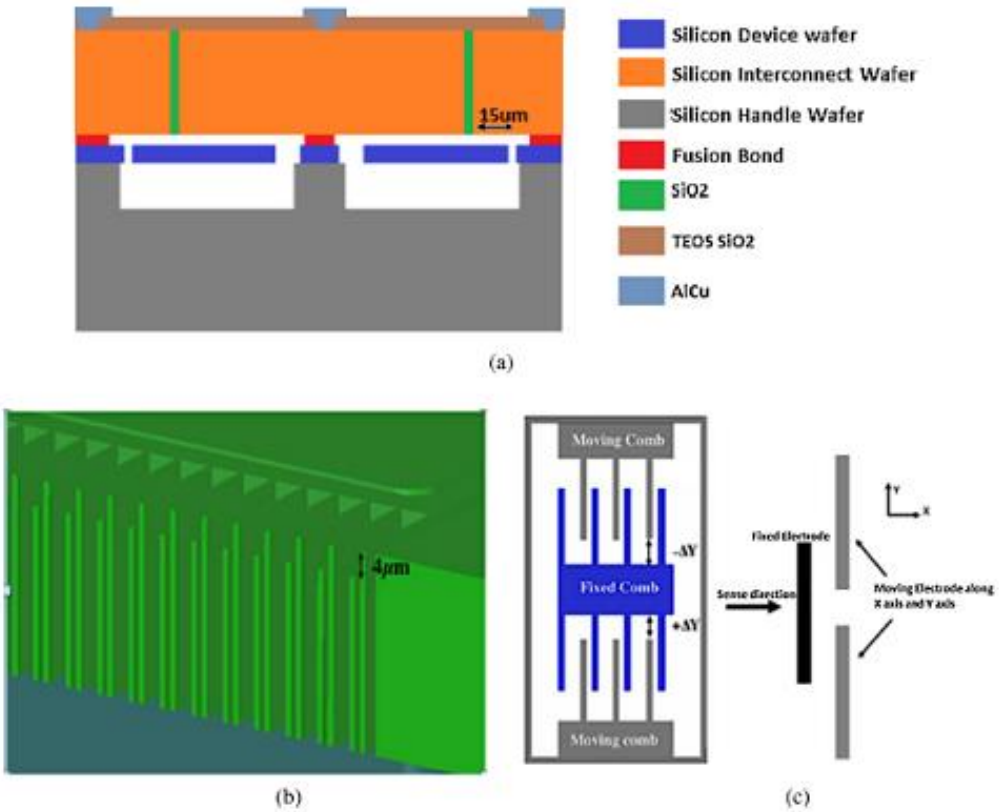

Figure 4.4 Cross-axis sensitivity minimization techniques in addition to decoupled frames. (a) The extended area of the top electrode along X- and Y- axis. (b) Recessed fingers with 4 μm height difference. (c) Capacitive inter-digitized compensation electrodes

$$\begin{pmatrix} m_x & 0 & 0 \\ 0 & m_y & 0 \\ 0 & 0 & m_z \end{pmatrix}\begin{pmatrix} \ddot{x} \\ \ddot{y} \\ \ddot{z} \end{pmatrix}+\begin{pmatrix} b_x & 0 & 0 \\ 0 & b_y & 0 \\ 0 & 0 & b_z \end{pmatrix}\begin{pmatrix} \dot{x} \\ \dot{y} \\ \dot{z} \end{pmatrix}+\begin{pmatrix} k_x & 0 & 0 \\ 0 & k_y & 0 \\ 0 & 0 & k_z \end{pmatrix}\begin{pmatrix} x \\ y \\ z \end{pmatrix}=\begin{pmatrix} m_x a_x \\ m_y a_y \\ m_z a_z \end{pmatrix} \tag{4.1}$$

$$T(j\omega)=\frac{\frac{1}{\omega_0^2}}{\sqrt{\left(1-\frac{\omega^2}{\omega_0^2}\right)^2+\left(2\varsigma\frac{\omega}{\omega_0}\right)^2}} \tag{4.2}$$

4.2.1. Electro-mechanical design

Fig. 4.2(a) shows the 3-D model of the accelerometer device structure. Fig. 4.2(b) shows the shapes of the spring structures that are used to support the three different masses. The central proof mass has a square shape to allow uniform out-of-plane motion sensing. The frames have

a rectangular shape enabling more sensitive in-plane motion sensing along specific axis. The device thickness is fixed by the MIDIS fabrication process at 30 μm. The large size of the proof masses helps to reduce the noise and increase the sensitivity of the accelerometer. At low operational frequencies (when, $f<<f_0$), the mechanical sensitivity, S_{mech}, is inversely proportional to the natural frequency, f_0, for each axis and is given by the Eq. (4.3), where, Δx is the displacement for a specific variation of the input acceleration, Δa.

$$S_{mech} = \frac{\Delta x}{\Delta a} = \frac{1}{\left(2\pi f_0\right)^2} \tag{4.3}$$

The springs supporting the proof mass and moveable frame structures consist of four flexible serpentine shaped springs supporting the central proof mass and four springs supporting each frame. Each spring is composed of 3 units of U-shape springs connected in series for Frames 1 and 2. All the corners are filleted to reduce the stresses due to elevated processing temperatures, especially, during the bonding process. Based on the lumped modeling, the spring constants, K_x and K_y along X- and Y- axes, respectively and K_z along Z axis can be expressed by Eq. (4.4) [33], where E, I, h, w and L represent the young's modulus, inertial moment, height, width and length for each beam, respectively. The aspect ratio of thickness to width is appropriately designed to insure high stiffness allowing only one movement along the intended specific axis.

$$\begin{aligned} K_{x/y} &= \frac{8EI_z}{L^3} = \frac{2Ehw^3}{3L^3} \\ K_z &= \frac{24EI_y}{5L^3} = \frac{2Eh^3w}{5L^3} \end{aligned} \tag{4.4}$$

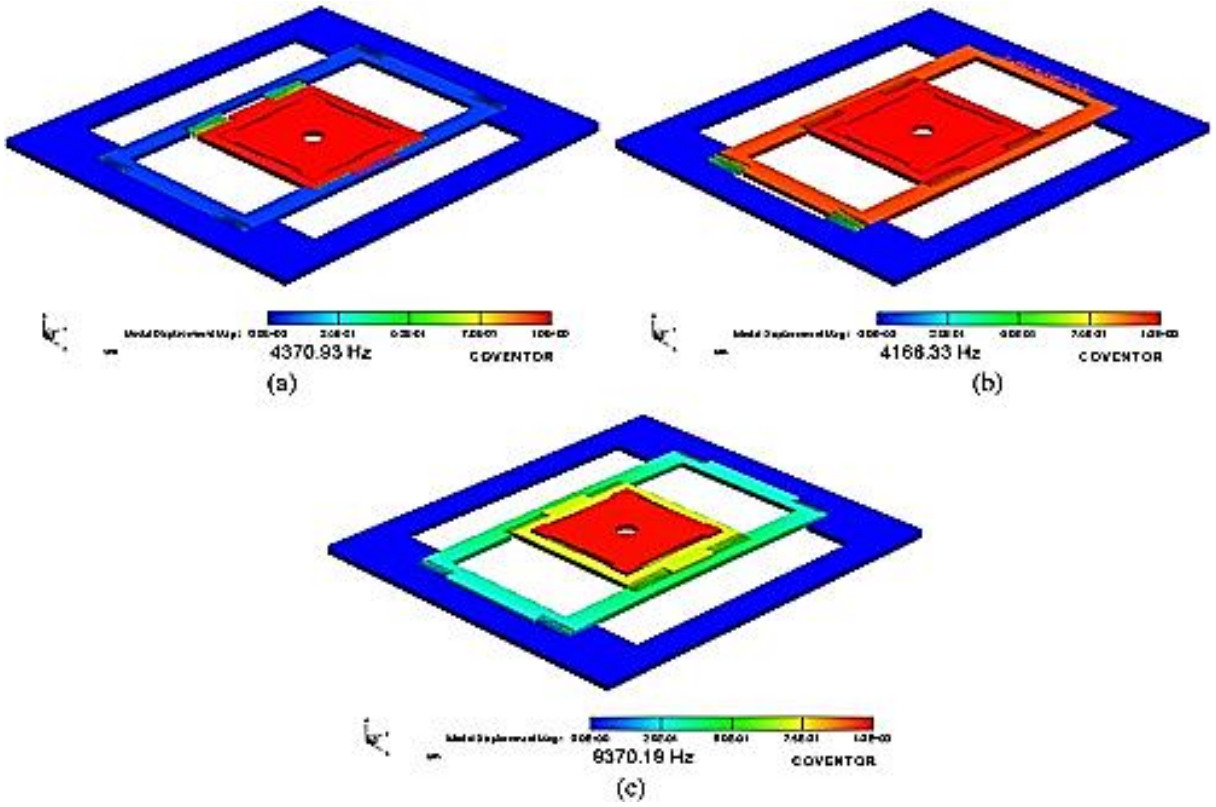

Figure 4.5 Finite Element Method (FEM) analysis. (a) In-plane mode along X- axis. (b) In-plane mode along Y- axis. (c) Out of plane mode along Z-axis

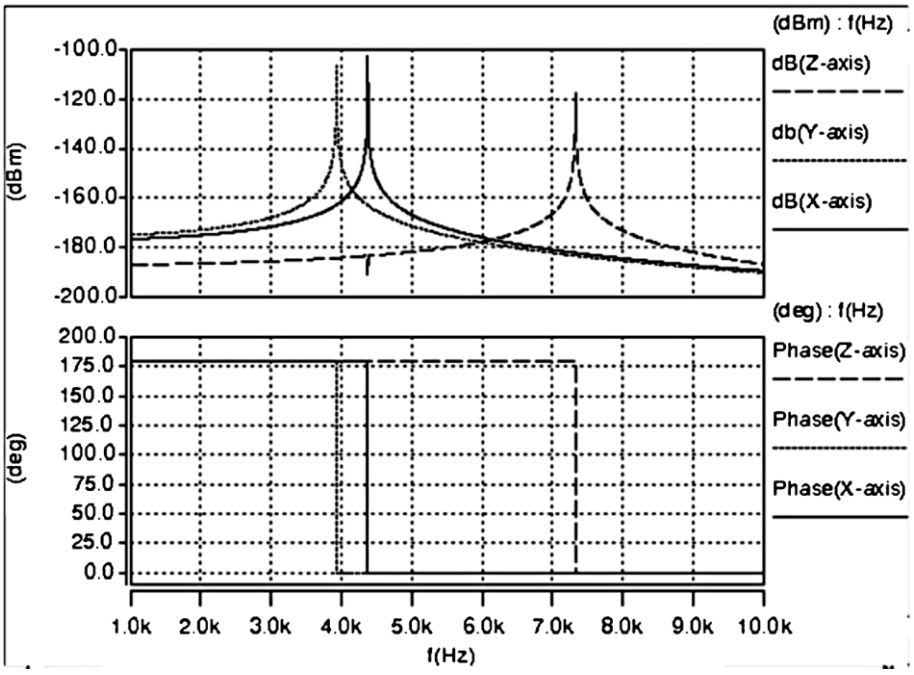

Figure 4.6 Frequency-Domain Analysis: Lumped modeling

From Fig. 4.3, the electrical transduction uses differential capacitance measurement with asymmetric configuration through inter-digitized fingers with two different gaps (d_1 and d_2) along X- and Y- axis. However, the transduction is based on absolute measurement along Z-axis with a gap, d, between the two electrodes. For a small displacement, the electrical sensitivities along all directions are expressed by Eq. (4.5). Here, the small gap, d1, between the inter-digitized fingers is fixed at 2 µm and the optimal ratio between d1 and d2 is determined to be 6. The gap, d, between the top electrode and the central proof mass is set at 2 µm. The overall sensitivity of the sensor is given by Eq. (4.6).

$$S_{x/y\_elect} = C_0 \frac{d_2 - d_1}{d_2 d_1}$$
$$S_{z\_elect} = \frac{C_0}{d} \tag{4.5}$$

$$S_{x/y\_elect} = \frac{C_0}{\omega_0^2} \frac{d_2 - d_1}{d_2 d_1}$$
$$S_z = \frac{C_0}{\omega_0^2 d} \tag{4.6}$$

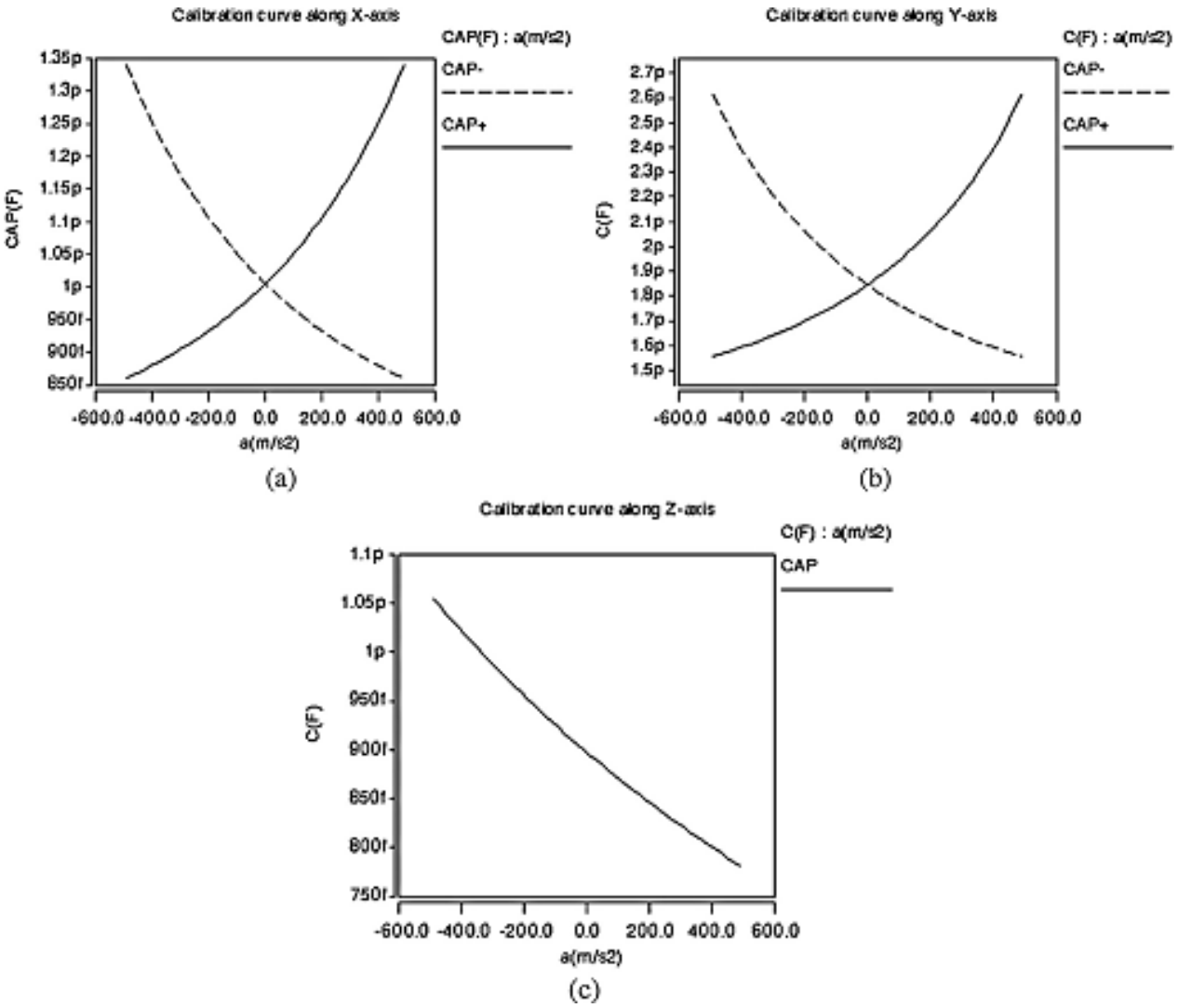

Figure 4.7 Simulated calibration curves. (a) Differential measurement along X-axis. (b) Differential measurement along Y-axis. (c) Absolute measurement along Z-axis

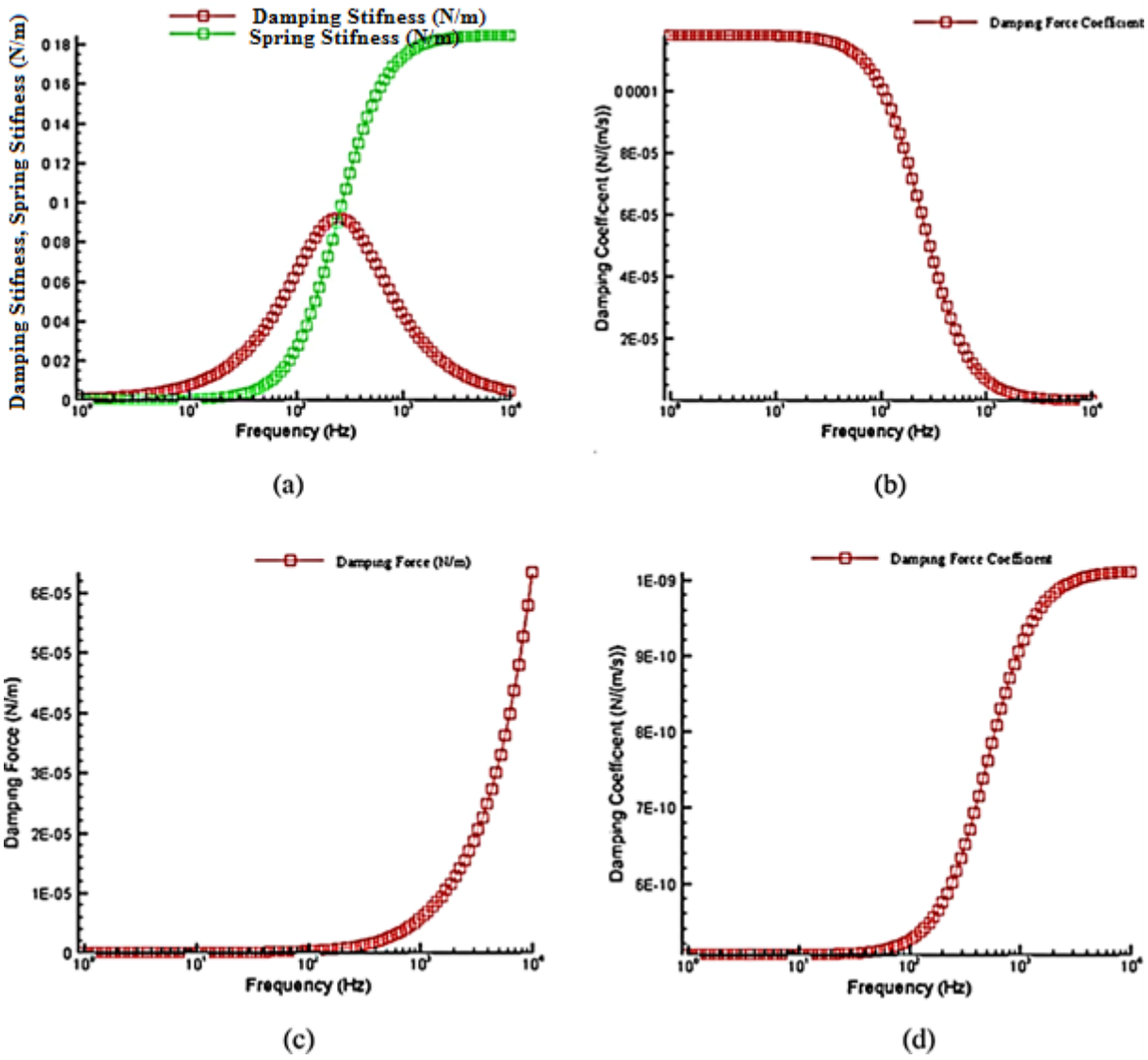

Figure 4.8 Damping results for the central proof mass. (a) Damping force due to squeezed effect. (b) Damping coefficient due Squeezed effect. (c) Damping force due to slide effect. (d) Damping force coefficient due to slide air-film effect

4.2.2. Cross-axis sensitivity

The output signal of the tri-axial accelerometer that uses a single proof-mass structure and performs simultaneous measurement across the three principle axes, can generally be expressed by Eq. (4.7) [16–34]. Ideally, to achieve zero% cross-axis sensitivity, the matrix shown in Eq. (4.7) should only have terms S_{xx}, S_{yy} and S_{zz}, with rest being equal to zero. Thus, the cross-axis sensitivity which is defined as the output induced on a sense axis from the application of

acceleration on a perpendicular axis, expressed as a percentage of the sensitivity is given by Eq. (4.8) [35].

$$\begin{pmatrix} S_{xx} & S_{xy} & S_{xz} \\ S_{yx} & S_{yy} & S_{yz} \\ S_{zx} & S_{zx} & S_{zz} \end{pmatrix} \begin{pmatrix} a_x \\ a_y \\ a_z \end{pmatrix} = \begin{pmatrix} V_x \\ V_y \\ V_z \end{pmatrix} \tag{4.7}$$

$$\begin{aligned} Cross\_sensitivity(\%) &= \left(\frac{\sqrt{\left(S_{xy} - S_y\right)^2 + \left(S_{zy} - S_y\right)^2}}{S_y} \right) \times 100(\text{for y axis}) \\ &= \left(\frac{\sqrt{\left(S_{yx} - S_x\right)^2 + \left(S_{zx} - S_x\right)^2}}{S_y} \right) \times 100(\text{for x axis}) \\ &= \left(\frac{\sqrt{\left(S_{xz} - S_z\right)^2 + \left(S_{yz} - S_z\right)^2}}{S_z} \right) \times 100(\text{for z axis}) \end{aligned} \tag{4.8}$$

The capability to displace the central proof mass along Z-axis is achieved by the four serpentine springs where the stiffness is predominant over the U-shape springs as shown by Figs. 1 and 2.

This allows dominant and unidirectional displacement of the bot-tom electrode. The area in the top wafer with TSVs exceeds the central proof mass dimensions by 15 μm as shown in Fig. 4.4(a), which is considered sufficient margin to enable the bottom electrode to move along X- or Y-axis without causing any DC offset in the electrical measurement that could lead to cross-axis sensitivity. Further, there is no effect of the vertical displacement from the inter-digitized fingers as the difference in the height between the fixed and the moving fingers is 4 μm, leading to null DC offset and thus leads to low cross-axis sensitivity as shown in Fig. 4.4(b). The cross-axis sensitivity issue along X- and Y-axis is addressed through the use of two moving frames which permit to decouple the motion along the X- and Y-axis. As shown in Fig. 4.2(b), the Frame-1 is supported by Frame-2, thus, there is negligible effect of the X-axis acceleration on the Frame-2. However, any movement in the Y-axis direction has direct effect on the Frame-1.

This issue was resolved by employing another inter-digitized compensation capacitor, as shown in Fig. 4.4(c), which keeps the same initial capacitance value regardless of the motion of the Frame-1 along Y-axis. Thus, there is no mutual effect from the two frames on the output capacitance measurement which ultimately leads to low cross-axis sensitivity between a_x and a_y.

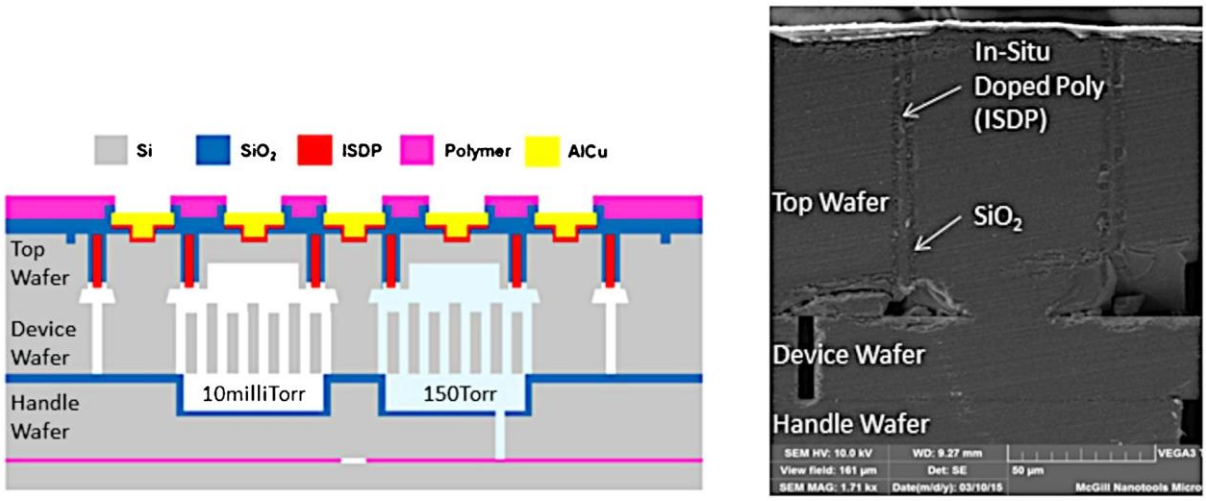

Figure 4.9 (a) Cross sectional view of the layers involved in the inertial sensor fabrication [14]. (b) Cross sectional microscope image of the tri-axial accelerometer

4.3. Simulation results and discussion

The simulations consist of modal and damping analysis using Finite Element Method (FEM) analysis using Coventorware software. Architect module was used to perform lumped modeling where one could perform co-integration analysis combining signal conditioning circuitry and the sensor device.

4.3.1. Electromechanical results

The modal analysis is used to show the dynamic characteristics of the sensor. The shapes for the first, second and third mode are illustrated in Fig. 4.5. The resonant frequencies along sensitive X-, Y-and Z-axis are designed as 4.37 kHz, 4.16 kHz and 8.37 kHz, respectively. Lumped modeling (using Architect software module) uses frequency analysis to show the

amplitude and the phase of the sensitive axis with a resonant frequencies around 4 kHz, 4.3 kHz and 7.3 kHz along X-, Y- and Z-axis, respectively, as illustrated by Fig. 4.6. Note that, the FEM method takes into account the rounded shapes of the springs as well as the complete structure shape. However, lumped modeling uses a perfect model for beams and structures which introduces a small difference between the two results. The capacitance measurement is based on differential measurement in order to increase the total capacitance change and consequently to improve the sensor sensitivity along the X- and Y- axis. The initial capacitances values are 2 pF, 2.7 pF and 0.9 pF along X-, Y- and Z-axis, respectively. Fig. 4.7 illustrates the calibration curves for the capacitance output versus the input acceleration. The maximum displacement for sensor comb structure is fixed to 25% from the initial gap d_1 in order to insure good linearity over [0–50 g] measurement range. Fig. 4.7(a) and (b) each show two curves that represent the variation along X- and Y- axis side of the inter-digitized comb fingers, respectively. Fig. 4.7(c) represents only one curve as the measurement is absolute along Z-axis. The sensitivities, given by the slopes of each curve, are 8.55 fF/g, 18.03 fF/g and 2.64 fF/g with maximum range of 957 fF, 2.10 pF and 269 fF along X-, Y- and Z-axis, respectively.

4.3.2. Accelerometer performance

Underdamped response has the advantage to increase the quality factor and thus achieve low noise performance in an accelerometer [11]. In addition, a higher Q-factor can help to improve the response time of the accelerometer. Both the vacuum maintained inside the sealed cavity and the device geometry control the damping coefficient and consequently the quality factor. The MIDIS process offers vacuum encapsulation of the device wafer at 10 mTorr. Further, the damping due to the geometry effect is analyzed using mainly two damping mechanisms, the slide air-film and the squeezed air-film damping, that are confined in the 2 µm gap between the central proof mass and the top wafer. Fig. 4.8 shows the results of the damping coefficient over

the operating frequency range indicating the dominance of the squeezed air-flow mechanism (0.092 µN/µm/s) over the slide film damping (5.26E–10 µN/ µm/s). Likewise, the effect of inter-digital fingers was analyzed using Stokes flow regime and the damping coefficients values are 9.26E–8 µN/µm/s and 1.518E–7 µN/µ/s along X- and Y- axes, respectively.

4.4. Experimental results and discussion

The tri-axial accelerometer device is fabricated using MIDIS process from TDSI, which includes a 30 µm thick device wafer. The detailed cross-sectional view of a typical device in MIDIS process is shown in Fig. 4.9(a) with the different layers involved in the device fabrication. Fig. 4.9(b) shows the microscope image of the cross-section of the fabricated tri-axial accelerometer device. The TSV interconnect layer is bonded to the device wafer through thin intermediate conductive layer of 2 µm (also illustrated in Fig. 4.4(a). Further, MIDIS process provides the fabrication of recessed fingers with a height difference of 4 µm between the fixed and the moving combs as shown in Fig. 4.9(a). The above two features, gap of 2 µm between the two electrodes using oxide material as insulating layer and recessed fingers with a height difference of 4 µm, were exploited to enable detection along Z-axis.

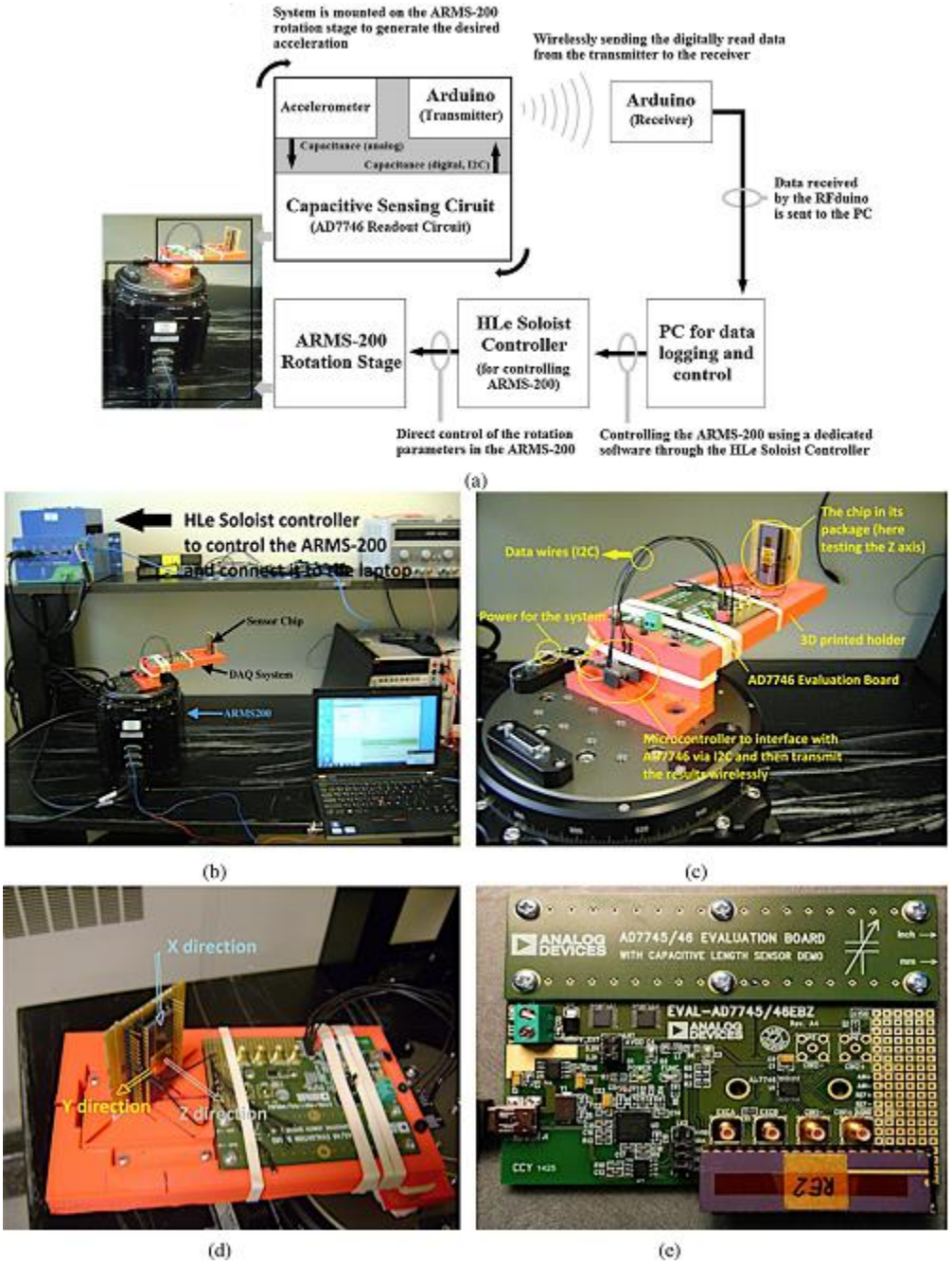

Figure 4.10 (a) Schematic of the experimental setup for testing the accelerometer sensor. (b) Picture of the experimental setup for testing the accelerometer sensor. (c) Close-up of the custom-built chip carrier installed over the horizontal shaker, (d) experiment setup for testing the cross-axis sensitivity performance. (e) Analog DevicesAD7746Capacitance to Digital Converter (CDC) circuit board.

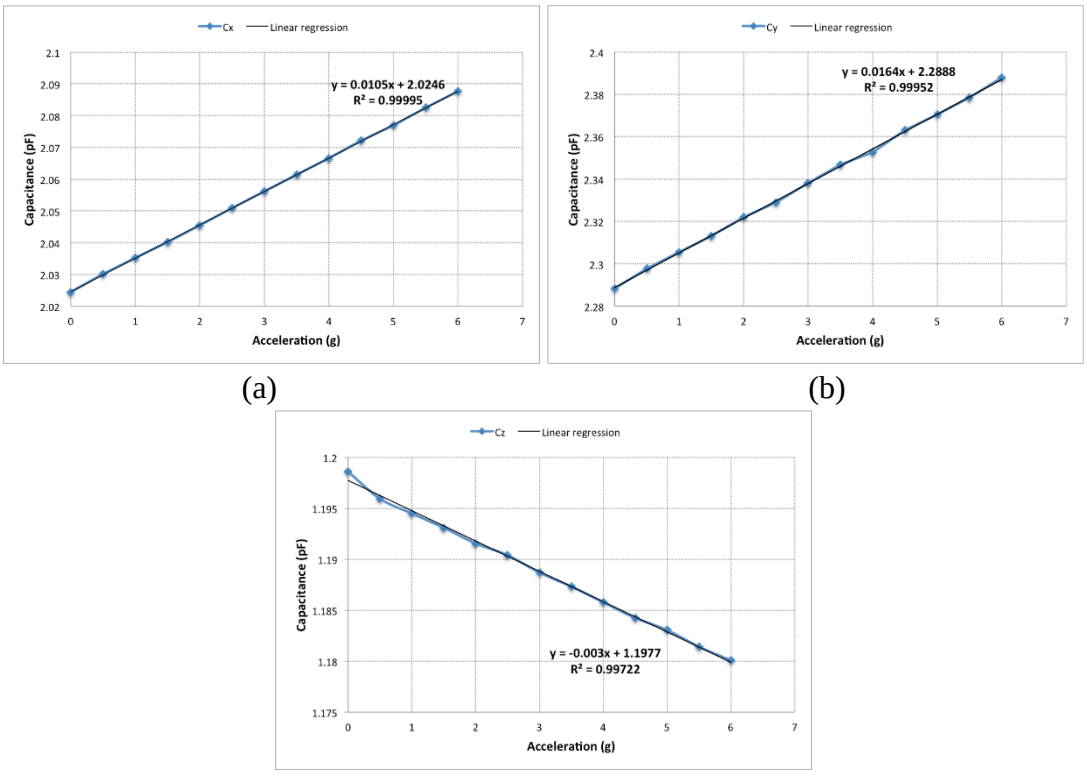

Figure 4.11 Experimental results for the accelerometer sensor. (a) Along X-axis. (b) Along Y-axis. (c) Along Z-axis

At this time, the process steps of the MIDIS process is maintained confidential by the TDSI foundry. Hence, Table 4-1 only listed the main structural features of MIDIS process. Fig. 4.10(a) and (b) shows the schematic and picture experimental setup for testing the sensor performance using the horizontal shaker ARMS-200 rotary motion simulator from Aerotech Inc., respectively. The sensor testing is done by placing the chip in different positions along the principle axes (X, Y and Z) as shown in Fig. 4.10(c). In first experiment, the measurements determined the sensor sensitivity and resolution along the various axis, while relying on the measured Total Noise Equivalent Acceleration (TENA) [36]. In the second experiment, we performed experiments to measure cross-axis sensitivity performance by placing the accelerometer at 45◦ for each couple of axes (X, Y), (X, Z) and (Y, Z) as shown in Fig. 4.10(d), through which the acceleration components along two axis can be measured. Here, the objective

is to compare the measured acceleration components in the second experiment to the value obtained from the first experiment. The sensor readout circuit is a 24-bit 2-channel ∑-Δ capacitance-to-digital convertor (AD7746) offered by Analog Devices Inc. as shown in Fig. 4.10(e). AD7746 includes an oversampling 24-bit ∑-Δ modulator and signal processing circuitry for noise shaping and filtering which helps to significantly minimize the noise and therefore enhances the measurement accuracy. The shaker allows acceleration only along one axis in range of 0–6 g. The AD7746 readout circuit was interfaced to Arduino microcontroller via I2C interface to transmit the acquired measurements to a personal computer. Fig. 4.11 illustrates the different calibration curves, that is, capacitance output versus the acceleration input, with its linear regression curves through which the sensitivity was deduced from the slope. The experimental results in Fig. 4.11 are very close to the results found in simulation study and the sensitivities values are 10.5 fF/g, 16.4 fF/g and 3 fF/g along X-, Y- and Z- axis, respectively. Fig. 4.12 shows the experimental results for the calibration curves of each couple axis, that is, (X,Y), (X,Z) and (Y,Z). The slope of the curve representing the sensor sensitivity is extremely close to the values found in the case of single acceleration component where the sensor is directed along the radial axis. In other words, two orthogonal accelerations are simultaneously applied to study the response of the sensor along the two orthogonal axes. We were able to obtained six calibration curves with slopes representing the sensitivities that are very close to the results obtained in the first experiment, as shown in Fig. 4.11. Here, the small differences in the experimental results can be explained by the noise generated due to the electric motor in the ARMS-200 rotary motion simulator. Further, there are small discrepancies that arise between the experimental results to the initial testing conditions as it is difficult to accurately place the test chip at 45◦ on a high speed rotating stage.

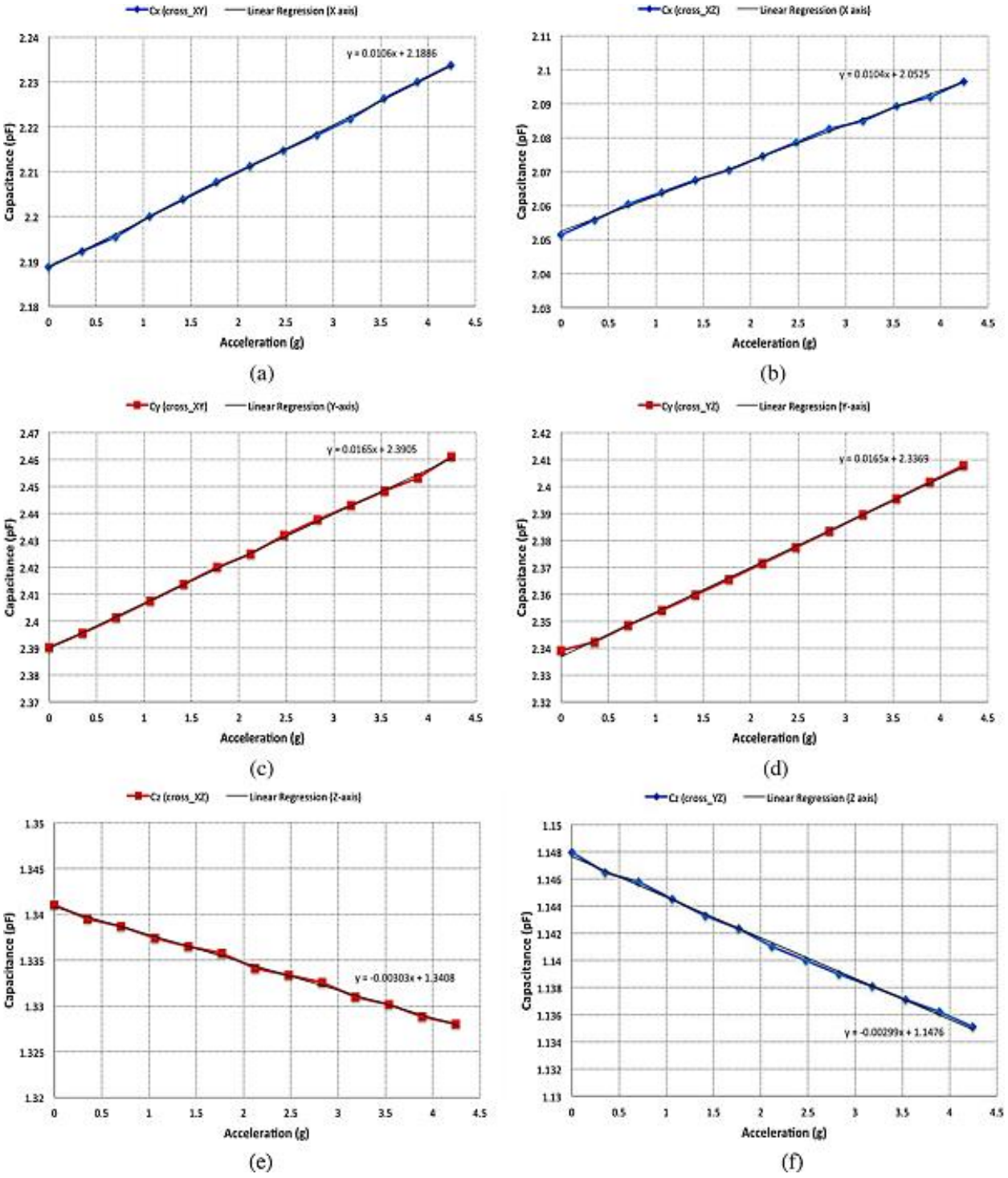

Figure 4.12 Experimental results for evaluating the cross-axis sensitivity by placing the accelerometer at 45◦ for each couple of axes (X, Y), (X, Z) and (Y, Z). (a) Measured X-axis component from coupled (X/Y) axis measurement (b) measured X-axis component from coupled (X/Y) axis measurement (d) measured Y-axis component from coupled (Y/Z) axis measurement. (e) Measured Z-axis component from coupled (X/Z) axis measurement (f) measured Z-axis component from coupled (Y/Z) axis measurement

Table 4-1 Features of the MIDIS fabrication process

Feature	*Thickness*	*Min feature (µm)*	*Min spacing (µm)*	*Max Spacing (µm)*
Device wafer	30	1.5	1.5	-
Top interconnect wafer	180	10	50	-
Bonding plane	2	50	10	700
Handle wafer	380	20	50	-

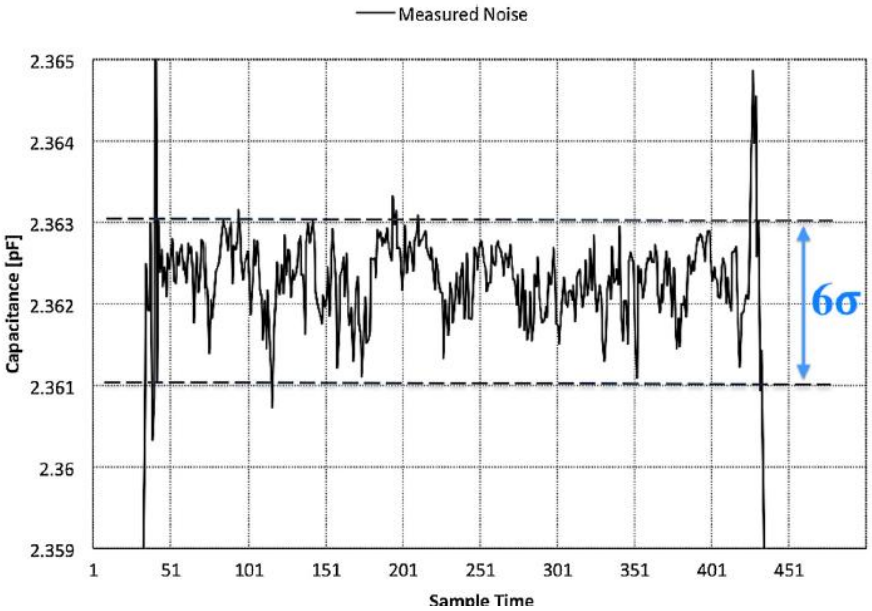

Figure 4.13 Total equivalent noise measurement

Table 4-2 The experimental specifications for the described tri-axial accelerometer sensor

	In plane Measurement		**Out of plane Measurement (z-axis)**	**MODEL 7503A5 accelerometer [37]**
	X-axis	Y-axis		
Measurement range (g)	[0-6]g			±50g
Sensor sensitivity (fF/g)	10.5	16.4	3	40 mV/g
Resolution (mg)	2.8	1.8	10	3.35
Mechanical noise (µg/√Hz)	1.04×10^{-2}	0.1415	19.2	75
Cross-axis sensitivity (%)	1.3	0.86	1.05	3

Dimensions (l × w × h) (μm)	1000 x 1000 x 30	-

Table 4-3 The simulation specifications for the described tri-axial accelerometer sensor

	In plane Measurement		**Out of plane Measurement (z-axis)**
	X-axis	Y-axis	
Measurement range (g)	±50g		
Sensor sensitivity (fF/g)	8,55	18.03	2.64
Resolution (mg)	3.5	1.6	11.3
Spring stiffness (μN/ μm)	23.4	38.7	51.8
Resonant frequency (kHz)	4.3	4.1	8.3
Cross-axis sensitivity (%)	0	0	0
Dimensions (l × w × h) (μm)	1000 x 1000 x 30		

Low noise operation represents an important parameter for the specification of the accelerometer. The noise floor is mainly established by two factors, namely, the signal conditioning circuit and the mechanical noise which is caused by the air viscosity inside the accelerometer package. The noise spectral density referred to the input acceleration is given by the Eq. (4.9) [36], where kB, T, Q are the Boltzmann constant, the working temperature and the quality factor, respectively.

$$a_n = \sqrt{\frac{4k_B T \omega_n}{Q}} \tag{4.9}$$

The MIDIS process allows low noise performance as it includes two unique features that are not currently available through any other commercial MEMS foundry. First, a thick structural

device wafer of 30 μm that adds significant mass, and second, ultra-clean wafer level vacuum encapsulation at 10 mTorr which leads to a high Q factor (quality factor) through the reduction in the damping effect. Experimentally, the total equivalent noise (TENA) measurement is performed under 1-g input acceleration and is deduced from the 6σ uncertainty defined by the signal limits as illustrated by Fig. 4.13. In this experiment, we deduced this parameter along Y-axis as an example and it is around 0.33 fF and this leads to a resolution of 1.8 mg for a given bandwidth of 32 Hz. From Fig. 4.13, the data shown near the start and end shows a large signal variation due to the tilting of test chip to collect suitable data. As predicted through the damping mechanism, in the current design the dominant mechanical noise is generated along Z-axis and it is estimated to be 19.2 μg/$\sqrt{\ }$Hz. Table 4-2 summarizes the important specifications that describe the novel tri-axial accelerometer sensor and includes a commercial capacitive tri-axial accelerometer for comparison.

4.5. Conclusions

We presented the design, fabrication and testing of a wafer level vacuum encapsulated tri-axial capacitive accelerometer with low cross-axis sensitivity. The accelerometer is fabricated in the new MIDIS process recently introduced by TDSI. Our approach of using a standard MEMS process provides a promising option allowing highly efficient and reproducible manufacturing at large volumes, lower cost, and high yields. The wafer level vacuum encapsulation of our proposed accelerometer provides benefits in reducing the overall product cost, simplifying packaging constraints, and easing supply-chain logistics. The described accelerometer included several novel features including integrated structure using decoupled frames supported by strategically designed springs and employing capacitive compensators for the purpose of achieving low cross-axis sensitivity.

Acknowledgments

We would like to acknowledge the financial support given by Natural Sciences and Engineering Research Council of Canada (NSERC). We would like to acknowledge the access to MIDIS fabrication process provided by Canada Microelectronics Corporation (CMC).

References

[1] V. Kempe, *Inertial MEMS Principles and Practice*. New York: Cambridge University Press 2011.

[2] M. Kraft and N. M. White, *MEMS for automotive and aerospace applications*. USA, Philadelphia: Woodhead Publishing Limited, 2013.

[3] H. Byeoungju, O. Yongsoo, L. Byeungleul, K. Y. Park, B. Seongsoon, A. Seoungdo, *et al.*, "Area variable capacitive microaccelerometer with force-balancing electrodes," in *Position Location and Navigation Symposium, IEEE 1998*, 1998, pp. 146-151.

[4] Analog-Devices. Available: http://www.analog.com/en/products/mems/mems-accelerometers.html

[5] ST-Microelectronics. Available: http://www.st.com/web/en/catalog/sense_power/FM89/SC444?icmp=sc444_pron_accelerometers_aug2013&sc=accelerometers-nb-aug13

[6] Freescale-Semiconductor. Available: http://www.freescale.com/webapp/sps/site/overview.jsp?code=ACCLOWG

[7] Invensense. Available: http://www.invensense.com/mems/gyro/sixaxis.html

[8] BOSCH-Sensortec. Available: https://www.bosch-sensortec.com/en/homepage/products_3/3_axis_sensors/3-axissensors

[9] M. A. Lemkin, B. E. Boser, D. Auslander, and J. H. Smith, "A 3-axis force balanced accelerometer using a single proof-mass," in *Solid State Sensors and Actuators, 1997. TRANSDUCERS '97 Chicago., 1997 International Conference on*, 1997, pp. 1185-1188 vol.2.

[10] S. Butefisch, A. Schoft, and S. Buttgenbach, "Three-axes monolithic silicon low-g accelerometer," *Journal of Microelectromechanical Systems*, vol. 9, pp. 551-556, 2000.

[11] C. Junseok, H. Kulah, and K. Najafi, "A monolithic three-axis micro-g micromachined silicon capacitive accelerometer," *Journal of Microelectromechanical Systems*, vol. 14, pp. 235-242, Apr 2005.

[12] Q. Hongwei, F. Deyou, and X. Huikai, "A Monolithic CMOS-MEMS 3-Axis Accelerometer With a Low-Noise, Low-Power Dual-Chopper Amplifier," *Ieee Sensors Journal*, vol. 8, pp. 1511-1518, Sep 2008.

[13] C. M. Sun, M. H. Tsai, Y. C. Liu, and W. Fang, "Implementation of a Monolithic Single Proof-Mass Tri-Axis Accelerometer Using CMOS-MEMS Technique," *Ieee Transactions on Electron Devices*, vol. 57, pp. 1670-1679, Jul 2010.

[14] *MEMS Integrated Design for Inertial Sensors (MIDIS)*. Available: http://www.teledynedalsa.com/semi/mems/applications/midis/

[15] N. Yazdi, F. Ayazi, and K. Najafi, "Micromachined inertial sensors," *Proc of IEEE*, vol. 86, pp. 1640-1658, Aug 1998.

[16] H. Farahani, J. K. Mills, and W. L. Cleghorn, "Design, fabrication and analysis of micromachined high sensitivity and 0% cross-axis sensitivity capacitive accelerometers," *Microsystem Technologies*, vol. 15, pp. 1815-1826, Dec 2009.

[17] G. Li, Z. H. Li, C. S. Wang, Y. L. Hao, T. Li, D. C. Zhang, *et al.*, "Design and fabrication of a highly symmetrical capacitive triaxial accelerometer," *Journal of Micromechanics and Microengineering*, vol. 11, pp. 48-54, Jan 2001.

[18] A. Merdassi and V. P. Chodavarapu, "3-axis Capacitive Low-Gravity MEMS Accelerometer with Zero Cross-Axis Sensitivity in a Commercial Process," presented at the Nanotechnology 2013: Electronics, Devices, Fabrication, MEMS, Fluidics and Computational Washington D.C., 2013.

[19] P. Qu and H. W. Qu, "Design and Characterization of a Fully Differential MEMS Accelerometer Fabricated Using MetalMUMPs Technology," *Sensors*, vol. 13, pp. 5720-5736, May 2013.

[20] H. Farahani, J. K. Mills, and W. L. Cleghorn, "Design, fabrication and analysis of micromachined high sensitivity and 0% cross-axis sensitivity capacitive accelerometers," *Microsystem Technologies*, vol. 15, pp. 1815-1826, Dec 2009.

[21] F. Serrano-Vazquez, A. Herrera-May, and M. Bandala-Sanchez, "Design and modeling of a single-mass biaxial capacitive accelerometer based on the SUMMiT V process,"

Microsystem Technologies-Micro-and Nanosystems-Information Storage and Processing Systems, vol. 19, pp. 1997-2009, Dec 2013.

[22] A. Witvrouw, R. Van Hoof, G. Bryce, B. Du Bois, A. Verbist, S. Severi, *et al.*, "SiGe MEMS Technology: a Platform Technology Enabling Different Demonstrators," *Sige, Ge, and Related Compounds 4: Materials, Processing, and Devices,* vol. 33, pp. 799-812, 2010.

[23] C. Comi, A. Corigliano, A. Ghisi, and S. Zerbini, "A resonant micro accelerometer based on electrostatic stiffness variation," *Meccanica,* vol. 48, pp. 1893-1900, Oct 2013.

[24] S. H. Lee, J. Mitchell, W. Welch, S. Lee, and K. Najafi, "Wafer-level vacuum/hermetic packaging technologies for MEMS," *Reliability, Packaging, Testing, and Characterization of Mems/Moems and Nanodevices Ix,* vol. 7592, 2010.

[25] B. Lee, S. Seok, and K. Chun, "A study on wafer level vacuum packaging for MEMS devices," *Journal of Micromechanics and Microengineering,* vol. 13, pp. 663-669, Sep 2003.

[26] R. Gooch, T. Schimert, W. McCardel, B. Ritchey, D. Gilmour, and W. Koziarz, "Wafer-level vacuum packaging for MEMS," *Journal of Vacuum Science & Technology A,* vol. 17, pp. 2295-2299, 1999.

[27] M. Dienel, M. Naumann, A. Sorger, D. Tenholte, S. Voigt, and J. Mehner, "On the influence of vacuum on the design and characterization of MEMS," *Vacuum,* vol. 86, pp. 536-546, Jan 5 2012.

[28] Y. Jeong, D. E. Serrano, V. Keesara, W. K. Sung, and F. Ayazi, "Wafer-Level Vacuum-Packaged Tri-Axial Accelerometer with Nano Airgaps," *26th Ieee International Conference on Micro Electro Mechanical Systems (Mems 2013),* pp. 33-36, 2013.

[29] A. Merdassi, P. Yang, and V. P. Chodavarapu, "Wafer Level Vacuum Encapsulated Capacitive Accelerometer Fabricated in an Unmodified Commercial MEMS Process," *Sensors* vol. 15, pp. 7349-7359, 2015.

[30] G. Krishnan, C. U. Kshirsagar, G. K. Ananthasuresh, and N. Bhat, "Micromachined High-Resolution Accelerometers," *Journal of the Indian Institute of Science*, vol. 87, pp. 333-361, September 2007.

[31] C. S. Premachandran, S. C. Chong, S. Liw, and R. Nagarajan, "Fabrication and Testing of a Wafer-Level Vacuum Package for MEMS Device," *IEEE Transactions on Advanced Packaging*, vol. 32, pp. 486-490, 2009.

[32] J. Xie, R. Agarwal, Y. Liu, and T. J. Minglin, "A three-axis SOI accelerometer sensing with both in-plane and vertical comb electrodes," *Microsystem Technologies-Micro-And Nanosystems-Information Storage And Processing Systems*, vol. 18, pp. 325-332, Mar 2012.

[33] N. Lobontiu. (2010, March). *System Dynamics for Engineering Students*.

[34] A. Umeda, M. Onoe, K. Sakata, T. Fukushia, K. Kanari, H. Iioka, *et al.*, "Calibration of three-axis accelerometers using a three-dimensional vibration generator and three laser interferometers," *Sensors And Actuators A-Physical*, vol. 114, pp. 93-101, Aug 20 2004.

[35] VTI-Technolgies. (2005). *Cross-axis Compensation*. Available: http://www.murata.com/~/media/webrenewal/products/sensor/inclinometer/sca103t/an32_cross-axis_compensation.ashx?la=en-gb

[36] A. Babak Vakili and A. Farrokh, "Micro-gravity capacitive silicon-on-insulator accelerometers," *Journal of Micromechanics and Microengineering*, vol. 15, p. 2113, 2005.

[37] DYTAN-Instruments.Inc. *Model 7503A5, High Precision Triaxial MemsAccelerometer*. Available: http://72.34.224.196/Model-7503A5-High-Precision-Triaxial-MEMS-Accelerometer-P1396.aspx

CHAPTER -5

5. Wafer-Level Vacuum-Encapsulated Rate Gyroscope with High Quality Factor in a Commercial MEMS Process

We report the design and fabrication of a rate gyroscope sensor that is characterized by a high Quality Factor (*Q*) (52,300), unmatched resonance mode and low noise performance. The gyroscope dimensions are 1800 µm x 850 µm with 30 µm device thickness. The gyroscope comprises of a symmetrical resonator for the drive mode oscillation and uses differential capacitance measurement for inertial sensing. The gyroscope is fabricated using MEMS Integrated Design for Inertial Sensors (MIDIS) process, which is a new microfabrication process developed by Teledyne DALSA Semiconductor Inc. (TDSI). This new microfabrication technology offers wafer-level encapsulation under high vacuum pressure of 10 mTorr and includes Through Silicon Vias (TSVs) that allows flip-chip bonding with an integrated circuit for signal detection and processing. The fabricated gyroscope was tested and it exhibited a sensitivity of 0.8fF/º/s with excellent linearity over a wide input angular velocity range of ±1000º/s and a high rate resolution of 0.71°/s.

Keywords

Capacitive gyroscope; Rate gyroscope; High Quality factor gyroscope; MIDIS process; Unmatched mode; Zero-level vacuum encapsulation; Wafer-level packaging; Commercial MEMS process.

5.1. Introduction

Gyroscope is an essential component of a multi degrees-of-freedom (DOF) inertial measurement unit (IMU) that is used in a wide range of consumer, industrial, medical and military applications to track the relative motion and position of an object in space [1, 2]. Today, microelectromechanical systems (MEMS) based IMUs are widely available as a single-package and single-chip form factors that integrate both the sensor devices and interface electronics components [3]. The recent more advanced 9-DOF MEMS IMUs available in the market consist of a tri-axial accelerometer, gyroscope, and a magnetometer. Here, accelerometers measure linear motion along the *x*, *y*, and *z* axes (axial acceleration) and gyroscopes measure rotation (angular velocity) around these axes. The multi-DOF MEMS IMUs are used in a number of consumer applications such as human physical activity monitoring, gaming devices, active stabilization in cameras, and virtual reality, industrial applications such as robotics, vehicle stability control, and machine and vibration monitoring and military applications such as guidance and navigation [1, 2, 4-6].

Precision grade IMUs, such as tactical and inertial navigation grade IMUs, are crucial components in navigation and guidance systems in aerospace and defense applications [7], autonomous vehicle navigation [8], deep-bore energy extraction, precision industrial automation, and human biomechanical analysis [9]. High-sensitivity multi-DOF MEMS based accelerometers are available that are well suited for these applications. However, 6-DOF MEMS IMUs are yet to prove their functionality in the high precision motion and navigation applications where the limiting factor here is the lack of high accuracy MEMS gyroscopes. MEMS gyroscopes are prone to noise and bias drift that result in fast-growing errors during computation of the orientation and, thus, do not allow for extended periods of navigation [10, 11]. There is an urgent research need to develop silicon-based MEMS gyroscopes that are low

cost, small area and low power for precision motion and navigation applications, that are currently satisfied by bulky, fragile, and high power consuming fiber-optic and ring laser gyroscopes.

High-performance gyroscopes have stringent requirements, including low Angle Random Walk (ARW), low bias drift, high scale-factor, and scale-factor stability, while being low cost, small size, and low power consumption. Vibratory gyroscopes measure rotation rate (Ω) or angle (θ) by detecting changes in the vibration patterns caused by the Coriolis force. Depending on whether gyroscopes measure Ω or θ, they are categorized as rate gyroscopes (RG) or rate-integrating gyroscopes (RIG), respectively. The proposed design is a rate gyroscope type. For a uniaxial vibratory MEMS gyroscope, the Coriolis force allows energy transfer between X-drive vibration and Y-sense vibration. The Y-sense sensitivity, Y/Ω, is given by Equation (5.1) [2],

$$S_{y/\Omega} = \left| \frac{y(j\omega)}{\Omega_z} \right| = \frac{2}{\omega_d} \frac{Q_d F_e / (k_x k_y)}{\sqrt{\left(1 - \left(\frac{\omega_s}{\omega_d}\right)^2\right)^2 + \left(\frac{\omega_s}{\omega_d Q_s}\right)^2}} \tag{5.1}$$

where, ω_d is the angular frequency along drive axis, m is the mass of the proof mass, F_e is the input electrostatic force, Q_x and Q_y are the Quality factors along X-drive and Y-sense axis, respectively, and k_x and k_y are the spring stiffness along X-drive and Y-sense axis, respectively. Further, the thermo-mechanical noise which is inversely proportional to $\sqrt{f \times Q}$, can be reduced by designing a high Q gyroscope [12]. Thus, the Q plays an important role in determining the sensitivity of the MEMS gyroscope.

At macro-scale, Hemispherical resonator gyroscopes (HRGs) functioning in the wineglass resonance mode have exhibited some of the highest Qs reaching as high as 26 million [13]. However, it is difficult to apply these fabrication methods at the micro-scale. MEMS based Hemispherical Resonator Gyroscope (HRG) developed by Pai *et al.* [14] have only achieved a modest *Q* of 20,000. Many research groups have previously developed MEMS gyroscopes with high Q's exceeding 50,000. The Quadruple Mass Gyroscope (QMG) developed by Prikhodko et al. [15] obtained *Qs* exceeding 1 million, that helps to achieve sub-deg/hr bias stability, Micro Birdbath Resonator Gyroscope (mu-BRG) developed by Cho *et al.* [16] has reached a *Q* of 249,000, and the **Disk Resonator Gyroscope** (**DRG**) developed by Taheri-Tehrani *et al.* [17] exceeded a *Q* of 100,000.

The *Q* is impacted from many different damping mechanisms, such as anchor loss, thermoelastic dissipation (TED), surface loss, and air damping [18]. MEMS gyroscopes require a good quality ultra-clean hermetic encapsulation with low leakage to help achieve a high *Q* and stability of the *Q* for long-term operation by reducing the air damping and surface losses [19]. The QMG device [15, 20-22] with *Q*s exceeding 1 million is packaged in a hermetic sealed ceramic package with a getter material coated on the glass lid that is used to seal the encapsulated cavity in the package. The use of ceramic packages and getters are an expensive and unreliable packaging technique sensitive to shock and vibration that severely limits the practical and long-term usability. A better packaging alternative is with wafer-level vacuum encapsulation of MEMS devices, that is currently extensively studied by various research groups as it plays a key role in improving the long term reliability with excellent resistance to shock and vibration [23-25]. Wafer-level vacuum packaging techniques allow the use of high volume low cost plastic packaging at the device level. Wafer level vacuum packaging of MEMS inertial sensors has been demonstrated previously by several other research groups [26-29]

using custom microfabrication processes. However, the above described microfabrication processes [26-29], do not provide ultra-clean and low-leak rate vacuum packaging required to achieve high Q and maintain that high Q over a long duration as needed for high performance MEMS gyroscopes. To our knowledge, the DRG device [17], is currently the only demonstrated gyroscope using ultra-clean wafer-level vacuum encapsulation. The DRG device is fully encapsulated using a wafer-scale encapsulation "epi-seal" process that is described in Candler, et al. [30].

Here, we describe the design and development of a wafer-level vacuum encapsulated rate gyroscope with a high *Q* of 52,300 using MEMS Integrated Design for Inertial Sensors (MIDIS) process, which is a new microfabrication process developed by Teledyne DALSA Semiconductor Inc. (TDSI). To our knowledge, we demonstrate the highest reported *Q* for an unmatched mode rate gyroscope that is wafer-level vacuum encapsulated. The MIDIS process offers wafer-level encapsulation under high vacuum pressure of 10 mTorr. Further, the MIDIS process is a better alternative to the "epi-seal" process [30] as it offers one of the world's lowest demonstrated total leak rate equivalent from the encapsulated vacuum cavity that varies from one fabrication run to another between 45 molecules/second (7.5×10^{-13} atm cm^3/s) to 2500 molecules/second [31, 32]. The lower leak rate in the MIDIS process slows the degradation of the *Q* of the encapsulated MEMS device and allows the device operation with desired specifications over a longer lifetime. The MIDIS process offers a 30 µm thick single crystal silicon device layer that allows a heavy proof mass that increases the device sensitivity, has ultra-low stress, and provides high reproducibility, good mechanical properties and excellent matching capabilities in mass-production.

The developed uniaxial gyroscope offers high angular rate measurement with full range up to 1000º/s for a given bandwidth >100Hz and has low noise, low power consumption, and low long-term drift. The proposed device uses a differential capacitive measurement with asymmetric electrode configuration capable of detection resolution of 0.71º/s over the input measurement range of ±1000º/s. The driving actuation is implemented using electrostatic micro-resonators through symmetrical inter-digitated fingers that enable both balanced and linear oscillating force at a resonance frequency of 6.7 kHz. The fabricated gyroscope uses strategic designs for the mechanical springs supporting the proof mass and employs split mode condition through the implementation of decoupled frame, which helps to reduce the cross-axis sensitivity. The high aspect ratio of the fabricated springs enables high precision detection and insures excellent stability for the oscillation movement induced by the driving resonator.

While aiming for high *Q*, MEMS gyroscopes are operated in a mode-matched condition where the two vibration modes are degenerate, which increases the sensitivity of the gyroscope. The QMG, mu-BRG and DRG are examples of mode-matched gyroscopes. High *Q* mode-matched MEMS gyroscopes require sophisticated control electronics to operate. Further, considering practical aspects in any microfabrication process, there are inherent imperfections generated during the fabrication process. High *Q* mode-matched gyroscopes such as QMG, mu-BRG and DRG, are more susceptible to fluctuations in their dynamic operational parameters with microfabrication and packaging imperfections. The proposed gyroscope is based on unmatched mode of operation, where we keep a certain frequency difference, Δf, between the resonant modes which insures better stability in the overall system with the trade-off of a lower *Q* compared to QMG, mu-BRG and DRG.

The described gyroscope is interfaced to a commercial off-the-shelf capacitance-to-digital converter (CDC) circuit from Analog Devices Inc. (Model AD7746) [33]. The AD7746 provides good performance in terms of low noise and direct I^2C interface to a microcontroller. The conditioning circuit employs a 24-bit 2-channel sigma-delta (Σ-Δ) capacitance-to-digital convertor that offers excellent noise immunity and high resolution. In many high *Q* MEMS gyroscopes, the noise associated with the electronics used for detection and control of the micro-mechanical movement is one of the dominant noise sources. Thus, AD7746 with its excellent noise immunity is well suited for the proposed high *Q* gyroscope.

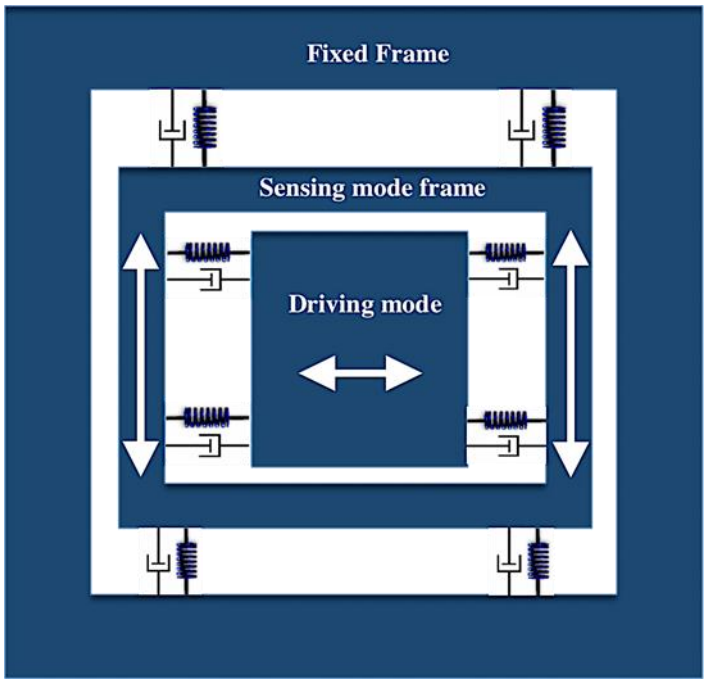

Figure 5.1 Operation principle and schematic of the Gyroscope

5.2. Operating Principle

The working principle of the proposed capacitive gyroscope sensor is based on the concept of Coriolis force induced by the rotation of the reference frame that supports a resonating proof mass. By applying the movement decomposition theory, one could deduce the Coriolis force

expression according to Equation (5.2). The generated force is perpendicular to the direction of the resonating proof mass and its magnitude is proportional to the angular velocity, Ω [34] as,

$$F_c = m \times a_c = m(2\Omega v) \tag{5.2}$$

where a_c is the Coriolis acceleration, m the mass of the proof mass, Ω the angular velocity with respect to the reference frame and v the velocity of the vibrating element. Figure 5.1 shows the design of the proposed uniaxial gyroscope. The design consists of a central proof mass supported by the sensing frame that are each connected by two different kinds of spring structures. This design allows functioning under split mode condition, where the sense and drive modes are separated through the use of a decoupling frame. The driving element uses a micro-resonator that can actuate the central proof mass in continuous oscillation along X-axis. The sensing mode is implemented along Y-axis that corresponds to the Coriolis force direction. Thus, X-axis oscillations will have no impact on the sensing frame as shown by Figure 5.1. Each axis can be modeled by a spring-mass system with its associated damping coefficients, c_x and c_y, along X- and Y- axis, respectively. Here, one could deduce the dynamic equations that govern the gyroscope motion according to Equation (5.3) [35] as,

$$\begin{cases} m\ddot{x} + c_x\dot{x} + k_x x = F_e \\ m\ddot{y} + c_y\dot{y} + k_y y = F_y - 2m\Omega_z\dot{x} \end{cases} \tag{5.3}$$

where c_x and c_y are the damping coefficients along X- and Y- axis, respectively, k_x and k_y are the spring stiffness along X- and Y- axis, respectively, Ω_z is the angular velocity around Z-axis and F_e the actuation force. The driving system consists of mechanical resonator that can be modeled by 1-DOF spring-mass system excited by harmonic electrostatic force, F_e. Under ultra-low damping condition, the maximum amplitude can be expressed in terms of Q_d (Q-factor of the drive resonator) by Equation (5.4) [35] as,

$$x_{\max} = \frac{F_e}{k_x} Q_d \tag{5.4}$$

Finally, the sensed displacement that can be converted into electrical signal and is given by Equation (5.5) [35]. Thus, one could improve the sensor sensitivity by increasing the *Q* factor and implementing a heavy proof mass.

$$y_{stat} = \frac{F_c}{k_y} = \left| \frac{2Q_d F_e}{m_d \omega_d} \frac{1}{\left(\omega_s^2 - \omega_d^2\right)} \right| \Omega_z \tag{5.5}$$

5.3. Electromechanical Design and Simulation Results

Figure 5.2(a) and 2(b) show the 2D model and cross-sectional view of the gyroscope, respectively. The proposed gyroscope design aims to achieve a high *Q* electrostatic resonator with good stability at the input and an ultra-low noise sensing transducer at the output. The drive system consists of a rectangular proof mass suspended by U-shaped mechanical springs with inter-digitated comb-drive that allows balanced actuation scheme and linearized force with respect to the excitation voltage as illustrated by Figure 5.3.

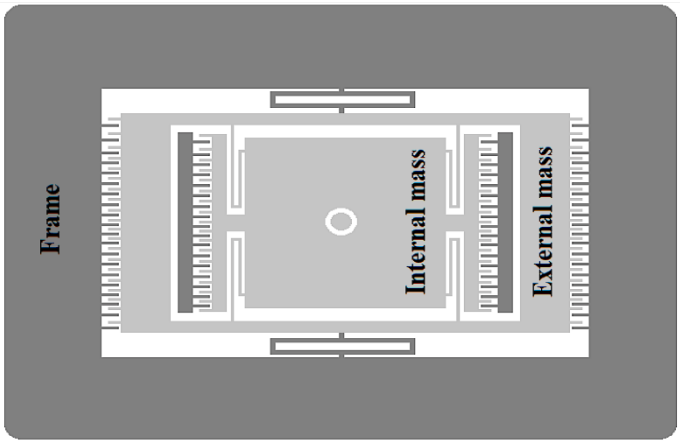

(a)

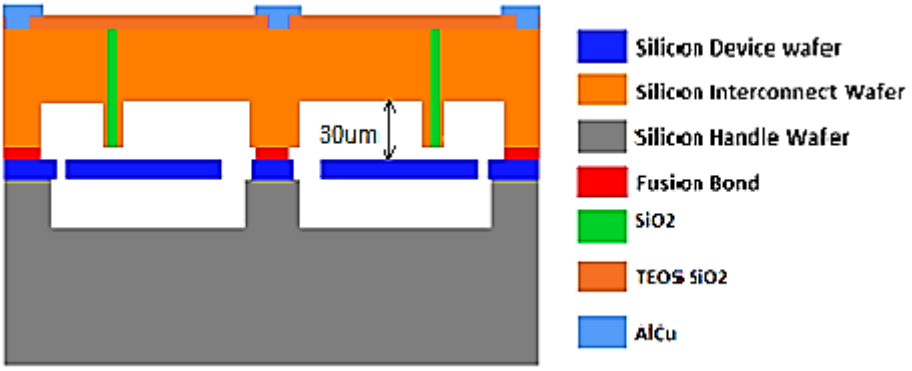

(b)

Figure 5.2 (a) 2-D schematic of the capacitive gyroscope. (b) Cross-sectional structure of the gyroscope

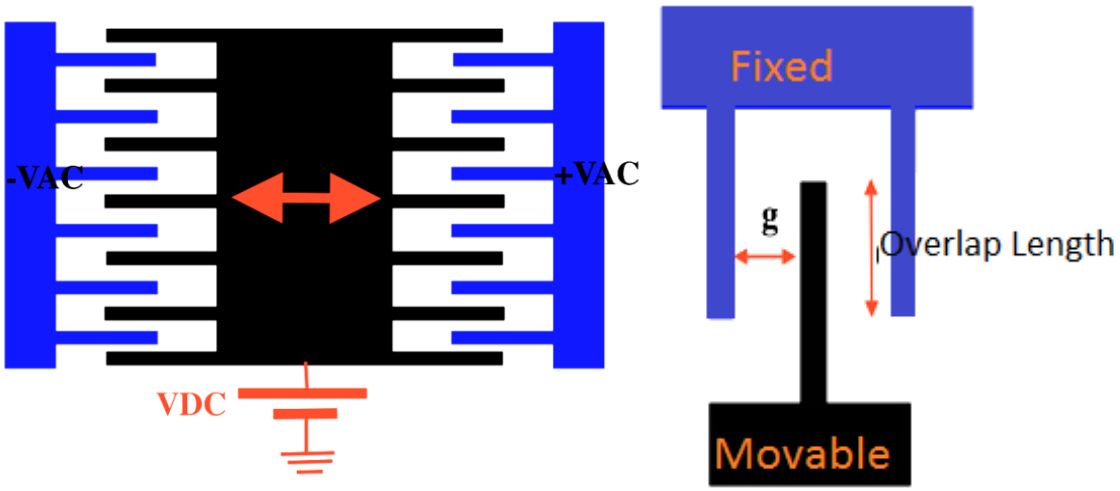

(a) (b)

Figure 5.3 Geometrical parameters of the comb drive resonator

The sensing frame that maintains the drive resonator is suspended by sagittal springs that enable the detection along Y-direction. The device thickness is fixed by MIDIS fabrication process at 30µm. A larger frame size allows a heavier proof-mass that helps to lower noise and higher sensitivity for the gyroscope. Due to the high aspect ratio and the strategic design of the mechanical springs, the cross-talk between the drive- and sense- modes is drastically minimized and two separated mass-spring systems of 1-DOF can be modeled along X- and Y-axis at the same time. Based on the inertial force concept, the mechanical sensitivity, which expresses the

displacement variation along the sense axis with respect to the angular velocity, can be approximated in unmatched mode condition by Equation (5.6) as,

$$S_{mech} = \frac{\Delta y}{\Delta \Omega_z} = \left| \frac{2Q_d F_e}{m_d \omega_{nd}} \frac{1}{\left(\omega_{ns}^2 - \omega_{nd}^2\right)} \right| \tag{5.6}$$

where, ω_{nd} and ω_{ns} are the natural angular frequency along drive and sense axis, respectively and Q_d is the Quality factor of the drive resonator.

The symmetric architecture of the comb drive has the advantage to linearly increase the overlap between fingers without any pull-in effect. Hence, the excitation force depends mainly on the gap, *g*, between fingers and the electrodes thickness, *h*, as given by Equation (5.7),

$$F_e = 4\frac{\varepsilon_0 h}{g} N V_{DC} V_{AC} \tag{5.7}$$

Both the minimum allowable gap, *g* (2µm), and electrode thickness, *h* (30µm), are fixed by the MIDIS fabrication process specifications. The overlap between the inter-digitated fingers is kept to its minimum limit to minimize the parasitic noise induced by the lateral forces, which improves the lateral stability of the comb-drive resonator. The U-folded beams and sagittal shapes of each spring enable perfect translatory motion of the rigid bodies along X- and Y- axis [36]. Each spring unit consists of two fixed-guided beams connected in series with equivalent stiffness spring constant as given by Equation (5.8),

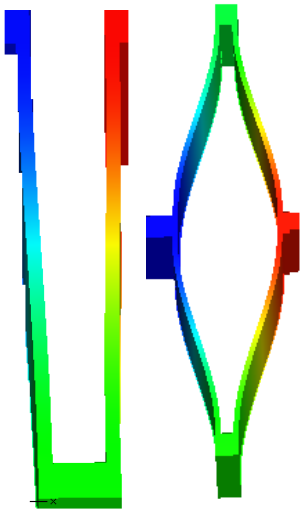

Figure 5.4 Deflection of U-shape and Sagittal based spring units

$$k_{xT} = 2Eh\left(\frac{w}{l}\right)^3 \tag{5.8}$$

where w, h and l represent the width, thickness and the length of each beam, respectively.

Finite Element Method (FEM) analysis is employed to simulate the drive and sense modes characterizing each as a 1-DOF spring-mass system and to simulate the slide damping mechanism which plays an important role in the sensor performance.

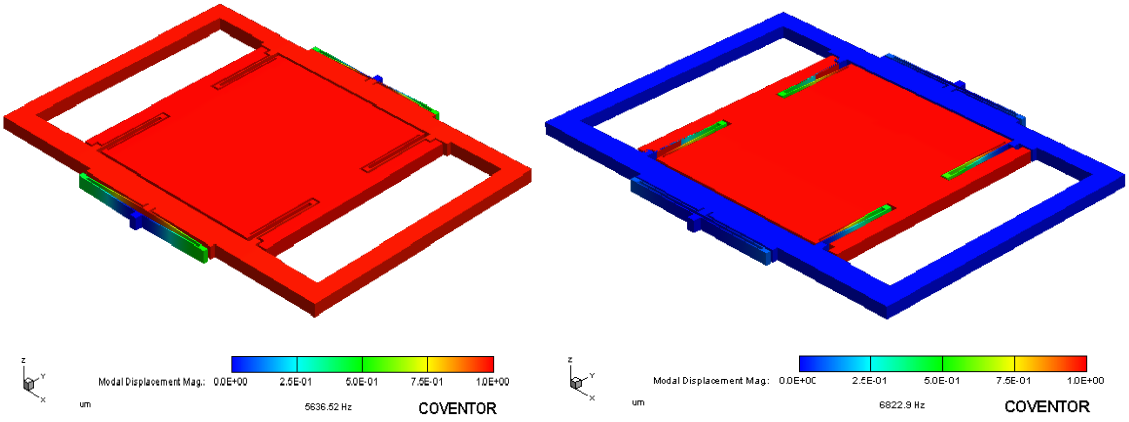

(a) (b)

Figure 5.5 FEM modal analysis. (a) Sense Mode. (b) Drive mode

Figure 5.5 shows the drive mode fixed at 6.822 kHz along X-axis and the sense mode fixed at 5.636 kHz along Y-axis. The frequency analysis depicted by Figure 5.6 confirms the maximum Coriolis force at the resonance frequency, which is 6.822 kHz. The electromechanical simulation was performed using lumped modeling through Architect module solver, which is integrated with CoventorWare Software. This approach enables integration of the signal conditioning circuit with the gyroscope sensor and a full electromechanical simulation can be performed with transient analysis. The mechanical sensitivity can be deduced from the slope of the graph as shown in Figure 5.7.

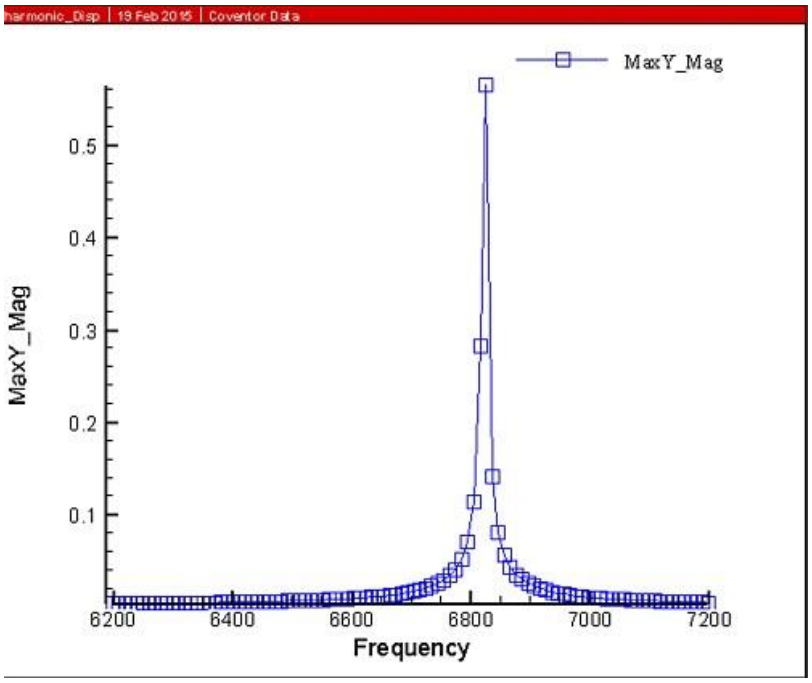

Figure 5.6 Frequency response of the gyroscope under fixed angular rotation of 1000º/s

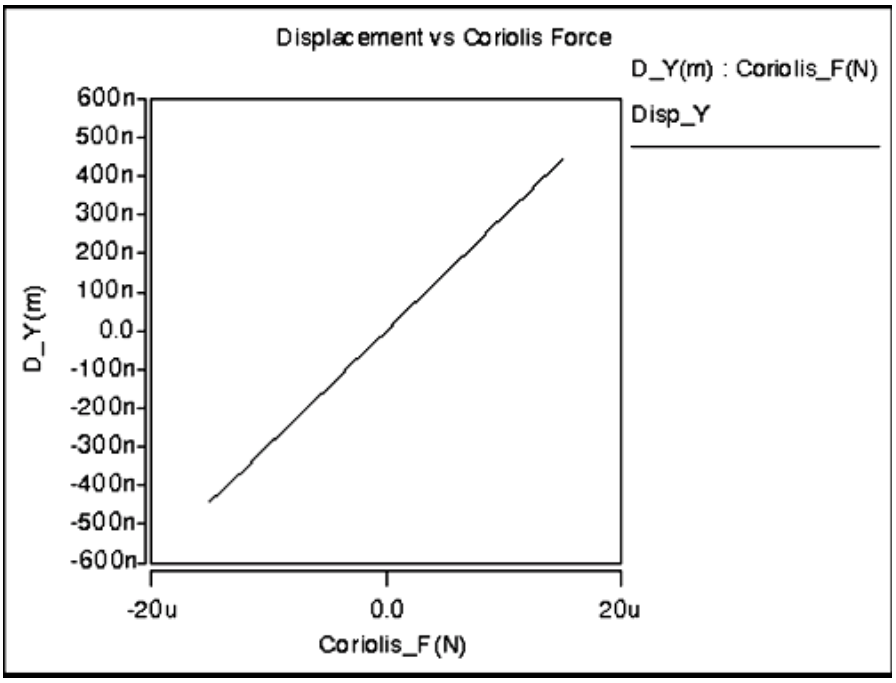

Figure 5.7 Displacement variation under the application of the Coriolis force

Figure 5.8 shows the transient simulation during the startup time for the driving oscillation along X-axis over a short time period of 3ms. The maximum amplitude reached in this case is equal to 0.12µm, which is much lower than the steady state value at 10µm. Figure 5.8(b)

illustrates the simulation results by running the solver at its operating steady-state value under the application of $V_{DC}(1V)\pm V_{AC}(1V)$ yielding to an amplitude of 1µm.

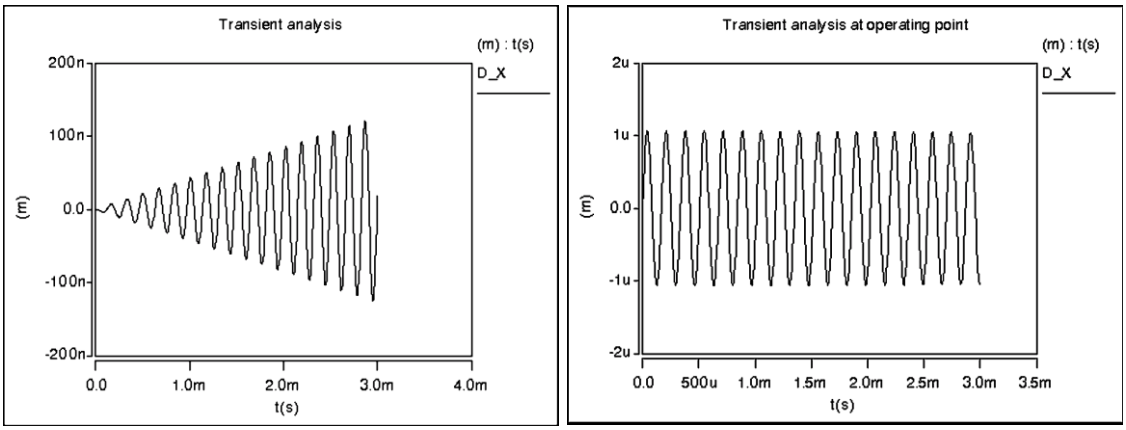

(a) (b)

Figure 5.8 Transient analysis. (a) Start-up transient analysis over 3ms time period. (b) Transient analysis at steady-state operating point

Figure 5.9 shows the electrical transduction design that is based on asymmetric configuration of the inter-digitized fingers and using two different gaps (d_1 and d_2) that yields to a differential measurement mode. Under the assumption of small displacement, one can deduce the electrical sensitivity, S_{elec}, according to Equation (5.9). The DC capacitance (C_0) value is fixed at 2pF with ΔC_{max} range of 590fF. The ratio between d_1 and d_2 is optimized to a numerical factor of 3.

$$S_{elec} = C_0 \frac{d_2 - d_1}{d_2 d_1} \tag{5.9}$$

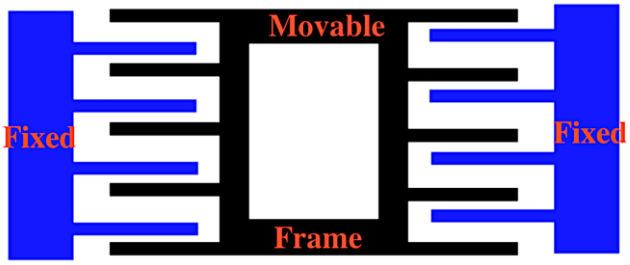

Figure 5.9 Asymmetric configuration of the capacitive transduction

The calibration curve that represents the capacitance variation with respect to the Coriolis force induced by the angular velocity rate as shown in Figure 5.10. Here, the two curves represent the two comb-fingers placed on the left and right sides of the moving frame. The symmetry structure of the two combs increases the sensor sensitivity. By measuring only one curve slope, one can calculate the overall sensor sensitivity as 18fF/μN.

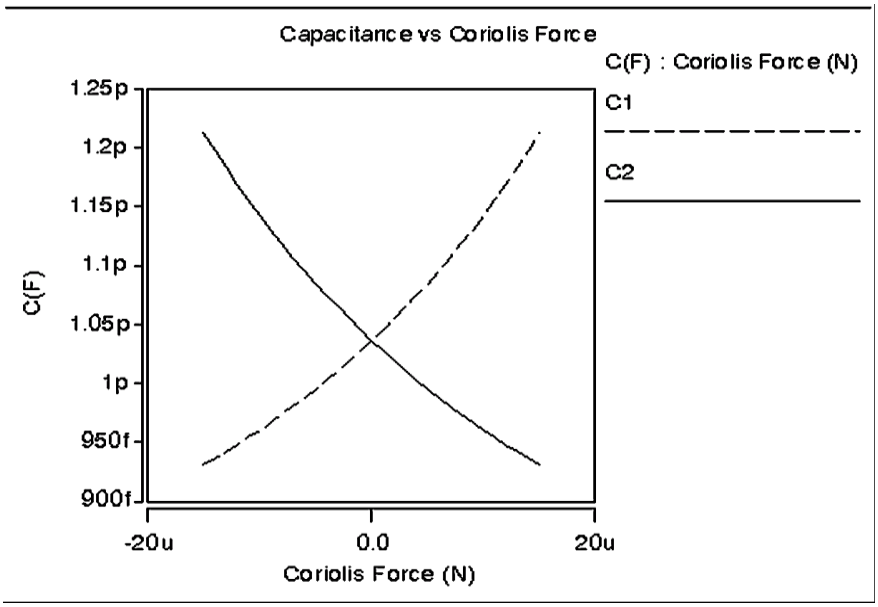

Figure 5.10 Illustration of the capacitance variation versus the generated Coriolis force

5.4. High Q-factor performance

The dynamic parameters play an important role in determining the gyroscope performance. One key factor to quantify the damping performance is to compute the damping coefficient for each mechanism. For instance, the Stokes damping coefficient can be expressed by Equation (5.10) as,

$$b_{sb} = \mu_{eff} \beta A \left(1 + \frac{1}{\beta d} \right) \tag{5.10}$$

where A represents the overlap area of the oscillating fingers, d the gap between fingers, μ is the effective viscosity of the air inside the encapsulated cavity and β is the momentum propagation velocity. Similarly, the squeezed damping coefficient is approximated by Equation (5.11) as,

$$b_{sf} = \mu_{eff} L \left(\frac{w}{h} \right)^3 \tag{5.11}$$

where L and w represents the length and width dimensions of the moving plate respectively.

Here, a high Q value helps to minimize the noise, increase the sensor sensitivity, and enhance the resolution. We employed several design strategies to improve the Q. First, a gap of 30μm wide is created between the capping layer (TSV layer) and the device layer to reduce the slide damping effect. Second, the short overlap length between inter-digitated fingers helps to minimize the damping mechanism originating from Stokes air flow that is confined between the inter-digitated fingers. Figure 5.11 shows the simulation result of the damping mechanism that is related to the squeezed air-film caused by the oscillation of the micro-resonator system and yields a damping coefficient of 3.7×10^{-7} (N//m/s) at the resonance frequency. The damping coefficient induced by the inter-digitated fingers in Stokes flow regime, reaches 1.7×10^{-6} (N/(m/s)).

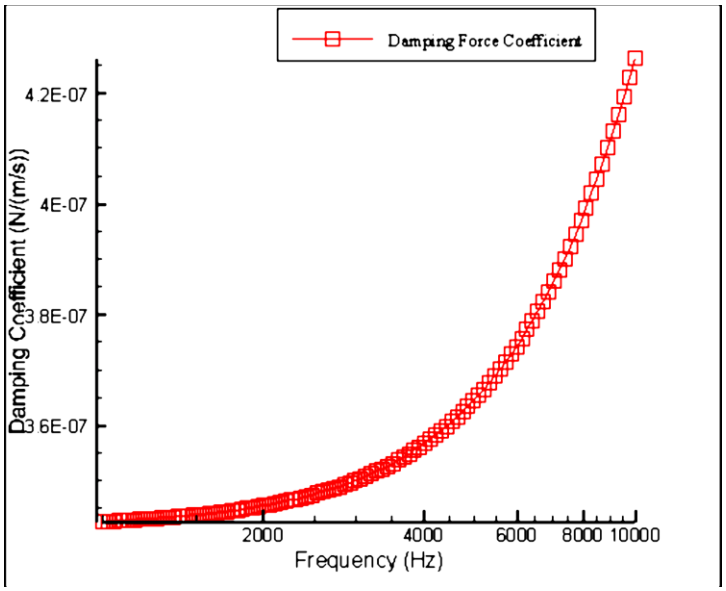

Figure 5.11 Slide film damping mechanism results

5.5. Experimental Results and Discussion

The gyroscope sensor is fabricated using MIDIS process from TDSI foundry [37]. The Scanning Electron Microscope (SEM) image of the fabricated gyroscope is shown in Figure 5.12(a) that includes the resonator element, inter-digitated capacitive transducer and two kinds of springs supporting the gyroscope structures. The fabrication steps in the MIDIS process are well detailed in our previous publications [31, 32, 38]. MIDIS process allows precise fabrication of the inter-digitated fingers with a gap of 2µm for both symmetric and asymmetric configurations, as depicted in Figure 5.12(b). The gyroscope dimensions are 1800 µm x 850 µm with 30 µm device thickness.

The experimentation targeted both the dynamic performance of the driving system and its impact on the metrology specifications of the gyroscope. Figure 5.13 shows the schematic of the experimental setup used for both calibration and characterization of the dynamic performance of the gyroscope. The experimental calibration system consisted of a horizontal rotation table from Aerotech Inc. (ARMS-200) for application of rotary motion as depicted by Figure 5.13(a). A network analyzer (Agilent E5061B-ENA) is employed for dynamic

performance characterization as illustrated by Figure 5.13(b) [39]. Figure 5.14 shows the experimental results for the resonant frequency of the drive and sense modes under the application of different excitation voltages.

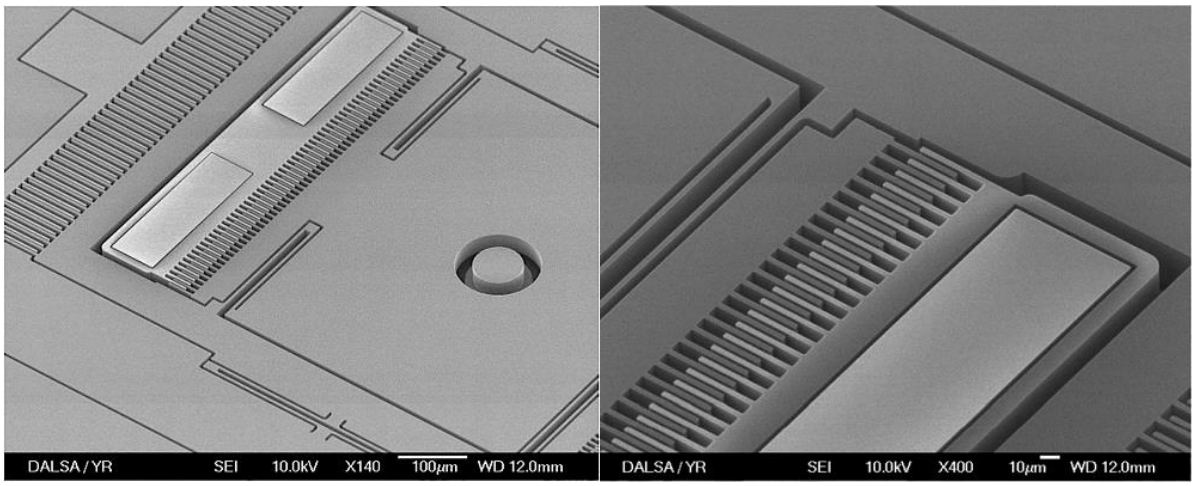

(a) (b)

Figure 5.12 (a) SEM image of the fabricated gyroscope device. (b) Inter-digitated sensing electrodes

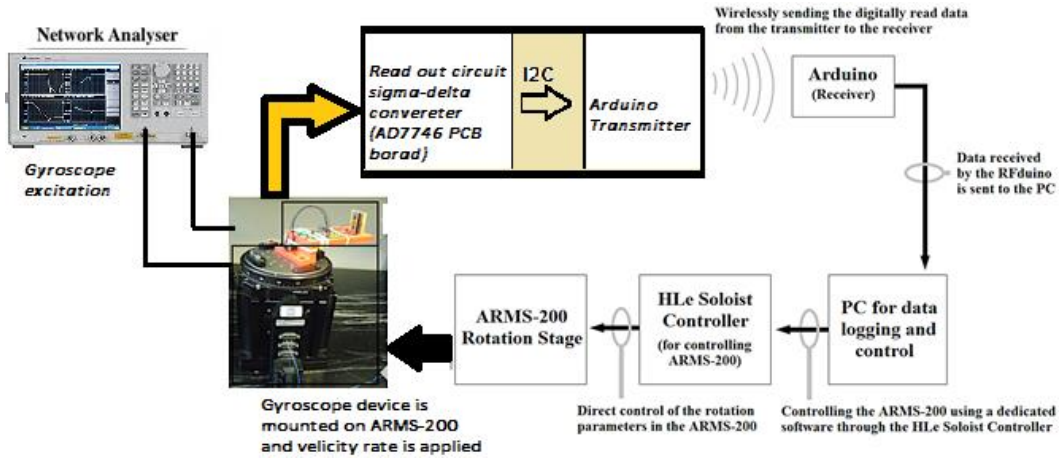

(a)

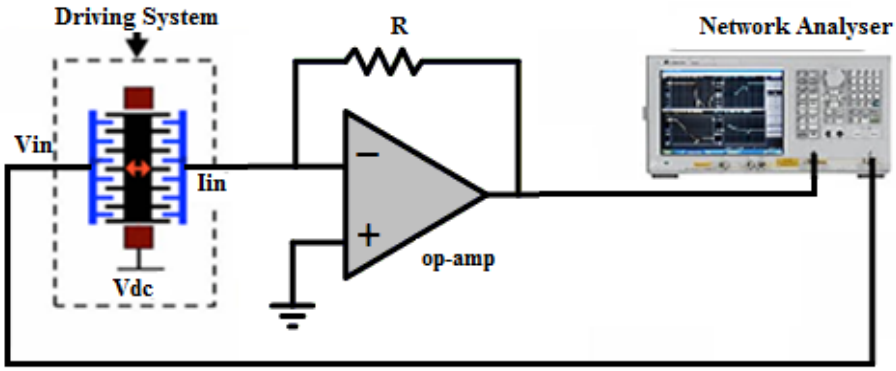

(b)

Figure 5.13 Schematic of the experimental set-up. (a) Sensor Calibration Setup. (b) Dynamic performance characterization system

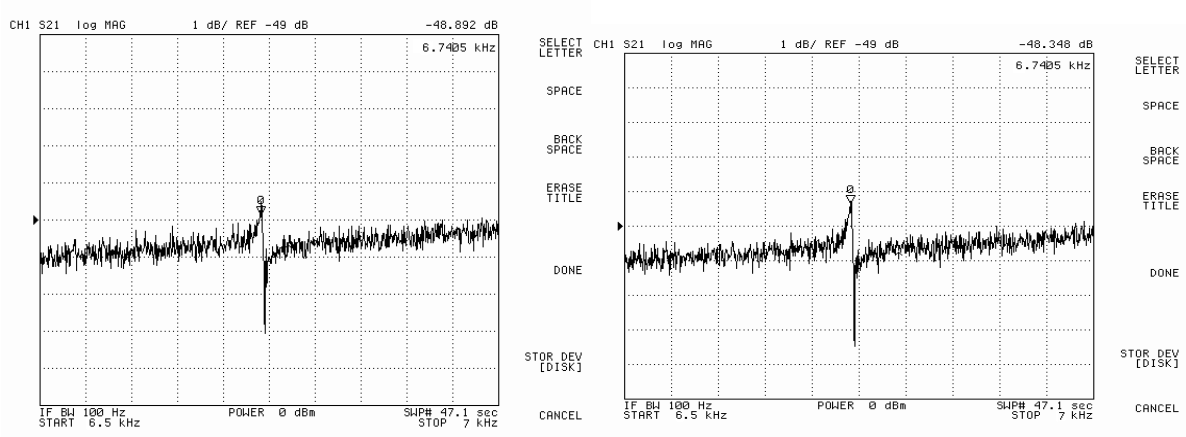

(a) (b)

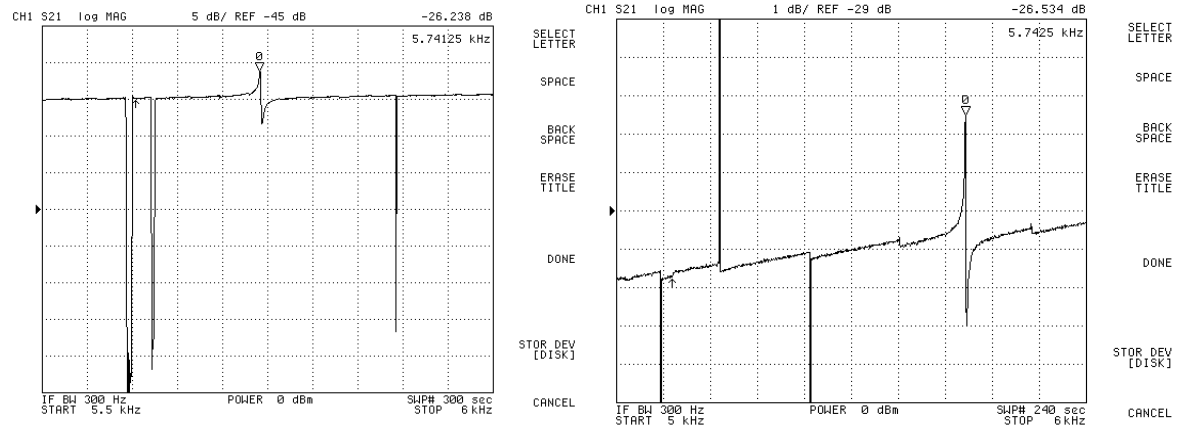

(c) (d)

Figure 5.14 Spectral response magnitude results. (a) 4VDC (Drive mode). (b) 5VDC (Drive mode). (c) 6VDC (Sense mode). (d) 6.5VDC (Sense mode)

The sensor is mounted on the horizontal rotation table that allows the application of precise angular velocity and provides slip rings for interconnections purpose with the external conditioning circuit (capacitance-to-digital converter circuit from Analog Devices Inc., model AD7746). Figure 5.15 illustrates the capacitance measurements in terms of the maximum Coriolis force generated by different angular velocities. The slope of the curve represents the sensor sensitivity and it is experimentally calculated as 0.8fF/(°/s).

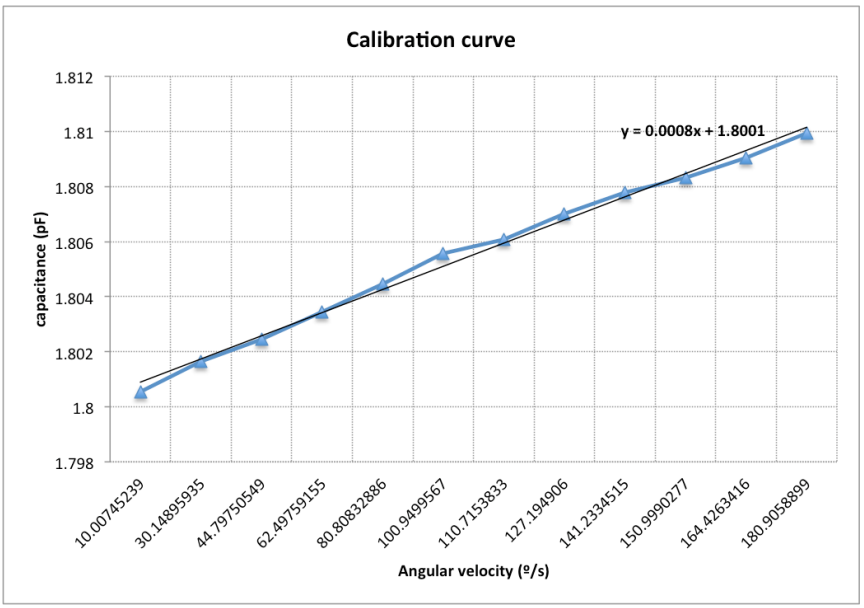

Figure 5.15 Calibration curve of the gyroscope sensor

The *Q* is characterized through the measurement of the bandwidth, *BW* at -3dB from the resonant peak, as given by Equation (5.12). To our knowledge, we demonstrate the highest reported *Q* for an unmatched mode rate gyroscope at 52,300.

$$Q_d = \frac{\omega_{nd}}{BW} \tag{5.12}$$

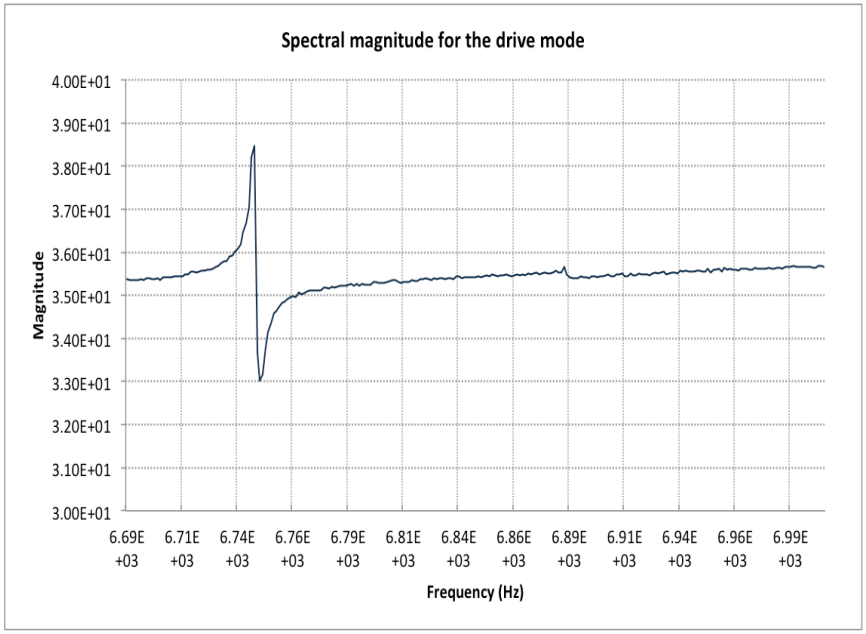

Figure 5.16 The measurement of the Q of the gyroscope

The resolution of the gyroscope is limited by the noise floor performance. In this case, the Brownian noise (Thermo-mechanical noise) for the gyroscope is given by Equation (5.13) as,

$$\frac{\Omega_n}{\sqrt{BW}} = \sqrt{\frac{k_B T \omega_{ns}}{m_s Q_s \omega_{nd}^2 x_{\max}^2}} \tag{5.13}$$

where m_s is the mass of the proof mass, BW is the gyroscope bandwidth, x_{max} is the maximum displacement made by the resonator, T is the temperature, and Q_s is the sense axis Quality factor. Figure 5.17 shows the overall gyroscope noise caused both by the mechanical and electronic sources. The use of Σ-Δ based capacitance to digital converter (CDC) (AD7746) [33] helps to reduce the effect of the electronic noise. The AD7746 uses a combination of two signal-processing techniques, the oversampling 24-bit Σ-Δ modulator and noise shaping filter that provide a high resolution of 4 aF. Based on 6σ confidence interval, the total noise floor is measured as $6x10^{-2}$ fF/√Hz over a frequency bandwidth of 100 Hz. Table-1 summarizes the important specifications of the developed gyroscope sensor.

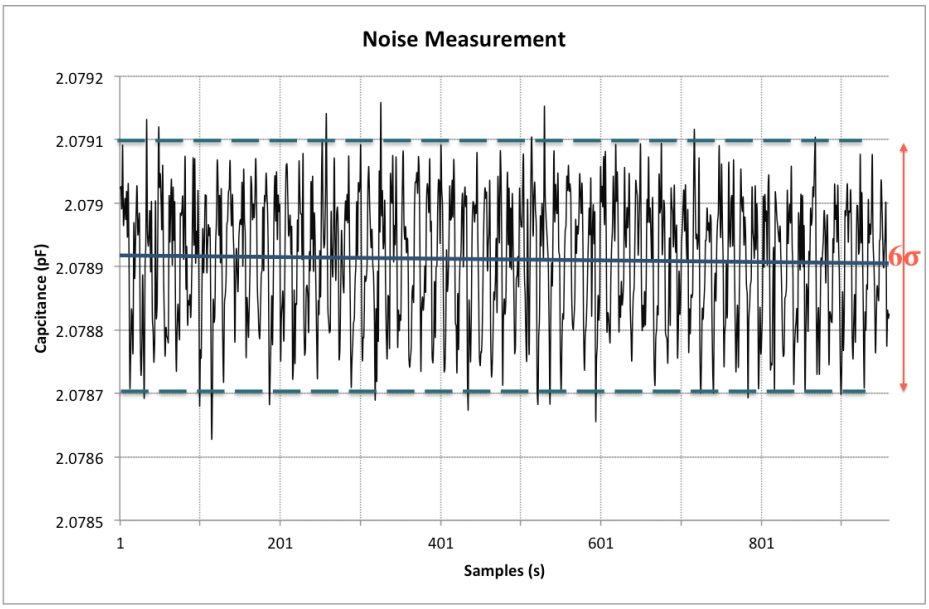

Figure 5.17 Noise measurement

Table 5-1 Experimentation Summary of gyroscope specifications

Parameters	Values
Angular Velocity range (º/s)	0-180º/s
Sensor sensitivity	0.8fF/ º/s
Noise measurement	$6x10^{-2}$ fF/√Hz
Sensor resolution	0.71º/s
Driving frequency	6.7 KHz
Q-factor (drive mode)	52300
Dimension area	1800x1000x30 (μm^3)

Table 5-2 Simulation Summary of gyroscope specifications

Parameters	Values
Angular Velocity range (º/s)	±1000º/s
Coriolis Force Sensitivity	18 (fF/µN)
Sensor sensitivity	0.6fF/ º/s
Sensor resolution	0.55º/s
Driving frequency	6.82 KHz

Q-factor (drive mode)	72633
Dimension area	1800x1000x30 (μm^3)

5.6. Conclusions

We reported, for the first time, the design, fabrication and testing of a gyroscope in a commercial ultra-clean wafer-level vacuum encapsulation process, MIDIS process from TDSI. We demonstrated the highest reported *Q* of 52,300 for an unmatched mode rate gyroscope that is wafer-level vacuum encapsulated. In unmatched mode of operation, a certain frequency difference, Δf, is maintained between the resonant modes to insure better stability in the overall system for improved practicality in overcoming imperfections in microfabrication processes. The capacitive rate gyroscope exhibited a sensitivity of 0.8fF/º/s with excellent linearity over a wide input angular velocity range of ±1000º/s and high rate resolution of 0.71°/s. The development of the described gyroscope is MIDIS process offers several advantages including high reliability, wafer-level packaging and reproducible manufacturing at very large volume, low cost, and high yield. Further, the use of low cost wafer-level vacuum packaging techniques would allow the use of high volume low cost plastic packaging at the device level which is a significant improvement over existing state-of-the-art MEMS gyroscope technology. In near future, the development of more sophisticated gyroscope designs in one of the world's most advanced wafer level vacuum encapsulation microfabrication process would open new and exciting opportunities in inertial sensor technology.

Acknowledgments

We would like to acknowledge the financial support given by Natural Sciences and Engineering Research Council of Canada (NSERC) and University of Dayton. We would like to

acknowledge the support of Canada Microelectronics Corporation for access to MIDIS process from TDSI.

References

[1] A. Lawrence, "Introduction," in *Modern Inertial Technology: Navigation, Guidance, and Control*, ed New York, NY: Springer US, 1993, pp. 1-3.

[2] V. Kempe, "Gyroscopes," in *Inertial MEMS Principles and Practice*, ed New York: Cambridge University Press 2011, p. 492.

[3] Z. S. Guo, F. C. Cheng, B. Y. Li, L. Cao, C. Lu, and K. Song, "Research development of silicon MEMS gyroscopes: a review," *Microsystem Technologies-Micro-and Nanosystems-Information Storage and Processing Systems*, vol. 21, pp. 2053-2066, Oct 2015.

[4] C.-W. Tan, S. Park, K. Mostov, and P. Varaiya, "Design of gyroscope-free navigation systems," in *Intelligent Transportation Systems, 2001*, Oakland, CA, 2001, pp. 286 - 291.

[5] C. Acar, A. R. Schofield, A. A. Trusov, L. E. Costlow, and A. M. Shkel, "Environmentally Robust MEMS Vibratory Gyroscopes for Automotive Applications," *Sensors Journal, IEEE* vol. 9, pp. 1895 - 1906, Octobor 2009.

[6] J. Mizuno, K. Nottmeyer, Y. Kanai, O. Berberig, and T. Kobayashi, "A silicon bulk micromachined crash detection sensor with simultaneous angular and linear sensitivity," *IEEE Transducers*, pp. 1302–1305, 1999.

[7] V. Sokolovic, G. Dikic, G. Markovic, R. Stancic, and N. Lukic, "INS/GPS Navigation System Based on MEMS Technologies," *Strojniski Vestnik-Journal of Mechanical Engineering*, vol. 61, pp. 448-458, Jul-Aug 2015.

[8] J. Collin, "MEMS IMU Carouseling for Ground Vehicles," *Ieee Transactions on Vehicular Technology*, vol. 64, pp. 2242-2251, Jun 2015.

[9] H. S. Zeng and Y. Zhao, "Sensing Movement: Microsensors for Body Motion Measurement," *Sensors*, vol. 11, pp. 638-660, Jan 2011.

[10] F. Ayazi, "Multi-DOF inertial MEMS: From gaming to dead reckoning," in *Solid-State Sensors, Actuators and Microsystems Conference (TRANSDUCERS), 2011 16th International*, 2011, pp. 2805-2808.

[11] R. Bogue, "Resonating gyroscopes: the next big challenge for MEMS technology," *Sensor Review*, vol. 27, pp. 197-199, 2007.

[12] H. Johari and F. Ayazi, "High-frequency capacitive disk gyroscopes in (100) and (111) silicon," *Proceedings of the Ieee Twentieth Annual International Conference on Micro Electro Mechanical Systems, Vols 1 and 2*, pp. 238-241, 2007.

[13] D. M. Rozelle, "The Hemispherical Resonator Gyro: From Wineglass to the Planets," in *19TH AAS/AIAA Space Flight Mechanics Meeting*, Savannah, Georgia, 2009, pp. 1157-1178.

[14] P. Pai, F. K. Chowdhury, C. H. Mastrangelo, and M. Tabib-Azar, "MEMS-Based Hemispherical Resonator Gyroscopes," *2012 Ieee Sensors Proceedings*, pp. 170-173, 2012.

[15] I. P. Prikhodko, S. A. Zotov, A. A. Trusov, and A. M. Shkel, "Sub-degree-per-hour silicon MEMS rate sensor with 1 million Q-factor," in *Solid-State Sensors, Actuators and Microsystems Conference (TRANSDUCERS), 2011 16th International*, 2011, pp. 2809-2812.

[16] J. Y. Cho, J. K. Woo, J. L. Yan, R. L. Peterson, and K. Najafi, "Fused-Silica Micro Birdbath Resonator Gyroscope (mu-BRG)," *Journal of Microelectromechanical Systems*, vol. 23, pp. 66-77, Feb 2014.

[17] C. H. Ahn, S. Nitzan, E. J. Ng, V. A. Hong, Y. Yang, T. Kimbrell, *et al.*, "Encapsulated high frequency (235 kHz), high-Q (100 k) disk resonator gyroscope with electrostatic parametric pump," *Applied Physics Letters*, vol. 105, Dec 15 2014.

[18] M. Sharma, E. H. Sarraf, R. Baskaran, and E. Cretu, "Parametric resonance: Amplification and damping in MEMS gyroscopes," *Sensors and Actuators a-Physical*, vol. 177, pp. 79-86, Apr 2012.

[19] S. H. Choa, "Reliability of vacuum packaged MEMS gyroscopes," *Microelectronics Reliability*, vol. 45, pp. 361-369, Feb 2005.

[20] I. P. Prikhodko, A. A. Trusov, and A. M. Shkel, "North-Finding with 0.004 Radian Precision Using a Silicon Mems Quadruple Mass Gyroscope with Q-Factor of 1

Million," *2012 Ieee 25th International Conference on Micro Electro Mechanical Systems (Mems)*, 2012.

[21] A. A. Trusov, G. Atikyan, D. M. Rozelle, A. D. Meyer, S. A. Zotov, B. R. Simon, *et al.*, "Flat Is Not Dead: Current and Future Performance of Si-MEMS Quad Mass Gyro (QMG) System," *2014 Ieee/Ion Position, Location and Navigation Symposium - Plans 2014*, pp. 252-258, 2014.

[22] I. P. Prikhodko, S. A. Zotov, A. A. Trusov, and A. M. Shkel, "What is MEMS Gyrocompassing? Comparative Analysis of Maytagging and Carouseling," *Journal of Microelectromechanical Systems*, vol. 22, pp. 1257-1266, Dec 2013.

[23] S. H. Lee, J. Mitchell, W. Welch, S. Lee, and K. Najafi, "Wafer-level vacuum/hermetic packaging technologies for MEMS," *Reliability, Packaging, Testing, and Characterization of Mems/Moems and Nanodevices Ix*, vol. 7592, 2010.

[24] B. Lee, S. Seok, and K. Chun, "A study on wafer level vacuum packaging for MEMS devices," *Journal of Micromechanics and Microengineering*, vol. 13, pp. 663-669, Sep 2003.

[25] R. Gooch, T. Schimert, W. McCardel, B. Ritchey, D. Gilmour, and W. Koziarz, "Wafer-level vacuum packaging for MEMS," *Journal of Vacuum Science & Technology a-Vacuum Surfaces and Films*, vol. 17, pp. 2295-2299, Jul-Aug 1999.

[26] Y. Jeong, D. E. Serrano, V. Keesara, W. K. Sung, and F. Ayazi, "Wafer-Level Vacuum-Packaged Tri-Axial Accelerometer with Nano Airgaps," *26th Ieee International Conference on Micro Electro Mechanical Systems (Mems 2013)*, pp. 33-36, 2013.

[27] C. S. Premachandran, S. C. Chong, S. Liw, and R. Nagarajan, "Fabrication and Testing of a Wafer-Level Vacuum Package for MEMS Device," *Ieee Transactions on Advanced Packaging*, vol. 32, pp. 486-490, May 2009.

[28] M. M. Torunbalci, S. E. Alper, and T. Akin, "Wafer Level Hermetic Encapsulation of MEMS Inertial Sensors using SOI Cap Wafers with Vertical Feedthroughs," *2014 1st Ieee International Symposium on Inertial Sensors and Systems (Isiss 2014)*, pp. 153-154, 2014.

[29] K. Zhang, W. Jiang, and X. X. Li, "Wafer-level sandwiched packaging for high-yield fabrication of high-performance MEMS inertial sensors," *Mems 2008: 21st Ieee International Conference on Micro Electro Mechanical Systems, Technical Digest*, pp. 814-817, 2008.

[30] R. N. Candler, M. A. Hopcroft, B. Kim, W. T. Park, R. Melamud, M. Agarwal, *et al.*, "Long-term and accelerated life testing of a novel single-wafer vacuum encapsulation for MEMS resonators," *Journal of Microelectromechanical Systems*, vol. 15, pp. 1446-1456, Dec 2006.

[31] G. Xereas and V. P. Chodavarapu, "Wafer-Level Vacuum-Encapsulated Lame Mode Resonator With f-Q Product of 2.23 x 10(13) Hz," *Ieee Electron Device Letters*, vol. 36, pp. 1079-1081, Oct 2015.

[32] A. Merdassi, P. Yang, and V. P. Chodavarapu, "A Wafer Level Vacuum Encapsulated Capacitive Accelerometer Fabricated in an Unmodified Commercial MEMS Process," *Sensors*, vol. 15, pp. 7349-7359, Apr 2015.

[33] Analog-Devices-Inc. Available: http://www.analog.com/en/products/analog-to-digital-converters/integrated-special-purpose-converters/capacitive-to-digital-and-touch-screen-controllers/ad7746.html

[34] J.-P. Guan and X.-M. Liu, "Improved Design and Modeling of Micromachined Tuning Fork Gyroscope Characterized by High Quality Factor," *Journal of Electronic Science and Technology* vol. 8, pp. 280-286, September 2010.

[35] C. Acar and A. Shkel, *MEMS Vibratory Gyroscopes, Structural Approaches to Improve Robustness*: Springer Science+Business Media, 2009.

[36] H. Mansoor, H. Zeng, K. Chen, Y. Yu, J. Zhao, and M. Chiao, "Vertical optical sectioning using a magnetically driven confocal microscanner aimed for in vivo clinical imaging," *Optics Express*, vol. 19, pp. 25161-25172, 2011.

[37] TDSI-Semiconductor. *MEMS Integrated Design for Inertial Sensors (MIDIS)*. Available: http://www.teledynedalsa.com/semi/mems/applications/midis/

[38] A. Merdassi, M. N. Kezzo, G. Xereas, and V. P. Chodavarapu, "Wafer level vacuum encapsulated tri-axial accelerometer with low cross-axis sensitivity in a commercial MEMS Process," *Sensors and Actuators A: Physical*, vol. 236, pp. 25-37, 12/1/ 2015.

[39] C. Comi, A. Corigliano, G. Langfelder, A. Longoni, A. Tocchio, and B. Simoni, "- A Resonant Microaccelerometer With High Sensitivity Operating in an Oscillating Circuit," vol. - 19, pp. - 1152, 2010.

CHAPTER -6

6. CONCLUSIONS AND LIMITATIONS

6.1. Conclusions

TDSI Inc. (Teledyne DALSA Inc.) promoted the market of MEMS inertial sensors through the development of MEMS Integrated Design for Inertial Sensors (MIDIS). The fabrication platform has been proven to be cost effective, reliable as well as adaptable to provide stable volume production and considered suitable for the development of high performance capacitive inertial sensors. The standard MIDIS process offered some attractive extraordinary features for the profit of inertial sensors designs. Amongst, ultra-clean wafer level encapsulation under high vacuum pressure on the order of 10 mTorr that can be achieved and very low leak rate of 45 molecules/s (7.5 10−13 atm·cc/s). Furthermore, TSVs are added as key features to enable 3-D integration of MEMS devices with ASIC circuits.

The research contributions in this dissertation target mainly the development of high performance capacitive inertial sensor platform including uniaxial accelerometer, tri axial accelerometer and rate grate gyroscope sensor. These MEMS devices has met the requirement needs in terms of high performance, size and cost effectiveness. The main key features that could characterize the novel designs of the presented inertial sensors can be summarized as follows:

- Simultaneous measurement of the three main components of acceleration with the objective to attain ultra-low cross axis sensitivity using a single chip area.

- Ability of acceleration detection along the Out-of-plane direction.
- Very low noise performance and consequently higher accuracy in the measurement can be achieved
- High quality factor yielding to a high sensitivity under unmatched mode operation of the gyroscope sensor.

The experimental validations of the MEMS inertial sensors are performed over several fabricated prototypes proving the fidelity of the experimental results and hence the consistency of the current designs. The uniaxial sensor allows the detection of the acceleration on the order of 33mg over wide measurement range that could attain $\pm 100g$. Further, the three axis accelerometer comprising single chip area allows the measurement of three acceleration components over $\pm 50g$ with very low cross-talk between axes, measuring only 0.8%. The resolution attained in these sensors is fixed to 1.8 mg which is considered suitable enough for various consumer and industrial applications. The gyroscope sensor proved the concept that high quality factor that achieved, more than 50,000, under unmatched mode where the dynamic stability is insured. The presented gyroscope is suited for wide range measurement of angular velocity reaching 1000°/s for a given resolution that can attain a minimum value of 0.71°/s.

The different sensors devices developed in this dissertation are considered the basis concept toward the development of multi-axis Inertial Module Unit (IMU) which can be fabricated on the same wafer using a unified process.

6.2. Future Works

The current approach presented in this dissertation is extended to serve the basis for the fabrication of non-inertial MEMS devices as well. Indeed, a new capacitive absolute pressure sensor is developed benefiting from the specific feature of high vacuum packaging to enable absolute pressure measurement. The new method is based on semi commercial approach where some post processing steps are added to MIDIS process in order to achieve the fabrication of the novel pressure sensor. Consequently, this approach offers a promising option to manufacture multi-axis accelerometers, gyroscopes, and a pressure sensor on a single die. Figure 6.1 shows an example of microscope image of a fabricated absolute pressure sensor.

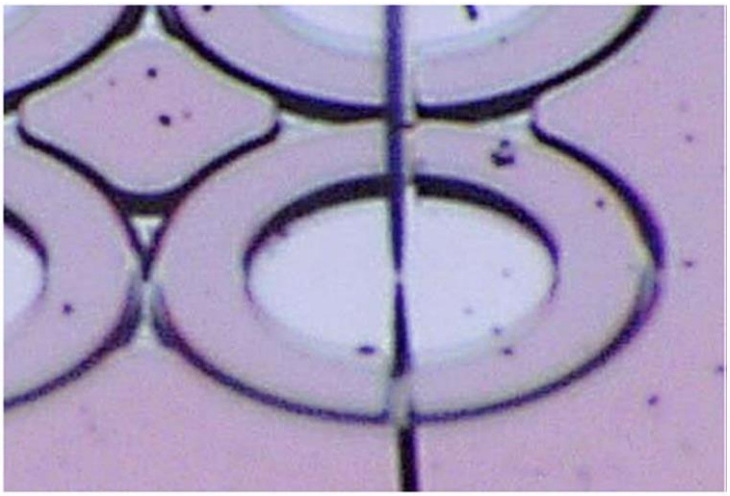

Figure 6.1 Microscope image of an absolute pressure sensor

Likewise, other MEMS devices such as microphone, micro pump, and resonant sensors can be implemented on MIDIS process with the same approach of customizing the fabrication in order to achieve the specific structures of the fabricated MEMS device. The reliability, robustness and the performance of the 3-D integration with IC circuits are considered important key features that should be studied in depth and experimentally tested in order to fully qualify the performance of the fabricated microsystems and ultimately the purview scope of MIDIS process.